3. Material Properties: Measurement and Data

The density of a fluid is defined as the mass of the fluid per unit volume. Some methods of measuring the density of the fluid with high precision determine the variation of one quantity in this ratio when the other is fixed and a further state variable is altered. Other methods make use of the effect of the fluid density on the position or motion of a rigid body contained within it. Examples of these instruments are described in this chapter for operation over a wide range of thermodynamic states.

3.1 Density

The density ρ is defined as the mass of unit volume of a substance under prescribed conditions. The density varies with pressure and temperature, the variation with respect to both variables being much greater in gases than liquids.

The specific gravity (SG), also termed the relative density, is determined by dividing the density of the substance by the density of a standard substance obtained under the same conditions of temperature and pressure. In particular, the usual definitions

are

$$\text{Liquid SG} = \frac{\text{density of liquid}}{\text{density of water}} \tag{3.1}$$

$$\text{Gas SG} = \frac{\text{density of gas}}{\text{density of air}} \tag{3.2}$$

Commonly accepted sets of reference conditions are

- normal temperature and pressure (NTP), usually taken as the temperature at 0.00 °C and a pressure of 760 mmHg, and
- standard temperature and pressure (STP), usually taken as the temperature at 15.00 °C and a pressure of 0.101325 MPa.

Despite the apparent simplicity of its definition, the accurate measurement of the density of fluids is complex and many novel techniques have been developed. Special care is required in measurements at high pressures in either phase while the hazards associated with operation in the gas phase, when the stored energy in a system is large, add to the complexity of experimental work considerably. In this chapter, modern techniques for the measurement of density will be presented, and emphasis will be given to those techniques that cover very wide temperature and pressure ranges, with low uncertainty.

3.1.1 Piezometers

Densimeters that employ magnetic-suspension or vibrating-element techniques, which will be discussed later in this chapter, now provide more-convenient methods for achieving a low level of uncertainty in the measurement of density. However, piezometers have been used extensively in the past because of their simplicity and high accuracy when used with care. Piezometers can be divided into three categories:

1. devices that measure the amount of mass or amount of substance within a fixed volume,
2. devices that determine the change in pressure effected by a change in volume, and
3. devices that utilize one or more expansions from one volume to another.

Fixed-Volume Piezometers

In fixed-volume devices, the mass or amount of substance in a known volume is measured at a temperature and pressure that are determined independently. To determine the mass of the sample the container is often weighed directly with and without the sample present. Alternatively, if the fluid is a gas, it may be allowed to expand into a much larger volume so that the final conditions are near ambient, when a relatively simple equation of state can be used to evaluate the amount of substance present.

The instrument shown in Fig. 3.1, made out of Pyrex glass, was employed for measurements of the saturated density of liquid refrigerants up to 10 MPa pressure with an estimated uncertainty of 0.3% [3.1]. It consists of a vessel connected to a capillary. The capillary is used to define the exact volume of the liquid, thus giving high resolution when filling the piezometer. Following evacuation of the piezometer, it is weighed. The sample is then introduced, degassed, and the device disconnected from the filling line. The mass of the sample was obtained by weighing again, while its volume by observing the liquid level in the tube.

Hwang and coworkers [3.2] developed a continuously weighed piezometer, based on an earlier apparatus developed by *Machado* and *Street* [3.3]. Hwang's piezometer consists of a weight measurement system, an isothermal bath with a temperature control and measurement system, a sample pressurizing system, and a high vacuum system. The sample is introduced into the piezometer vessel of known volume via a flexible capillary feed line. The mass of the piezometer plus fluid is then determined with an electronic force balance from which it is suspended at all times. In general, fixed volume devices are capable of density measurements with an uncertainty of ±0.1% or better, depending upon the fluid properties.

Fixed-volume cells have been used to great effect over a wide range of conditions. *Kubota* et al. [3.4] employed a fixed-volume cell charged with a known

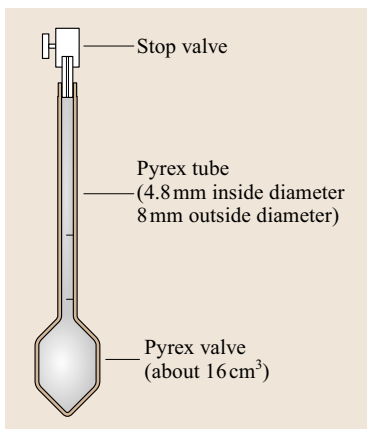

Fig. 3.1 Fixed-volume piezometer (after [3.1])

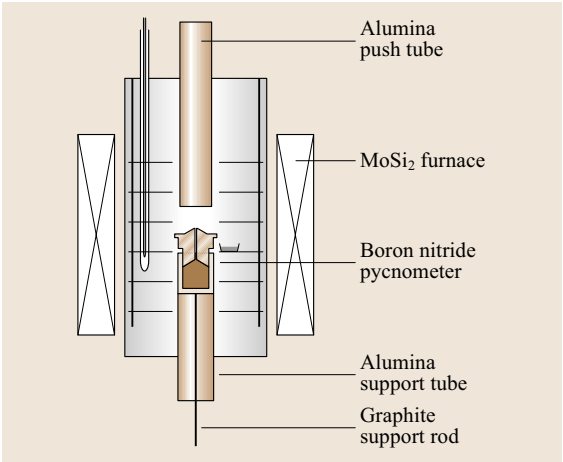

Fig. 3.2 High-temperature pycnometer, developed by *Sato* et al. [3.5]

mass of sample for the measurement of the density of refrigerants up to 100 MPa pressure. *Sato* et al. [3.5] operated a high-temperature pycnometer (Fig. 3.2) made of boron nitride, for the measurement of the density of molten silicon. In this case, the pycnometer containing a cylindrical sample of solid silicon was supported by a graphite rod and installed at the appropriate position on an alumina support tube (Fig. 3.2) inside the furnace. Then the upper part (cap) of the pycnometer had been partially inserted into the lower part during assembly. After the silicon melted, the apparatus was temporarily evacuated and the alumina push tube was lowered slowly to push the upper part of the pycnometer into position in the lower part. This caused the excess of molten silicon now in the pycnometer to overflow, leaving it exactly full and containing a defined volume. The mass of the sample is determined by subsequent weighing outside of the furnace. *Sato* et al. [3.5] reported density measurements up to 1850 K with an estimated uncertainty of better than 0.5%. However, at such high temperatures the difficulties of measurement generally mean that the discrepancies between investigators exceed their mutual quoted uncertainties so that it is not yet possible to confirm the estimate of error in this case.

Variable-Volume Piezometers

Variable-volume devices are characterized by sample cells that change in volume during the experiment. The change in volume is usually achieved using bellows (see next section) or pistons. Some older devices employed mercury as a liquid piston (e.g., *Goodwin* et al. [3.6]) but environmental and safety considerations now discourage the use of mercury in large quantities. New designs for piston devices have recently been employed [3.7]. However, the variable volume devices are generally less accurate than other methods, with uncertainties of about ±1%, and thus are not described further here.

Expansion Piezometers

The basic principle of expansion devices is that the sample is expanded from one volume into a second volume (usually evacuated), and the ratio of the original volume to the final volume establishes the ratio of densities before ρ_0 and after expansion ρ_f with

$$\frac{\rho_0}{\rho_f} = \frac{V_a + V_b}{V_a} = r \,, \tag{3.3}$$

where, V_a is the volume occupied by the fluid before the expansion, $(V_a + V_b)$ is the volume after the expansion and r is the cell constant. The device may utilize either a single expansion (large r) or a series of expansions.

Single expansion devices employ volume ratios r ranging from 50 to 1000 so that a pressure near atmospheric results from the expansion. The final molar density can then be calculated from the temperature and pressure using a simple virial equation of state. Once the final density is known, the original density ρ_0 can be calculated from (3.3), or the amount of substance by multiplying the final density by the total volume of the system. Single expansion devices have been recently described by *Duarte* et al. [3.8].

The most common multiple expansion method is that developed by *Burnett* [3.9], recently successfully applied by *Stouffer* [3.10]. These techniques have the advantage that neither mass nor volume need to be measured directly. Only pressure and temperature are measured before and after the expansion from a single volume into the combination of the original volume and an additional one. Although the technique is usually not an absolute technique, the uncertainty in the measurement of the density is often better then ±0.05%.

3.1.2 Bellows-Type Densimeters

Bellows-type densimeters are cells that contain and enclose the sample fluid. The entire cell, or at least a part of it, is a flexible bellows, which transmits the pressure on the outside of the cell to the test fluid. The pressure can be exerted and measured on the outside of the flexible cell through another pressure transmitting fluid which itself can be pressurized by a piston pump. The linear movement of the end of a bellows of constant cross section is measured to determine the compression

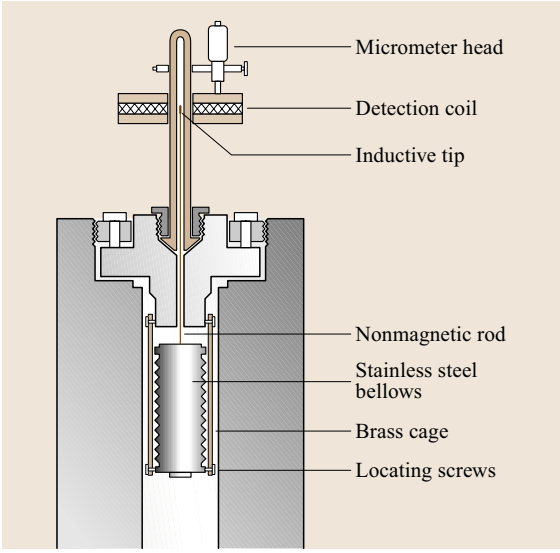

Fig. 3.3 High-pressure bellows-type pycnometer, developed by *Dymond* et al. [3.11, 12]

of the fluid in the measuring cell caused by the applied pressure.

The instrument shown in Fig. 3.3, is a bellows-type densimeter, employed by *Dymond* et al. [3.11, 12], for the measurement of the density of hydrocarbons up to 600 MPa with an estimated uncertainty of 0.1%. A known amount of liquid sample is introduced into the sealed metal bellows. In this case the movement of the bellows' end is determined using the magnetic induction between an inductive tip mounted on a rod that is itself attached to the end of the bellows and an external detector coil. Measurement of the movement of the detector coil along the tube to secure a constant induction serves to determine the position of the end of the bellows. Bellows densimeters have been employed by various investigators. *Iso* and *Uematsu* [3.13] employed such a densimeter for the measurement of the density of refrigerants up to 10 MPa pressure.

3.1.3 Vibrating-Element Densimeters

If a solid, elastic body containing (or surrounded by) a fluid is driven to oscillate, then the frequency of resonance of the solid/fluid assembly will depend upon the properties of the fluid and, in particular its density ρ. The resonant frequency will also depend upon the properties of the solids involved and, in particular, upon a modulus K of the solid oscillator of mass M, whose elastic distortion yields the oscillatory behavior. As a result, for any form of solid/fluid oscillator of this kind we can write an expression for the resonant frequency f as [3.14]

$$f = \sqrt{\frac{K}{(M + k\rho)}}\,, \tag{3.4}$$

where k is characteristic of the particular arrangement of the oscillator. Evidently, if it is possible to calculate, or measure, K and k independently then measurement of the resonant frequency of the oscillation can yield the density of the test fluid.

A common feature of all types of vibrating element densimeters is the need to excite the vibration of the solid element and to observe its resonant frequency. There are two mechanisms usually employed for this purpose [3.14].

Magnetic drive of the vibrating element can be achieved by means of small coil assemblies mounted within or upon the vibrating element and forced into motion by application of electric currents in fixed driving coils. Detection of motion can be accomplished in the same way by the same or a different set of coils. If a steady drive is desired, the signals picked up by the sensors are amplified and fed back as a drive to maintain the disturbing forces on the vibrating body of the meter. This mechanism can actually be made to self-tune to the resonant frequency of the oscillator automatically if the resonance is sufficiently sharp. The main advantage of the magnetic drive and pickup systems is that they are noncontact methods; they use conventional copper windings and they are usable within the temperature range of −200 to +200 °C.

Alternatively, there is a wide range of piezoelectric materials that allow the direct application of an electric current to a solid so as to causes an elastic distortion. These materials demonstrate good temperature characteristics and have the advantage of being low in cost. They have a relatively high impedance, making the signal conditioning circuitry easy, unlike the circuitry for electromagnetic sensors. Piezoelectric drives are mechanically affixed to the vibrating body by adhesives. Therefore, attention must be paid to the careful placement of the mount in order to reduce the strain experienced by the piezo element owing to the thermal and pressure stresses to which the element is subjected during operation over ranges of temperature and pressure. A number of different types of densimeters have been developed that utilize vibrating elements and the most common ones are [3.14]:

1. Vibrating-tube densimeters are suitable for operation with a wide range of fluids from gases to liquids

as well as to slurries. Commercial instruments using this principle are widely available and are frequently used in research laboratories and industrial monitoring. The mode of operation is based on the transverse vibration of a single circular section tube constrained to vibrate in a single plane.

2. Vibrating-cylinder densimeters are ideal for liquified gas products or refined liquids.
3. Tuning-fork densimeters make use of the natural frequency of low-mass tuning forks. In some cases, the fluid is taken into a small chamber in which the electromechanically driven forks are situated, or in other cases the fork is inserted directly into the liquid.

In the vibrating-tube densimeter the basic measurement to be made is of the resonant frequency of the tubular oscillator filled with the fluid whose density is to be measured. The mass of fluid inside the oscillator determines the change of the resonant frequency of oscillation from that obtained when the tube is filled with another fluid or even in vacuo. Thus, by measuring this change of frequency it is possible to obtain the mass that fills the tube volume and therefore the density of the sample. In practice, the configuration of the tubular oscillator is generally chosen in the form of a 'V' or a 'U' so as to define precisely a single mode of oscillation. For that reason it is not usual to seek to perform absolute measurements with the densimeter using a fundamental theory. Instead one begins with the equation that derives from the simple phenomenological theory that arises from (3.4) so that

$$\rho = A\tau^2 - B \,, \tag{3.5}$$

where τ is the measured period of vibration for the tube when filled with a fluid of density ρ, and A and B calibration parameters of the densimeter, which may be functions of pressure and temperature. The values of A and B have to be obtained by the use of two fluids of known density, ρ_1 and ρ_2, as calibrants under the same conditions of temperature and pressure. Equation (3.5) can then be rewritten to eliminate A and B, in the form

$$\rho = \frac{(\rho_1 - \rho_2)\left(\tau^2 - \tau_2^2\right)}{\left(\tau_1^2 - \tau_2^2\right)} + \rho_2 \,, \tag{3.6}$$

where τ_1 and τ_2 are the periods of vibration of the tube when filled with calibrants 1 and 2, respectively, at the same temperature and pressure as the sample liquid. For the best vibrating tube densimeters the dependence on temperature and pressure of the two instrument constants is rather small and, if modest accuracy is sought, it is possible to treat them as constants. However, for the highest accuracy it is always best to use the full form of (3.6) at each thermodynamic state.

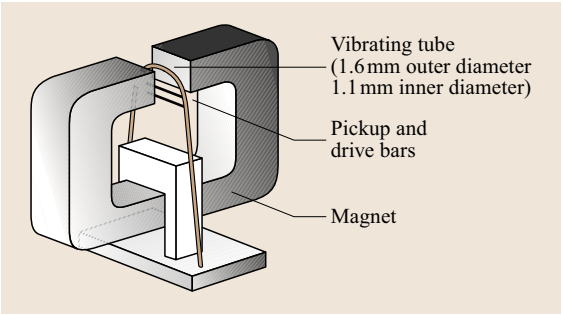

Fig. 3.4 Vibrating-tube densimeter, developed by *Hynek* et al. [3.15]

Vibrating-tube densimeters have been employed by a large number of investigators. A very small sample of the applications is listed here. *Hynek* et al. [3.15] constructed a vibrating-tube densimeter (Fig. 3.4) for measurements with corrosive solutions at temperatures up to 723 K and pressures up to 40 MPa, with an uncertainty of about 0.5%. A similar vibrating U-tube was developed by *Blencoe* et al. [3.17] for measurements of the density up to 200 MPa. Similar devices have been employed for the measurement of the density of refrigerants, for example, *Defibaugh* and *Morrison* [3.18] employed such an instrument for the measurement of the density of refrigerant R22 from 253 to 373 K and up to 6.2 MPa with an estimated uncertainty of 0.05%. *Sousa* et al. [3.19] measured the density of refrigerant R142b from 293 to 403 K and pressures up to 17 MPa.

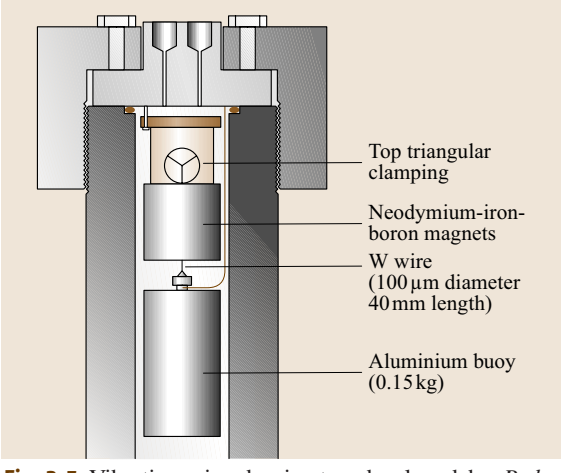

Fig. 3.5 Vibrating-wire densimeter, developed by *Padua* et al. [3.16]

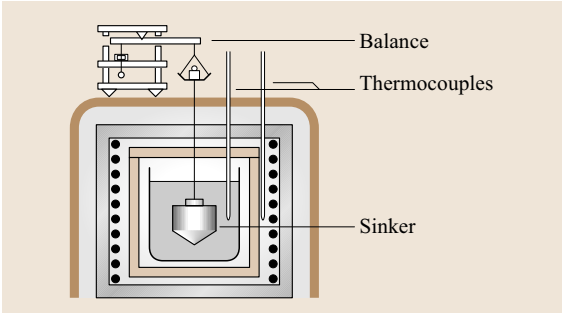

Fig. 3.6 Buoyancy-type densimeter

Their estimated uncertainty was 1% for the liquid phase and 3% for the vapor phase.

A special category of vibrating-element densimeters is the vibrating-wire densimeter. Such an instrument is shown in Fig. 3.5. In this case, the vibrating element comprises a thin metallic wire of radius R and length $2L$ with the top end fixed and a solid cylindrical weight of volume V_w suspended from the lower end. The wire is placed in a uniform permanent magnetic field generated by two rare-earth magnets. The motion of the wire is driven by the application of an oscillatory current in the wire. Variation of the frequency of the driving current with the aid of an impedance analyzer, or in some other way, can be used to find the resonant frequency. The presence of the sample fluid around the vibrating wire contributes to the change in the resonant frequency

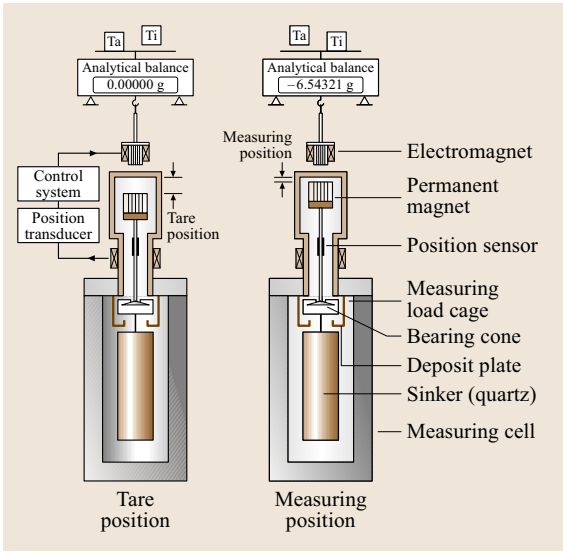

Fig. 3.7 Principle of the new single-sinker densimeter, developed by *Klimeck* et al. [3.20]

from that observed when the wire vibrates in vacuo. The largest single effect of the fluid is a result of the buoyancy force acting on the suspended weight. However, there is a minor effect caused by the fluid flow around the vibrating wire. According to the theory of such a device, treated in detail elsewhere [3.21, 22], the resonant frequency of the wire can be expressed in terms of the density of the fluid as well as its viscosity, together with the radius of the wire, the density of its material, the volume of the suspended weight and the density of the material from which the weight is constructed. Many of these quantities are amenable to direct, independent measurement but some are not. In particular, the measurements of the wire radius and of its density are usually not accomplished with sufficient accuracy by independent means. For that reason these two quantities are usually determined by calibration using two fluids of known density and viscosity. This needs to be done only at one thermodynamic state since changes with temperature and pressure are readily evaluated for other conditions.

The first attempts to build densimeters based on the vibrating-wire sensor and designed according to the theory of the vibrating wire took place in the group of *Wakeham* at Imperial College, London, around 1990 [3.23], where the most recent version of the hydrodynamic model has also been formulated. A second version of the vibrating-wire densimeter was built at the Instituto Superior Tecnico, Lisbon, initially as a pure densimeter [3.16]. This design is shown in Fig. 3.5. A 100 µm-diameter tungsten wire was employed, while a top triangular clamping ensured the predominance of the first vibrational mode of motion. The uncertainty in the density measurements achieved with this instrument is ±0.05% at the 95% confi-

Table 3.1 Reference values for the density (kg m^{-3}) of water and steam

	Pressure (MPa)			
T (°C)	0.1	1	5	10
0.1	999.8	1000	1002	1005
10	999.7	1000	1002	1004
25	997.0	997.5	999.2	1001
50	988.0	988.4	977.0	992.3
75	974.8	975.1	977.0	979.2
100	0.5897	958.8	960.6	962.9
200	0.4603	4.854	867.3	870.9
300	0.3790	3.876	22.05	715.3
500	0.2805	2.824	14.58	30.48
700	0.2227	2.233	11.30	22.94

Table 3.2 Density ρ (kg m^{-3}) of some *n*-alkanes in the liquid phase

		P (MPa)	273.15 K	298.15 K	323.15 K	348.15 K	373.15 K
n-Pentane	C_5H_{12}	0.101	645.7	621.2	595.5	568.0	537.7
		5	650.8	627.5	603.4	577.8	549.4
		10	655.6	633.4	610.5	586.3	559.3
		25	668.4	648.5	628.3	606.9	582.2
		50	685.8	668.2	650.5	631.5	608.6
n-Hexane	C_6H_{14}	0.101	677.2	654.9	631.7	607.3	581.4
		5	681.6	660.2	638.2	615.3	591.0
		10	685.8	665.2	644.2	622.5	599.6
		25	697.2	678.5	659.6	640.4	620.1
		50	713.1	696.4	679.8	662.9	645.0
n-Heptane	C_7H_{16}	0.101	700.5	679.5	657.9	635.6	612.1
		5	704.5	684.2	663.5	642.3	620.3
		10	708.3	688.7	668.8	648.6	627.7
		25	718.8	700.8	682.7	664.6	646.2
		50	733.7	717.4	701.4	685.4	669.3
n-Octane	C_8H_{18}	0.101	718.7	698.7	678.2	657.2	635.3
		5	722.4	703.0	683.3	663.2	642.6
		10	726.0	707.2	688.2	668.9	649.3
		25	736.0	718.5	701.1	683.8	666.3
		50	750.2	734.3	718.7	703.4	688.2
n-Nonane	C_9H_{20}	0.101	733.1	713.9	694.2	674.1	653.4
		5	736.6	717.9	699.0	679.7	660.1
		10	740.1	721.9	703.5	685.0	666.3
		25	749.6	732.6	715.7	698.9	682.1
		50	763.3	747.8	732.5	717.6	702.9
n-Decane	$C_{10}H_{22}$	0.101	745.1	726.2	707.2	687.8	668.0
		5	748.5	730.1	711.7	693.1	674.2
		10	751.8	733.9	716.0	698.0	680.0
		25	760.9	744.2	727.6	711.2	695.0
		50	774.3	758.9	743.8	729.2	714.9
n-Undecane	$C_{11}H_{24}$	0.101	754.8	736.5	718.0	699.2	680.0
		5	758.1	740.2	722.3	704.2	685.8
		10	761.3	743.9	726.4	708.9	691.2
		25	770.2	753.8	737.6	721.5	705.5
		50	783.2	768.1	753.3	738.9	724.8
n-Dodecane	$C_{12}H_{26}$	0.101	763.4	745.3	727.0	708.5	689.6
		5	766.6	748.9	731.1	713.2	695.1
		10	769.7	752.4	735.1	717.7	700.3
		25	778.4	762.1	745.9	729.8	714.0
		50	791.2	776.0	761.2	746.7	732.6

dence level. The design was later adapted to measure the viscosity simultaneously along with a more refined theory [3.24]. The latest vibrating-wire instrument of this type was built at the University Blaise-Pascal. *Clermont-Ferrand*, France, incorporating a number of improvements [3.25].

Table 3.3 Density ρ (kg m^{-3}) of some alkenes in the liquid phase

		P (MPa)	273.15 K	298.15 K	323.15 K	348.15 K	373.15 K
Benzene	C_6H_6	0.101	899.8	873.6	846.8	819.2	790.8
		5	903.4	877.7	851.6	824.9	797.6
		10	906.9	881.8	856.3	830.4	804.0
		25	916.7	892.9	869.1	845.1	820.8
		50	931.1	909.1	887.2	865.3	843.3
Toluene	C_7H_8	0.101	885.8	862.3	838.7	814.8	790.5
		5	889.1	866.2	843.2	820.1	796.8
		10	892.4	870.0	847.6	825.2	802.8
		25	901.6	880.4	859.5	839.0	818.8
		50	915.3	895.7	876.6	858.1	840.3
Ethylbenzene	C_8H_{10}	0.101	883.4	862.6	840.8	817.9	793.9
		5	886.7	866.3	845.1	823.1	800.0
		10	889.8	869.9	849.3	828.0	805.9
		25	898.8	880.1	860.9	841.3	821.3
		50	912.1	894.9	877.5	860.0	842.3
o-Xylene	C_8H_{10}	0.101	898.0	876.5	854.9	833.2	811.5
		5	900.9	879.8	858.7	837.7	816.6
		10	903.9	883.1	862.5	842.0	821.6
		25	912.2	892.4	872.9	853.8	835.0
		50	924.6	906.1	888.1	870.6	853.7
m-Xylene	C_8H_{10}	0.101	879.6	860.0	839.4	817.6	794.5
		5	882.8	863.7	843.7	822.7	800.6
		10	886.0	867.4	848.0	827.7	806.5
		25	894.9	877.5	859.5	841.0	821.9
		50	908.1	892.3	876.1	859.7	843.0
p-Xylene	C_8H_{10}	0.101	875.6	855.8	834.9	812.9	789.5
		5	878.9	859.5	839.2	818.0	795.6
		10	882.0	863.1	843.4	822.9	801.5
		25	890.9	873.2	855.0	836.2	816.9
		50	904.1	888.0	871.5	854.8	837.8
Mesitylene	C_9H_{12}	0.101	880.7	860.7	840.2	819.2	797.6
		5	883.8	864.1	844.2	823.9	803.2
		10	886.8	867.6	848.1	828.4	808.5
		25	895.3	877.1	859.0	840.8	822.8
		50	907.9	891.2	874.6	858.3	842.4

3.1.4 Buoyancy-Type Densimeters

The buoyancy method basically makes use of Archimedes' principle. A suspended sinker (Fig. 3.6) with a known mass and volume is attached to a fine wire, and is totally immersed in the sample liquid. A precision force balance is used to measure the force to support the sinker. Once the mass, volume, and supporting weight of the sinker are known, the density of the liquid can be calculated. The principle is rather straightforward for liquids at atmospheric pressure where containment of the liquid sample is simple and attachment of a thread to a force balance causes no breach of a sealed container. However, even in these simple circumstances, some corrections need to be made for the force exerted by surface tension on the suspension wire and for the volumetric thermal expansion coefficient of the sinker. When used with great care buoyancy-type densimeters can yield results of great accuracy.

An advanced version of the buoyancy technique is the magnetic suspension system. *Klimeck* et al. [3.20] developed an advanced single-sinker densimeter em-

Table 3.4 Density ρ (kg m^{-3}) of some *n*-alcohols in the liquid phase

		P (MPa)	273.15 K	298.15 K	323.15 K	348.15 K	373.15 K
Methanol	CH_4O	0.101	810.0	786.5	762.5	737.6	710.8
		5	814.0	791.3	768.2	743.9	717.3
		10	818.0	796.0	773.6	749.8	723.5
		25	828.9	808.7	787.9	765.4	739.5
		50	844.6	826.4	807.5	786.4	760.8
Ethanol	C_2H_6O	0.101	806.3	785.0	763.1	739.6	713.8
		5	809.9	789.2	767.8	744.8	719.1
		10	813.4	793.2	772.3	749.7	724.2
		25	823.1	804.3	784.6	762.9	737.7
		50	837.2	820.0	801.9	781.2	756.1
1-Propanol	C_3H_8O	0.101	819.1	799.5	779.0	756.8	732.4
		5	822.5	803.4	783.5	761.8	737.7
		10	825.8	807.2	787.8	766.6	742.8
		25	835.0	817.7	799.6	779.6	756.4
		50	848.5	832.9	816.3	797.6	775.1
1-Butanol	$C_4H_{10}O$	0.101	824.6	805.8	786.2	765.2	742.3
		5	827.7	809.4	790.3	769.9	747.5
		10	830.8	812.9	794.4	774.5	752.5
		25	839.4	822.8	805.5	786.8	765.8
		50	852.2	837.1	821.4	804.1	784.1
1-Pentanol	$C_5H_{12}O$	0.101	828.9	811.0	792.1	772.1	750.4
		5	831.9	814.3	796.0	776.5	755.4
		10	834.8	817.7	799.8	780.9	760.2
		25	842.9	826.9	810.4	792.6	773.1
		50	855.1	840.5	825.5	809.2	790.9
1-Hexanol	$C_6H_{14}O$	0.101	833.0	815.3	797.1	778.2	758.2
		5	835.8	818.5	800.8	782.4	763.0
		10	838.6	821.7	804.5	786.6	767.6
		25	846.4	830.6	814.5	797.8	780.1
		50	858.1	843.6	829.1	813.9	797.6
1-Heptanol	$C_7H_{16}O$	0.101	836.4	819.1	801.1	782.3	762.5
		5	839.1	822.2	804.6	786.3	767.1
		10	841.7	825.2	808.1	790.3	771.6
		25	849.3	833.8	817.8	801.2	783.7
		50	860.6	846.4	831.8	816.7	800.7
1-Octanol	$C_8H_{18}O$	0.101	838.8	821.7	804.1	785.5	766.0
		5	841.4	824.7	807.5	789.5	770.5
		10	844.0	827.7	810.8	793.3	774.8
		25	851.4	836.0	820.2	803.9	786.7
		50	862.4	848.3	833.9	819.0	803.3

ploying a magnetic suspension system (Fig. 3.7). The magnetic suspension coupling consists of an electromagnet, a permanent magnet, a position transducer, and a control system. The electromagnet is attached at the underfloor weighing hook of a commercial analytic balance. Inside the coupling housing there is a permanent magnet to which the sinker to be weighed is linked by means of a load coupling and decoupling de-

Table 3.5 Density ρ (kg m^{-3}) of some refrigerants in the liquid phase

		P (MPa)	248.15 K	273.15 K	298.15 K	323.15 K	348.15 K
R22	$CHClF_2$	5	1375	1299	1214	1113	975.0
		10	1386	1315	1238	1149	1043
		25	1416	1355	1290	1217	1140
R32	CH_2F_2	5	1148	1070	980.7	865.0	
		10	1162	1088	1006	910.1	857.7
		25	1194	1128	1058	982.3	1019.8
R124	C_2HClF_4	5	1518	1450	1380	1303	1202
		10	1526	1462	1402	1338	1247
		25	1547	1496	1454	1408	1330
R125	C_2HF_5	5	1447	1349	1236	1086	
		10	1466	1376	1279	1167	
		25	1510	1436	1359	1282	
R134a	$C_2H_2F_4$	5	1386	1312	1229	1135	1017
		10	1399	1328	1252	1168	1075
		25	1432	1368	1302	1234	1166
R141b	$C_2H_3ClF_2$	5	1328	1287	1244	1197	1147
		10	1333	1294	1253	1209	1163
		25	1345	1311	1276	1239	1200
R152a	$C_2H_4F_2$	5	1022	971.3	914.8	850.7	774.1
		10	1030	981.9	929.4	871.9	808.5
		25	1051	1008	962.8	915.6	867.3

vice. The upper part of the coupling housing which separates the permanent magnet from the electromagnet is manufactured of a magnetically neutral metal, namely copper beryllium. To achieve the freely suspended state of the permanent magnet, its absolute position is detected by a position sensor and controlled via a proportional–integral–differential controller. By means of a superimposed set-point controller and an additional control system, several vertical motions of the permanent magnet are generated automatically. In this way, soft up- and downward movements of the permanent magnet can be realized, and via the load coupling and decoupling device the solid quartz glass cylinder working as sinker can be coupled and decoupled.

In the tare position, the permanent magnet is suspended at a relatively large distance from the top of the coupling housing, the sinker is decoupled from the permanent magnet, and the balance can be tared to zero. In order to achieve the measuring position, the electronic control unit of the magnetic suspension coupling brings the permanent magnet closer to the top of the coupling housing. This means that the bearing cone also moves upwards and takes the measuring load cage with which the sinker is connected. In this way, the sinker is coupled with the balance and can be weighed.

In order to measure the density of the fluid in the measuring cell, the sinker is coupled and decoupled several times (changes between the tare and measuring position), so that the buoyancy force upon the sinker can be more accurately determined by averaging. Then, the density of the fluid can be determined from the simple relation,

$$\rho = \frac{(m_\mathrm{s} - m_\mathrm{s,fluid})}{V_\mathrm{s}(T, P)} \,. \tag{3.7}$$

In this equation, m_s is the true mass of the sinker (weighed in the evacuated measuring cell), $m_\mathrm{s,fluid}$ is the apparent mass of the sinker (weighed in the fluid-filled measuring cell), and $V_s(T, P)$ is the temperature and pressure dependent volume of the sinker.

This instrument was successfully employed for many measurements over a very wide range of conditions with an uncertainty of better than $2 \times 10^{-4} \rho$.

The group in Bochum, headed by Prof. W. Wagner, also has other types of densimeter based upon similar principles. Here, we only mention two other very successful designs. The two-sinker densimeter developed by *Kleinrahm* and *Wagner* [3.26] in 1986 automatically compensated all incidental effects (such as the zero-point shift of the balance, buoyancy forces on auxiliary

Table 3.6 Density ρ (kg m^{-3}) of some gases

		P (MPa)	273.15 K	298.15 K	323.15 K	348.15 K	373.15 K
Argon	Ar	0.101	1.778	1.628	1.502	1.394	1.300
		5	91.75	82.71	75.39	69.36	64.30
		10	189.1	168.1	151.7	138.6	127.8
Hydrogen	H_2	0.101	0.089	0.082	0.075	0.070	0.065
		5	4.23	3.89	3.60	3.35	3.13
		10	8.09	7.46	6.92	6.46	6.06
Nitrogen	N_2	0.101	1.246	1.141	1.052	0.997	0.911
		5	62.44	56.47	47.64	47.64	44.26
		10	124.4	111.6	101.5	93.3	86.5
Oxygen	O_2	0.101	1.424	1.304	1.203	1.116	1.041
		5	73.67	66.36	60.48	55.63	51.55
		10	152.2	135.1	121.8	111.2	102.6
Carbon monoxide	CO	0.101	1.246	1.141	1.052	0.977	0.911
		5	62.94	56.82	51.89	47.82	44.40
		10	126.1	112.8	102.3	93.9	86.9
Carbon dioxide	CO_2	0.101	1.970	1.802	1.660	1.540	1.436
		5		130.52	104.46	90.21	80.48
		10			379.6	230.6	186.9
Sulfur dioxide	SO_2	0.101	2.908	2.649	2.435	2.254	2.099
Hydrogen sulfide	H_2S	0.101	1.532	1.4	1.29	1.195	
		5				85.78	
Methane	CH_4	0.101	0.715	0.655	0.604	0.56	0.522
		5	40.05	35.3	31.73	28.91	26.61
		10	89.6	75.7	66.4	59.5	54.1
Ethane	C_2H_6	0.101	1.351	1.235	1.137	1.054	0.982
		5			91.8	70.97	60.53
		10			314.7	223.6	158.98
Propane	C_3H_8	0.101	2.004	1.826	1.678	1.554	

devices, adsorption effects, surface tension, etc.) that reduce the accuracy of the density measurement when only a single sinker is employed. In 2002, the same group developed an absolute viscometer–densimeter [3.27] for measurements on gases, that operates with a 0.15–0.4% uncertainty in viscosity and 0.02–0.05% in density.

Various other investigators employed densimeters. based upon the same principle. *Masui* [3.28] employed an optical sensing system fed by a fibre optic as a feedback control to stabilize the buoy support. *Masui* [3.28] measured the density of toluene from 298 to 423 K and pressures up to 30 MPa, with an estimated uncertainty of 0.025%. A similar magnetic suspension densimeter was employed by *Toscani* et al. [3.29] for density measurements of liquids and liquid mixtures. This instrument covered a temperature range from 295 to 400 K at pressures up to 100 MPa, with an uncertainty of ±0.2%. *Okada* et al. [3.30], developed a magnetic densimeter, in which the float consists of a hollow glass body containing a soft-iron core.

3.1.5 Density Reference Values

The density of water is still widely employed as a liquid density standard. The equation developed by *Wagner* and *Pruß* [3.31] was adopted by the International Association for the Properties of Water and Steam (IAPWS) in 1995. The IAPWS formulation for the thermodynamic properties of ordinary water substance for both scientific and general use is called IAPWS 1995 (IAPWS-95) [3.32]. It represents all of the thermodynamic properties of water from the melting line (251.2 K

at 209.9 MPa) to a temperature of 1273 K and pressures up to 1 GPa. In this entire range IAPWS 95 represents the most accurate measurements to within the experimental uncertainty. Values of density at specific temperature and pressure points are given at Table 3.1.

3.1.6 Tables of Density Values

In Tables 3.2–3.6, the density of commonly encountered fluids is given for engineering purposes, as a function of temperature and pressure. The fluids and the temperature and pressure conditions chosen are the same for the density, viscosity and thermal conductivity discussed in the present section and in Sects. 3.4 and 3.5.

Values for the liquid density are based on a large collection of experimental data critically assessed (*n*-alkanes [3.33], *n*-alkenes [3.34], *n*-alcohols [3.35], refrigerants [3.36]). The uncertainty of the quoted liquid density values is much better than ±0.3%. Values for the gas-phase density have been obtained from corresponding-states software [3.37] with an estimated uncertainty better than ±0.5%.

3.2 Surface Tension and Interfacial Tension of Liquids

This chapter presents the concepts of surface and interfacial tensions, their dependencies, measurement, and prediction. It starts with an explanation of the surface tension of pure liquids and its temperature dependence. Then, the surface tension of solutions is presented, and useful correlations for the dependence of surface tension on the solute concentration are suggested. Next, the concept of interfacial tension associated with two dense phases is explained, and its relationship with the surface tensions of the two phases is discussed. The Young–Laplace equation that correlates the pressure difference across an interface with interfacial tension and curvature is presented. Various methods for measurement of surface and interfacial tension are discussed, based on the theoretical background previously explained. Finally, selected surface tension values are tabulated, and a method for predicting surface tension from other thermodynamic properties is shown.

3.2.1 Surface Tension of Pure Liquids

Observations Intuitive Concepts, and Definitions

It is well known that small liquid drops are almost spherical even under the influence of gravity, while large drops are distorted from sphericity under the effect of gravity. Also, many types of small solid particles (and insects such as striders) can float or move on water even if their density is higher than that of water, while large particles of such density readily pass through the water surface. Clearly, therefore, there exists a force that acts on particles in general, which becomes more pronounced as they become smaller. A complementary well-known fact is that, as particles become smaller, the ratio of their surface area to their volume increases. For example, the surface area of a sphere of radius R is proportional to R^2, while its volume is proportional to R^3; therefore, the ratio of surface area to volume is proportional to $1/R$, which strongly increases as R decreases. Thus, it is reasonable to suspect that the force acting on small particles is associated with their interfaces.

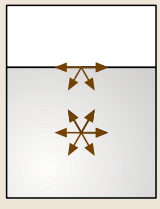

Fig. 3.8 A schematic comparison of the forces acting on a molecule near a surface, and a molecule in the bulk

Thinking from a molecular point of view, the net force acting on a molecule near a surface must be different from that acting on a molecule deep in the bulk, simply because of symmetry considerations. This is schematically demonstrated in Fig. 3.8. Thus, the energy of a molecule near a surface must be different from that of the same molecule in the bulk. Based on this general picture, Gibbs developed a formalism that defines surface energy as the difference between the actual energy of a system and the sum of the energies of its components had there been no interface between them. In Gibbs' approach, the interface is considered a mathematical surface of no thickness, in line with macroscopic observations. The surface energy per unit area of a liquid surface in contact with vapor (or, in general, with a gas) is its surface tension. If the liquid is in contact with a dense phase, such as another immiscible liquid or a solid, the corresponding terms that are used are *interfacial energy* and *interfacial tension*. The latter will be

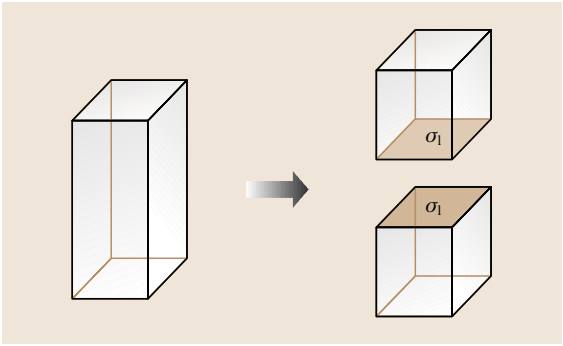

Fig. 3.9 An imaginary experiment that creates two new surfaces by breaking an infinite liquid body into two parts, and removing them to a large distance from each other

used below as a general term, whenever both interfacial tension and surface tension are implied. For completeness, it should be mentioned that Bakker and van der Waals developed a different approach, in which the interface is considered as a thin, but three-dimensional region. For practical purposes, the two approaches lead to the same conclusions.

It may also be useful to regard surface energy as the energy needed to create a surface. In the imaginary experiment shown in Fig. 3.9, an infinite body of a liquid is separated into two parts that are removed from each other to a sufficiently large distance, so their interaction energy is negligible. The energy per unit interfacial area needed for this separation is termed the *work of cohesion* E_c since it overcomes the cohesion between the molecules of a single species. It is equal to twice the surface tension of the liquid σ_l since two new surfaces were created in this experiment. Thus,

$$\sigma_l = \frac{E_c}{2} \,. \tag{3.8}$$

Another imaginary experiment may shed a different light on the surface tension concept. Figure 3.10 shows a thin frame with three fixed sides and a movable bar as a fourth side. If a liquid film (such as a soap film) is formed on this frame, then a force F has to be applied to the movable bar in order to increase the surface area of the film. The work done by this force is Fd, where d is the path length. This work is transformed into surface energy $2\sigma_l Ld$, where L is the width of the frame (the factor 2 stands for the two sides, top and bottom, of the liquid film). Thus

$$\sigma_l = \frac{F}{2L} \,. \tag{3.9}$$

This result shows that surface tension can also be interpreted as a force per unit length. This interpretation is

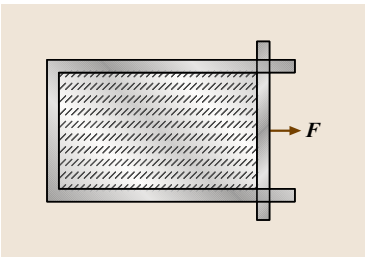

Fig. 3.10 Top view of a liquid film on a frame with a movable side. A force acting on the movable side is required to increase the surface area of the film

useful as a basis for some of the methods for surface tension measurement.

Based on the above definitions, the units in which surface tension is measured should be J/m^2 or N/m. Actually, for convenience, surface tension is usually expressed in mN/m (millinewtons per meter). The reason for this choice is that this unit is equivalent to dynes/cm that had been used for many years. Thus, by adopting the units of mN/m, the numerical values of surface tension were unchanged by the transition to SI units. Typical surface tension values for regular liquids are in the range of ≈ 14 to ≈ 73 mN/m at about room temperature. The higher end of this range corresponds to water. Liquid metals have much higher surface tension: mercury, for example, has a surface tension of ≈ 486 mN/m at room temperature.

In most practical applications, the surface tension of a pure liquid is considered independent of the size of the system. Thus, the surface tension of a small drop of a liquid is assumed the same as for a large drop. A priori, based on molecular interactions reasoning, it can be argued that this constancy may not hold for very small drops. This indeed is the case, however it was experimentally demonstrated that a drop has to be almost molecular in size in order to observe size dependence of its surface tension.

Temperature Dependence

At the critical temperature T_c there is no distinction between a liquid and its vapor. In other words, no interface exists between them. Thus, the surface tension of a liquid at the critical temperature must be, by definition, zero. This observation indicates that, in general, for most liquids, surface tension decreases as the temperature is increased. Since no exact theory seems to exist, the quantitative dependence of surface tension on the absolute temperature T (in K) can be estimated by semi-empirical, approximate expressions. A useful expression

is the Eötvös equation, which reads

$$\sigma_l V^{2/3} = c(T_c - T)\,, \tag{3.10}$$

where V is the molar volume in m^3, c is a constant, which for many liquids has the value of approximately 2.1×10^{-4} J/K, and σ_l is measured in mN/m.

Another useful expression is the van der Waals–Guggenheim equation

$$\sigma_l = \sigma^0 \left(1 - \frac{T}{T_c}\right)^n\,, \tag{3.11}$$

where σ^0 is a constant typical to the liquid, in the same units as σ_l, and n equals 11/9 for many organic liquids. The usefulness of these two expressions lies in their approximate universality in terms of the values of c or n.

3.2.2 Surface Tension of Liquid Solutions

Concepts and General Examples

In many practical processes, solutions rather than pure liquids are employed. Therefore, understanding surface tension of solutions is essential. In principle, solutes may increase the surface tension or decrease it. According to a fundamental, thermodynamic theory developed by Gibbs, the effect of a solute on surface tension depends on the tendency of the solute to concentrate at the solution–air interface. If the solute tends to concentrate at the interface more than in the bulk, an increase in its concentration will decrease the surface tension.

Figure 3.11 shows typical dependencies of surface tension on concentration in aqueous systems. Figure 3.11a shows the effect of a typical electrolyte (NaCl) dissolved in water. As can be clearly seen, the addition of the electrolyte increases the surface tension beyond that of water. However, very large concentrations are required for a relatively small increase in surface tension. Clearly, the electrolyte prefers to be in the bulk rather than at the surface. Figure 3.11b shows a typical effect of a soluble organic liquid in water (propanol). The surface tension gradually decreases from that of pure water to that of the solute. The decrease is steeper at lower concentrations of the solute and shallower at higher concentrations. The fact that the surface tension decreases indicates that the organic solute prefers to concentrate at the interface. This is understandable from a molecular point of view, because a molecule of an organic materials always has a hydrophobic (water-fearing) part in it, which tends to stay away from water as much as possible.

When an organic molecule has a polar part together with a dominant hydrophobic part, the solubility in the bulk is small, and the molecule tends to adsorb mostly at the surface. Such amphiphilic molecules are referred to as *surface-active agents* or *surfactants*. Figure 3.11c

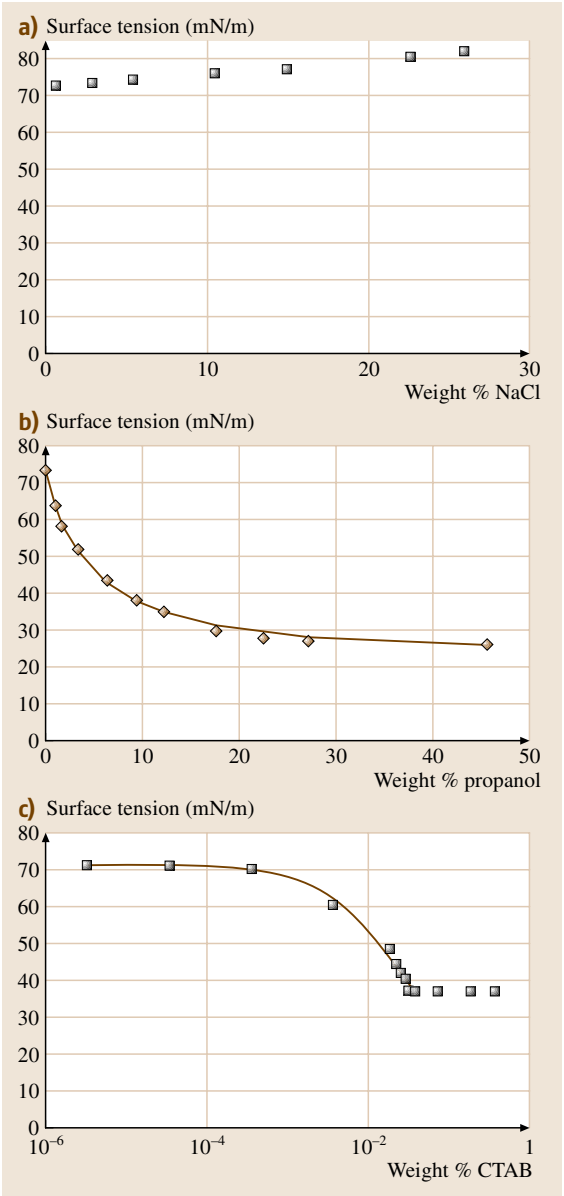

Fig. 3.11a–c Typical surface tension dependence on solute concentration in aqueous solutions: **(a)** an electrolyte (NaCl); **(b)** a soluble organic liquid (propanol, the curve represents a fit of the Connors and Wright equation); **(c)** a surfactant (CTAB in PBS, the curve represents a fit of the Szyszkowski equation)

shows a typical dependence of the surface tension on concentration for a surfactant (cetyl trimethyl ammonium bromide in phosphate buffer solution, CTAB in PBS). Two features are very prominent in this figure:

1. the surfactant concentration that leads to a meaningful reduction in surface tension is orders of magnitude smaller than for a soluble organic material; and
2. above a certain concentration the surface tension remains constant.

The latter is called the *critical micelle concentration* (CMC), since at this and higher concentrations of the surfactant, its molecules in the bulk aggregate in structures called *micelles*. This aggregation is an alternative to adsorbing at the liquid-air surface. The hydrophobic parts of the molecules are hidden inside the micelles in order to minimize their interaction with water, instead of being exposed to air at the interface. A spherical micelle is shown schematically in Fig. 3.12. Micelles exist in many geometrical forms, a topic which is extensively covered in textbooks and in the research literature, and which is of the utmost importance in biology (cell membrane formation by lipids). It is also interesting to note that *reverse micelles* can form in organic liquids, where the polar parts of the surfactant molecules will be *hidden* from the solvent.

Useful Surface Tension Correlations

Unfortunately, the theory regarding surface tension of solutions is not yet sufficiently developed to yield exact, general equations. Therefore, semi-empirical correlations need to be used. Two useful correlations are presented below, one that is useful for very low concentrations, and the other for relatively high concentrations.

For low concentrations, the von Szyszkowski equation may be used

$$\sigma_l = \sigma_0 - RT\Gamma_\infty \ln\left(1 + \frac{C}{b}\right), \qquad (3.12)$$

where σ_0 is the surface tension of the pure solvent, R is the universal gas constant, C is the molar concentration of the solute, and Γ_∞ and b are two empirical constants to be determined by the best fit to experimental data. In the simplified theory underlying this equation, Γ_∞ is the saturation surface concentration (mols per unit area) of the adsorbed molecules at the surface. The curve in Fig. 3.11c shows an example of a fit of this equation to experimental data. The fit is excellent all the way to the CMC.

At higher concentrations, an equation developed by *Connors* and *Wright* [3.38] may be employed

$$\sigma_l = \sigma_0 - (\sigma_0 - \sigma_s)\left(1 + \frac{\beta(1-x)}{1-\alpha(1-x)}\right)x, \qquad (3.13)$$

where σ_s is the surface tension of the pure solute, x is the molar fraction of the solute, and α and β are the two empirical constants to be determined. It is clear that at $x = 0$ this equation indeed predicts the surface tension to be that of the pure solvent, σ_0, and at $x = 1$ that of the pure solute, σ_s. Figure 3.11b shows that this equation can fit data very well for intermediate concentrations.

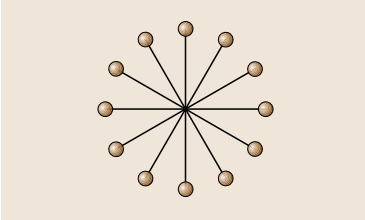

Fig. 3.12 A schematic of a spherical micelle

3.2.3 Interfacial Tension

Work of Adhesion

The concept of interfacial tension can be demonstrated and understood by following an imaginary experiment, similar to that used for introducing the surface tension concept. Suppose, as shown in Fig. 3.13, that two semi-infinite bodies of different materials, a and b, are separated from each other to a sufficiently large distance, so their interaction energy is negligible. At the beginning of the process, the interfacial energy per unit interfacial area is σ_{ab}, while at the end the sum of the surface energies per unit area is $(\sigma_a + \sigma_b)$. The energy per

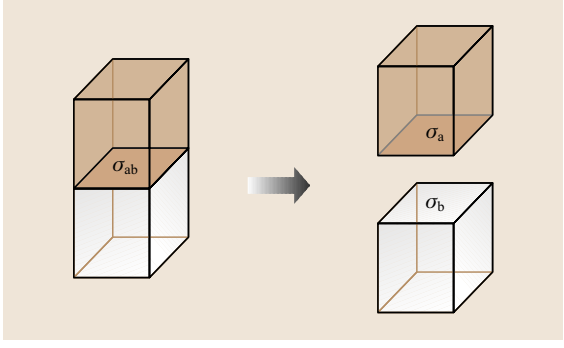

Fig. 3.13 An imaginary experiment that creates two new surfaces by separating two semi-infinite bodies of different materials at the interface between them, and removing them to a large distance from each other

unit interfacial area needed to achieve this separation, E_a, is termed the *work of adhesion*, and the interfacial tension can be expressed as

$$\sigma_{ab} = \sigma_a + \sigma_b - E_a \,. \tag{3.14}$$

Thus, if one can independently calculate E_a, the interfacial tension can be calculated from the individual surface tensions.

Calculation of Interfacial Tension from Surface Tensions

Unfortunately, an exact, general calculation of the work of adhesion is not yet possible. Therefore, some useful approximations have been developed over the years. *Girifalco* and *Good* [3.39] presented the first useful correlation:

$$E_a = 2\phi\sqrt{\sigma_a \sigma_b} \,, \tag{3.15}$$

where ϕ is a dimensionless correction factor, covering for the uncertainty in the equation. Values of ϕ for liquid–fluid systems were measured to be in the range of 0.6–1.2, so the uncertainty in this equation is meaningful.

Fowkes [3.40] developed another approach. In his approach, surface tension consists of two contributions: that of dispersion (London–van der Waals) forces and that of other sources, such as hydrogen bonding, for example:

$$\sigma = \sigma^{\mathrm{d}} + \sigma^{\mathrm{h}} \,. \tag{3.16}$$

Here, σ is surface tension in general, the superscript d stands for dispersion (London–van der Waals) forces, and the superscript 'h' stands for hydrogen bonding. In addition, the work of adhesion between two non-similar phases (e.g., an aqueous phase and a nonpolar phase) depends only on the nonpolar interactions between them. Therefore,

$$E_a = 2\sqrt{\sigma_a^{\mathrm{d}} \sigma_b^{\mathrm{d}}} \tag{3.17}$$

Owens and *Wendt* [3.41] generalized this approach by considering the surface tension to include, in general, also a polar (nondispersive) contribution: $\sigma = \sigma^{\mathrm{d}} + \sigma^{\mathrm{p}}$, where the superscript 'p' stands for the polar contributions. Then, the work of adhesion becomes

$$E_a = 2\sqrt{\sigma_a^{\mathrm{d}} \sigma_b^{\mathrm{d}}} + 2\sqrt{\sigma_a^{\mathrm{p}} \sigma_b^{\mathrm{p}}} \,. \tag{3.18}$$

By comparing (3.18) with (3.15), an expression for the Girifalco–Good correction factor can be derived

$$\phi = \sqrt{\frac{\sigma_a^{\mathrm{d}} \sigma_b^{\mathrm{d}}}{\sigma_a \sigma_b}} + \sqrt{\frac{\sigma_a^{\mathrm{p}} \sigma_b^{\mathrm{p}}}{\sigma_a \sigma_b}} \,. \tag{3.19}$$

This equation can be used to roughly estimate the value of ϕ. For water, $\sigma^{\mathrm{d}}/\sigma \approx 0.3$, so for the case of an interface between water and a completely nonpolar liquid ($\sigma^{\mathrm{p}} = 0$), $\phi = 0.3^{1/2} \approx 0.55$. This value agrees well with the lowest end of the experimentally measured ϕ. However, the highest value of ϕ according to (3.19) is 1, which is lower than the experimentally derived value of about 1.2. Thus, while (3.19) is probably a good approximation, it is still not sufficiently accurate. Other correlations and approaches that are based on various contributions to surface tension can also be found in the literature.

In order to elucidate the surface tension components of a polar liquid (say liquid a), its interfacial tension with a nonpolar liquid (b) should be measured. In this case, $\sigma_b^{\mathrm{p}} = 0$, $\sigma_b^{\mathrm{d}} = \sigma_b$, and $\phi = \sqrt{\sigma_a^{\mathrm{d}}/\sigma_a}$. Thus, calculation of ϕ from interfacial tension measurement yields σ_a^{d}. Obviously, it is advisable to repeat the measurement with a few nonpolar liquids and get an average result. For example, the nonpolar liquids *n*-hexane, *n*-heptane, *n*-octane and *n*-decane all have a ϕ of 0.55 with water at 20 °C. Consequently, $0.55 = \sqrt{\sigma_w^{\mathrm{d}}/\sigma_w} = \sqrt{\sigma_w^{\mathrm{d}}/72.8}$, or $\sigma_w^{\mathrm{d}} \cong 22\,\mathrm{mN/m}$ and $\sigma_w^{\mathrm{p}} \cong 50.8\,\mathrm{mN/m}$. Benzene has a surface tension of 28.9 mN/m and a ϕ of 0.72 with water at 20 °C. Therefore, by (3.19), $0.72 = \sqrt{\frac{22\sigma_b^{\mathrm{d}}}{72.8 \cdot 28.9}} + \sqrt{\frac{50.8(28.9-\sigma_b^{\mathrm{d}})}{72.8 \cdot 28.9}}$, and it turns out that $\sigma_b^{\mathrm{d}} \cong 27.5\,\mathrm{mN/m}$. As expected, this value is quite close to the surface tension itself.

3.2.4 Implications of Surface and Interfacial Tension on Liquid–Fluid Systems

Surface Curvature

The effect of surface and interfacial tension in liquid–fluid systems is closely related to the curvature of their interfaces. Therefore, the basic principles of curvature definition are explained in the following.

For a two-dimensional sufficiently smooth curve, the local radius of curvature is the radius of the circle drawn using three infinitesimally close points on the curve (Fig. 3.14). Radii of curvature may be defined as negative or positive, depending on whether the curve is concave or convex. For a three-dimensional surface, the mean curvature H at a given point is defined by the following average

$$2H = \frac{1}{R_1} + \frac{1}{R_2} \,; \tag{3.20}$$

R_1 and R_2 are the principal two-dimensional radii of curvature of the curves of intersection between the sur-

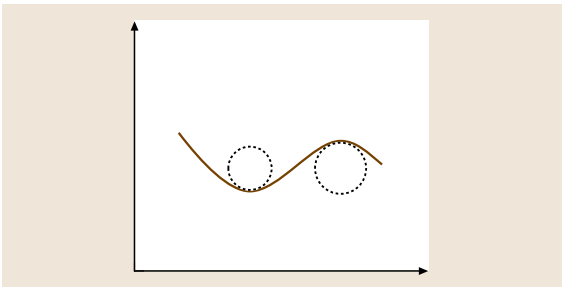

Fig. 3.14 Examples of the local radius of curvature of a two-dimensional curve (the two local radii of curvature shown in the figure have opposite signs)

face and two perpendicular planes (the principal cross sections, Fig. 3.15). It is important to realize that H is invariant to the orientation of the two planes, as long as they are perpendicular to each other.

For example, the mean curvature of a sphere is $1/R$, where R is the sphere radius, since in this case $R_1 = R_2 = R$. For a cylinder, it is convenient to choose one of the perpendicular planes to be parallel to the axis of the cylinder (so that $R_1 = \infty$) and the other perpendicular to the axis (so that $R_2 = R$, the cylinder radius). Thus, for a cylinder $H = 1/(2R)$.

Pressure Difference across Curved Interfaces

For large liquid–fluid systems, the interfaces of which have zero curvature, the pressure at equilibrium must be equal on the two sides of the interface. However, when the interfacial curvature is nonzero, a pressure difference across the interface must exist at equilibrium. The magnitude of this pressure is given by the Young–Laplace equation

$$P_\mathrm{i} - P_0 = 2\sigma_\mathrm{lf} H = \sigma_\mathrm{lf}\left(\frac{1}{R_1} + \frac{1}{R_2}\right) , \qquad (3.21)$$

where P_i is the pressure at the side of the interface for which the radius of curvature is defined, P_o is the pressure at the other side of the interface, and σ_lf is the interfacial tension between the liquid and the fluid. For simple shapes, such as a bubble or a drop, P_i and P_o can be interpreted as the inside and outside pressure, respectively.

Thus, for example, for a spherical body

$$P_\mathrm{i} - P_\mathrm{o} = \frac{2\sigma_\mathrm{lf}}{R} . \qquad (3.22)$$

It is important to notice that this equation does not differentiate between a fluid (e.g. air) bubble and a liquid drop: the pressure is always higher inside the curved body, whether it is a bubble or a drop. For a cylindrical body the pressure difference is given by

$$P_\mathrm{i} - P_\mathrm{o} = \frac{\sigma_\mathrm{lf}}{R} . \qquad (3.23)$$

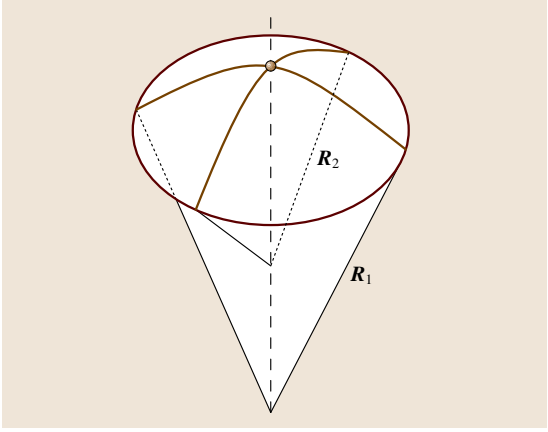

Fig. 3.15 Intersection curves of a three-dimensional surface with two perpendicular planes

3.2.5 Measurement of Surface Tension and Interfacial Tension

Force Methods

Some surface tension measurement methods use force measurements, as described below. These methods employ the concept of surface tension (or interfacial tension) being a force per unit length.

Drop Weight. The idea underlying this method is that a drop remains attached to a capillary as long as the interfacial tension force balances its weight. This is shown

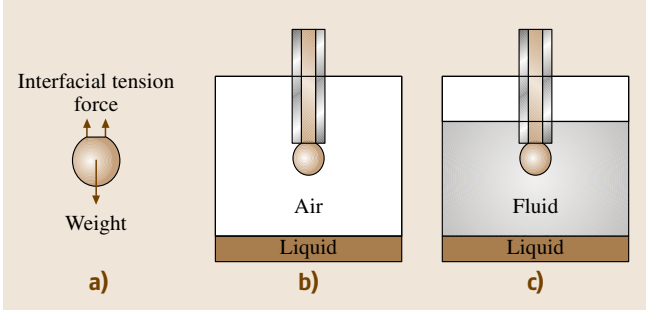

Fig. 3.16a–c The drop weight method: **(a)** the approximate force balance; **(b)** surface tension measurement; **(c)** interfacial tension measurement (the fluid is a lighter surrounding liquid)

schematically in Fig. 3.16a. According to this simplistic argument, the interfacial tension force at detachment equals the weight of the detached drop W_d. The force due to interfacial tension is assumed to be $2\pi r\sigma_{lf}$, where r is the radius of the capillary (interfacial tension is considered as force per unit length). Thus, in principle, weighing a drop and measuring the radius of the capillary enable the calculation of the interfacial tension.

However, the detachment process is much more complex than assumed above. Actually, the detachment does not occur at the line of contact between the liquid and the capillary, but through the formation of a narrowing neck in the drop itself. Therefore, the static picture of a balance between gravity and the interfacial tension force needs to be complemented. The dynamic process of detachment is rather complicated, and can be described only with the help of rather sophisticated numerical simulations. Thus, the practical solution to the problem is to add a correction factor, f_W, to the static balance equation:

$$W_d = 2\pi r\sigma_l f_W \,. \tag{3.24}$$

The correction factor turns out to depend on the dimensionless ratio between the radius of the capillary and the cubic root of the volume V of the drop: $f_W = f_W(r/V^{1/3})$. Figure 3.17 shows an approximate curve for f_W. Since the detachment process is dynamic, (3.24) may need also to be corrected for the viscosity of the liquid, if it is very high. Information about the effect of viscosity is still incomplete. Still less is known on a significant effect of the elastic stresses developing in non-Newtonian viscoelastic polymer solutions (even in the most dilute ones).

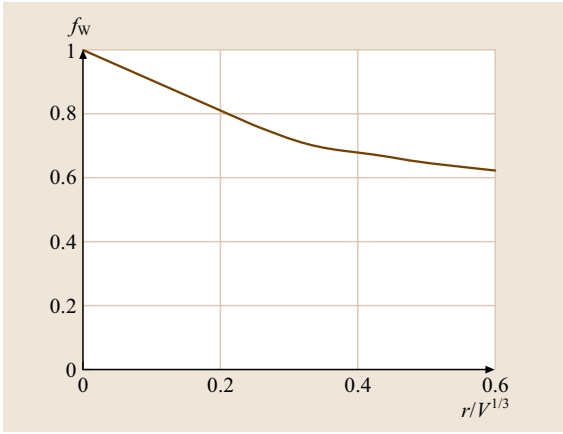

Fig. 3.17 An approximate curve for f_W, the correction factor for the drop weight method

From a practical point of view, the drop weight method is a convenient, inexpensive method that can give good interfacial tension results. It may be especially useful when relative changes in interfacial tension are more important than very accurate, absolute values. The drop weight is calculated as an average of a sufficiently large number of drops. An automatic drop counter is helpful. The radius of the capillary can be accurately measured, however attention should be given to find out whether the drop hangs on the outer perimeter of the capillary or the inner one. The correction factor is best estimated by calibration of the actual experimental system with liquids of known surface tension. The drop weight method can be used to measure surface tensions (Fig. 3.16b) as well as interfacial tensions (Fig. 3.16c). For the latter purpose, the capillary tip is dipped into the fluid.

The Ring Method. The ring method is described schematically in Fig. 3.18. The principle behind it is somewhat similar to the one underlying the drop weight method: one measures the force needed to detach a wire ring from a liquid–fluid interface. The ring is dipped into the liquid, and then removed until detachment from the liquid occurs. The maximum force measured in this case F_r is the sum of the weight of the ring W_r and the interfacial tension force that acts on the inner as well as outer perimeter of the ring. Since the thickness of the wire of the ring is very small compared with its radius, the two perimeters are considered to be of the same radius R_r. As in the case of the drop weight method, the detachment process is complex, therefore a correction factor f_r is required in order to calculate the exact interfacial tension from the simplistic force balance. Thus

$$F_r = W_r + 4 f_r \pi R_r \sigma_{lf} \,. \tag{3.25}$$

f_r depends on two dimensionless ratios: $f_r = f_r(R_r/V_r^{1/3}, R_r/r_r)$, where V_r is the meniscus volume

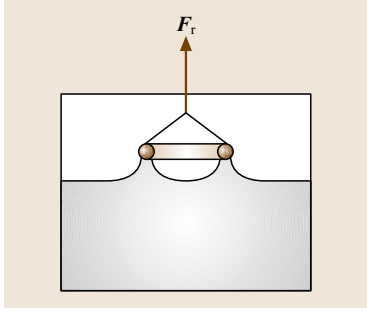

Fig. 3.18 A schematic of the ring method

(liquid carried by the ring above the bulk level), and r_r is the cross-sectional radius of the wire.

One of the main advantages of this method is that it can be easily automated and calibrated to give a surface tension reading. The f_r dependence is then an integral part of the instrument software. The main disadvantage of this method is its sensitivity to the cleanliness of the wire (usually a platinum wire). Also, the wire has to be perfectly planar in order to avoid distortions of the interface that may interfere with the measurement and calculations. The ring method may be used for measuring interfacial tensions as well as surface tensions.

Wilhelmy Plate. The Wilhelmy plate method is similar to the ring method, however a thin, vertical plate is used instead of a ring (Fig. 3.19). The main advantage is that the force balance at detachment does not need a correction factor, because of the simplicity of the plate geometry and its thinness:

$$F_p = W_p + p_p \sigma_{lf} \,. \tag{3.26}$$

In this equation, F_p is the force measured by the balance, W_p is the weight of the plate, and p is the perimeter of its cross section. The Wilhelmy plate method is useful for measuring interfacial tensions as well as surface tensions.

Shape Methods

The shape methods for surface tension measurement take advantage of the fact that the shape of a drop at equilibrium is determined by a balance between external forces (e.g., gravity) and surface or interfacial tension. A drop used in these methods may be hanging from a capillary (*pendant drop*) or on top of a horizontal solid surface (*sessile drop*). When external forces are negligible, the drop must be spherical, independently of interfacial tension. However, when external forces are sufficiently large to distort the shape of the drop from sphericity, the details of its shape depend also on interfacial tension. Recording the shape enables the calculation of interfacial tension from (3.21).

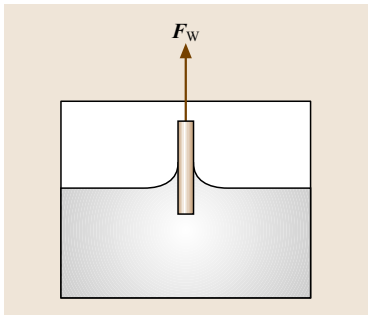

Fig. 3.19 The Wilhelmy plate method

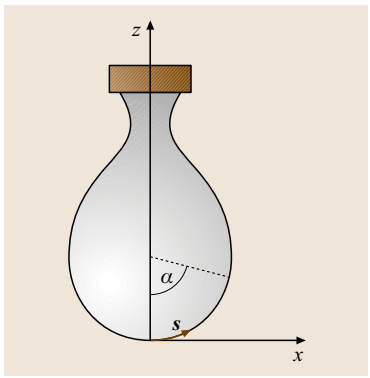

Fig. 3.20 A pendant drop with the variables used in the calculation of its shape

Drop Shape. In this method, the shape of a drop is recorded, digitally analyzed, and compared with theoretical calculations. The drop must be sufficiently large, so that the effect of gravity on its shape is meaningful. The drop must also be axisymmetric, in order to enable comparison with available theoretical calculations. The objective of the comparison with theory is to find the interfacial tension value that leads to the best fit between the recorded and calculated shapes.

For these calculations, (3.21) is transformed in the following way for the case of a pendant drop (Fig. 3.20). Very similar arguments apply to sessile drops. First, the pressure difference at each point across the interface is expressed as

$$P_i - P_o = (P_i - P_o)_{z=0} - \Delta\rho g z \,, \tag{3.27}$$

where x and$z$ are the coordinates for describing the drop shape (Fig. 3.20), the point ($x = 0$, $z = 0$) is the drop apex, $(P_i - P_o)_{z=0}$ is the pressure difference at the drop apex, $\Delta\rho$ is the density difference between the liquid and the fluid, and g is the gravitational acceleration.

Then, for an axisymmetric drop, the expressions for the radii of curvature become

$$\frac{1}{R_1} = \frac{(\mathrm{d}\sin\alpha)}{\mathrm{d}x} \,, \tag{3.28}$$

where R_1 is the principal radius of curvature in a drop cross section that includes the z-axis and

$$\frac{1}{R_2} = \frac{(\sin\alpha)}{x} \,, \tag{3.29}$$

where R_2 is the principal radius of curvature in a plane perpendicular to the above cross section, at the point (x,

z). α is the angle between the drop axis and the normal to the drop interface (Fig. 3.20). When (3.27–3.29) are introduced in (3.21), the result is a first-order differential equation in α

$$\frac{\mathrm{d}\sin\alpha}{\mathrm{d}x} = \frac{(P_\mathrm{i}-P_\mathrm{o})_{z=0}}{\sigma_\mathrm{lf}} - \frac{\Delta\rho g z}{\sigma_\mathrm{lf}} - \frac{\sin\alpha}{x} \,. \tag{3.30}$$

Due to the symmetry at the apex, $R_1 = R_2$. Therefore

$$\frac{(P_\mathrm{i}-P_\mathrm{o})_{z=0}}{\sigma_\mathrm{lf}} = \frac{2}{b} \,, \tag{3.31}$$

where b is the radius of curvature at the apex. Thus, (3.30) finally reads

$$\frac{\mathrm{d}\sin\alpha}{\mathrm{d}x} = \frac{2}{b} - \frac{\Delta\rho g z}{\sigma_\mathrm{lf}} - \frac{\sin\alpha}{x} \,. \tag{3.32}$$

However, there are still two independent variables, x and z. To solve this problem, the integration is done along the generatrix of the drop interface, introducing the arc length from the apex, s, as variable. The variables x and z are related to s by (Fig. 3.20)

$$\mathrm{d}x = \cos\alpha\,\mathrm{d}s \tag{3.33}$$

and

$$\mathrm{d}z = \sin\alpha\,\mathrm{d}s \,. \tag{3.34}$$

The arc length should also be introduced as a variable in (3.32), where $\mathrm{d}\sin\alpha/\mathrm{d}x$ is replaced by $\mathrm{d}\alpha/\mathrm{d}s$. Then, (3.32–3.34) constitute a set of three differential equations that are solved by routine numerical integration methods. The drop shape method has also been automated.

Rotating Cylinder. In this method, the shape of a drop is determined by a balance between interfacial tension and centrifugal force. A bubble of a fluid is introduced into a horizontal capillary that is filled with a liquid (the density of the liquid is higher than that of the fluid). The capillary rotates around its axis (Fig. 3.21). The centrifugal force increases pressure in the denser liquid, which squeezes the fluid bubble. In the absence of interfacial tension, the fluid bubble would have become a very thin and long cylinder. However, interfacial tension tends to keep the bubble as spherical as possible. The equilibrium between these two forces determines the actual shape of the bubble.

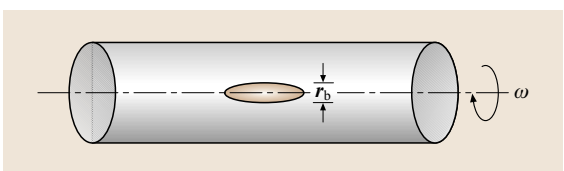

Fig. 3.21 The rotating-cylinder method

If, for simplicity, one assumes the bubble to resemble a cylinder of radius r_b (and finite length), then minimization of the system energy (the sum of the kinetic and interfacial energies) leads to the following approximate equation

$$\sigma_\mathrm{lf} \cong \frac{\left(\omega^2\Delta\rho r_\mathrm{b}^3\right)}{4} \,, \tag{3.35}$$

where ω is the angular velocity of rotation. This equation can be employed to estimate the usefulness of the method. In one assumes an angular velocity of $10^2\ \mathrm{s}^{-1}$, density difference of $0.2\times10^3\ \mathrm{kg/m}^3$, a bubble radius of 10^{-3} m, the resulting interfacial tension is 0.5 mN/m. Thus, this method may be used for the measurement of very low interfacial tensions.

In order to be able to measure the bubble radius while the capillary is rotating, a stroboscopic light is synchronized with the frequency of rotation. Thus, the bubble appears frozen. The main technical difficulty is indeed stabilizing the rotating capillary in such a way that the frozen bubble is amenable to exact measurement of its size. This stabilization is more difficult the higher the frequency of rotation. Therefore, this method is especially useful for low interfacial tensions, for which the rotation frequency does not need to be very high.

Maximum Bubble Pressure

This method is based on a clever way of using (3.21) without the need to measure the radius of curvature of the interface directly. The idea underlying the method is related to the pressure variations inside a bubble that is growing at the tip of a capillary. At the beginning of

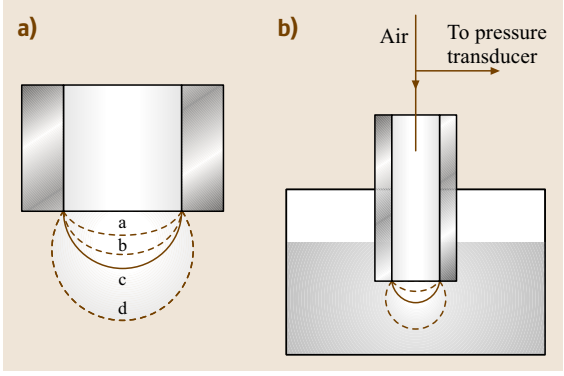

Fig. 3.22a,b The maximum bubble pressure method: Stages in the growing of a bubble

Table 3.7 Selected surface tension values of organic liquids

Group	Material	Surface tension at 20 °C [mN/m]
Acetylenes	1-hexyene	20.98
	1-tridecyne	27.56
Acids (organic)	Formic	37.67
	Isobutyric	25.04
Aldehydes	Acetaldehyde	21.18
	2-furaldehyde	43.76
Alcohols	Ethyl	22.39
	1-decanol	28.88
Alkyl halides	Chloromethane	16.2
	1-iodohexadecane	32.73
Amines	Trimethylamine	13.97
	Phenylhydrazine	45.56
Benzene and its alkyl derivatives	Benzene	28.88
	1-phenyldecane	30.97
Esters, aromatic	Ethyl α-campholanate	27.64
	Benzyl benzoate	45.95
Esters, carboxylic	Isopropyl acetate	22.30
	Methyl acetoacetate	33.09
Ethers	Ethyl methyl ether	15.93*
	Anisole	35.70*
Ketones	Acetone	26.67
	Benzophenone	44.05
Olefins	1-pnetene	16.00
	1-octadecene	28.49
Organosilicon compounds	Tetramethylsilane	12.85
	Tetrapropyl silicate	23.58
Paraffins	Pentane	16.05
	Eicosane	28.87
Perfluoro compounds	Perfluoropentane	9.89
	Perfluorocyclopentane	11.12

* value interpolated between 15 °C and 25 °C

Table 3.8 Selected surface tension values of inorganic liquids

Liquid	Surface tension at 20 °C [mN/m]
Bromine	41.8
Carbon disulfide	32.32
Hydrogen peroxide	75.87
Mercury	486.5
Water	72.88

the process of blowing a bubble, the bubble volume is small, the radius of curvature is large (Fig. 3.22a, stage a, dashed curve), and the pressure is, consequently, low. As the blowing process proceeds and the bubble grows, the radius of curvature *decreases* (Fig. 3.22a stage b, dashed curve), and the pressure *increases*. From a geometric point of view, the lowest possible radius of curvature of the bubble (when it is sufficiently small to be spherical) is the inside radius of the capillary (Fig. 3.22a stage c, solid curve). At this point, the pressure is highest. From this point on, an increase in the bubble volume must be associated with an increase in the radius of curvature (Fig. 3.22a stage d, dashed curve), therefore with a decrease in pressure. Thus, when the pressure is highest (for sufficiently small bubbles), the radius of curvature of the bubble must equal that of the capillary. By identifying the point of maximum pressure, surface tension can be calculated from the measured maximal pressure difference $\Delta P_{\max}$ and the known capillary radius r_c

$$\sigma_l = \frac{\Delta P_{\max} r_c}{2} \,. \tag{3.36}$$

If the bubble is sufficiently large to be distorted by gravity, a corresponding correction must be made to (3.36), based on calculations of the exact shape of the bubble.

From a practical point of view, the system involves blowing gas bubbles into a sample liquid, and continuously measuring the pressure inside the bubble (Fig. 3.22b). This method is more suited to measure surface tension than interfacial tension. The bubbles are continuously blown, and the maximum pressure is recorded over many bubbles. It is important to blow the bubbles as slowly as practically possible, in order to 1. obtain equilibrium values of surface tension, and 2. avoid interactions between successive bubbles, which may interfere with the measurement. The method was neglected for a long time, since accurate pressure transducers were too expensive. Since their price has turned reasonable, this method has become a useful option.

3.2.6 Surface Tension Values for Liquids

Typical, Selected Values

Tables 3.7 and 3.8 present typical, selected surface tension values, taken from the review paper by *Jasper* [3.42]. Effort has been made to include the highest and lowest values of each group, in order to demonstrate the possible value range.

Data on the dependencies of surface tension on temperature for numerous liquids can be found in the book by *Vargaftik* et al. [3.43].

Estimation of Surface Tension

There are a few methods for predicting the surface tension of a liquid from its properties. One of the successful methods for liquids that do not contain hydrogen bonds is the corresponding-state method:

$$\sigma_l = P_c^{2/3} T_c^{2/3} Q \left(1 - \frac{T}{T_c}\right)^{11/9} . \tag{3.37}$$

In this equation, σ_l is given in mN/m, T_c and P_c are the critical temperature and pressure of the liquid in K and Pa, respectively, and T is the temperature.

$$Q = 5.553 \times 10^{-5} \left[1 + \frac{\frac{T_b}{T_c} \ln(P_c/1.013 \times 10^5)}{1 - T_b/T_c}\right] - 1.293 \times 10^{-4} . \tag{3.38}$$

In this equation, T_b is the normal boiling point (i. e., the boiling point at 1.013×10^5 Pa). Q has the dimensionality of $[\mathrm{kg}^{1/2}\mathrm{m}/(\mathrm{s\,K})]^{2/3}$, however its numerical value is adjusted to yield the surface tension in mN/m. Equation (3.37) and (3.38) may predict surface tension to within a few percent.

3.3 Contact Angle

3.3.1 The Equilibrium Contact Angle

This section presents the various definitions of equilibrium contact angles, their measurement and interpretation. It starts with the contact angle on an ideal solid surface, its calculation, and the assessment of the solid surface tension from the value of the ideal contact angle. Then, the complexity of contact angles on real surfaces, which are rough and chemically heterogeneous, is explained. The phenomenon of hysteresis and the concepts of the advancing, receding, and most stable contact angles are presented and discussed. The conditions for meaningful measurement of contact angles are explained, and methods for their interpretation are presented.

The Ideal Contact Angle

The Young Equation. Figure 3.23 shows a typical wetting system consisting of a drop on a solid surface. This system contains three interfaces, therefore is characterized by three interfacial tensions: liquid–fluid σ_{lf}, solid–liquid σ_{sl}, and solid–fluid σ_{sf} (out of these, only σ_{lf} is directly measurable). The contact angle θ is defined as the angle between the tangent to the liquid-fluid interface and the tangent to the solid interface at the contact line between the three phases. By convention, the contact angle is measured on the liquid side (rather than on the fluid side). In many practical situations, the fluid is a gas.

The relationship between the contact angle and the interfacial tensions in the system is based on the pioneering publication by Young in 1805:

$$\cos\theta_Y = \frac{\sigma_{sf} - \sigma_{sl}}{\sigma_{lf}} . \tag{3.39}$$

In this equation, the subscript Y indicates the contact angle predicted by the Young equation. This equation was developed for the case of an ideal solid surface, which is defined as smooth, rigid, chemically homogeneous, insoluble and non-reactive. Therefore, this contact angle is referred to as the *ideal contact angle*. It is important to emphasize that this relationship depends only on the chemical nature of the three phases, and is independent of gravity. The latter may affect the shape of the drop, but not in the close proximity of the contact line, thus not its contact angle. The Young contact angle represents the state of the drop, which has the minimal Gibbs energy. It is important to note that the Gibbs energy versus contact angle curve for an ideal surface has only a single minimum at θ_Y. In other words, an ideal solid surface is characterized by a single value of the contact angle.

In principle, the three interfacial tensions may be influenced by each other at the contact line. This is

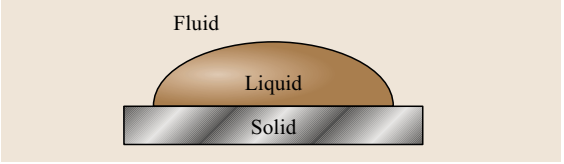

Fig. 3.23 A typical wetting system

due to the effect that one phase may have on the interaction between the other two phases. For example, the molecules of the solid may interfere with the interaction between the liquid and the fluid, thus affecting the value of the liquid-fluid interfacial tension very close to the contact line. This possibility was recognized by Gibbs, who suggested that this three-phase mutual interaction be accounted for by a *line tension*. The value of line tension has been a controversial issue for many years, however it is clear now that it may affect the contact angle of drops only when they are very small (much less than 1 micron). Therefore, line tension will not be referred to any more in the present discussion.

In order to predict the equilibrium contact angle, using (3.39), one needs to know all three interfacial tensions. However, σ_{sl} and σ_{sf} cannot be directly measured. Thus, the best that can be done to reduce the number of unknowns is to use the correlations between interfacial tensions and surface tensions that were introduced in Sect. 3.2. Since in most applications and, especially, in most measurements the fluid is a gas, σ_f is practically zero. Therefore, the solid–fluid interfacial tension σ_{sf} is actually the surface tension of a solid, σ_s. For simplicity and clarity of presentation, it is assumed throughout this chapter that the fluid is a gas.

Under this assumption, introducing, for example, (3.14) and (3.15) from Sect. 3.2 into (3.39), leads to

$$\cos\theta_Y = -1 + 2\phi\sqrt{\frac{\sigma_s}{\sigma_l}}\,. \tag{3.40}$$

It should be remembered, however, that σ_s, the surface tension of the clean solid, is also not directly measurable. Therefore, an equation such as (3.40) can be used in either of two ways (assuming that the value of ϕ is known):

1. to calculate the θ_Y, using σ_s as a free parameter;
2. to assess σ_s based on measurements of θ_Y.

A few numerical examples that illustrate the predictions of θ_Y by this equation are summarized in Table 3.9, assuming, for simplicity, that $\phi = 1$. The issue of the value of ϕ will be discussed later in more detail.

Example 1 represents the case of a water drop on a typical nonpolar plastic surface. The contact angle is relatively high, in agreement with typical data for water on polyethylene, for example. Example 2 represents a nonpolar liquid, such as octane, on a nonpolar plastic such as polyethylene. This case is characterized by a zero contact angle, and is usually termed *complete wetting*. Equation (3.40) shows that complete wetting always results when the surface tension of the liquid is approximately equal to that of the solid (depending on the exact value of ϕ). Equation (3.40) shows that the contact angle is higher than zero when the surface tension of the liquid is approximately higher than that of the solid, as demonstrated in the previous example 1. This case is termed *partial wetting*.

Table 3.9 Numerical predictions of (3.40) for various cases (assuming $\phi = 1$)

Example	σ_l [mN/m]	σ_s [mN/m]	$\cos\theta_Y$	θ_Y [°]
1	73	22	0.098	84.4
2	22	22	1	0
3	73	400	3.68	0

Example 3 demonstrates the case of a liquid spreading on a solid, whose surface tension is much higher than that of the liquid. For example, water spreading on a very clean metal surface. The interesting point is that the value of $\cos\theta_Y$ calculated from (3.40) appears to be higher than 1. This mathematical impossibility has a very simple physical explanation, as follows. Equation (3.39) or its derivatives (3.40) predict where the local minimum in energy should be, within the physically possible range of contact angles, which is 0−180°. However, whenever the value of $\cos\theta_Y$ is supposed by this equation to be higher than 1, it means that such a local minimum does not exist. Rather, the minimal energy occurs at the border of the contact angle range, $\theta_Y = 0°$. Similarly, if $\cos\theta_Y$ appears to be lower than (−1), the minimum in energy occurs at the other border, at $\theta_Y = 180°$.

It should also be noted that a clean solid surface, when exposed to air, may adsorb components from the air, so its *effective* surface tension may be lower than that of the clean solid. In some cases, the solid may adsorb the vapor of the liquid to such an extent that its surface tension is much lowered. Systems for which complete wetting is expected to occur (based on the surface tension of the clean solid), but actually are characterized by partial wetting (because of the adsorption of vapor), were termed *autophobic* by Zisman and his collaborators.

Assessing the Surface Tension of a Solid from the Ideal Contact Angle. Equation (3.40), or a similar equation, would have enabled the calculation of the surface tension of a solid, had the value of ϕ been known. However, ϕ

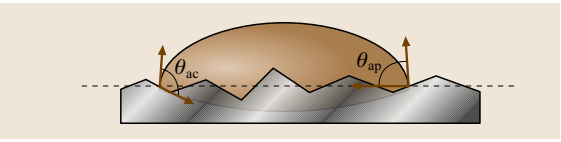

Fig. 3.24 The actual and the apparent contact angle on a rough surface

itself depends on the surface tension of the solid and on that of the liquid, as demonstrated, for example, by (3.19) in Sect. 3.2. When this equation is introduced into (3.40), one gets

$$(1+\cos\theta_Y)\sigma_l = 2\left(\sqrt{\sigma_s^d\sigma_l^d}+\sqrt{\sigma_s^d\sigma_l^d}\right) . \quad (3.41)$$

Assuming that the surface tension of the liquid and its components are known, this equation involves two unknowns: σ_s^d and σ_s^p. In order to solve for both unknowns, another contact angle measurement needs to be made with a different liquid on the same solid. Then, a system of two equations enables the calculation of the two unknowns:

$$(1+\cos\theta_{Y1})\sigma_{l1} = 2\left(\sqrt{\sigma_s^d\sigma_{l1}^d}+\sqrt{\sigma_s^d\sigma_{l1}^d}\right) . \quad (3.42)$$

$$(1+\cos\theta_{Y2})\sigma_{l2} = 2\left(\sqrt{\sigma_s^d\sigma_{l2}^d}+\sqrt{\sigma_s^d\sigma_{l2}^d}\right) . \quad (3.43)$$

In order to get meaningful results, it is very important to correctly choose the liquids for the contact angle measurements. It turns out that it is best if one of the liquids is nonpolar, and if the liquids are as dissimilar as possible.

Contact Angles on Real Surfaces

Actual and Apparent Contact Angles. The previous section outlined the procedures for calculating either the contact angle on an ideal solid, or the surface tension of a solid from the measured ideal contact angle. However, in reality, solid surfaces are seldom ideal; they are usually rough and chemically heterogeneous to some extent. In these cases, there is a need to distinguish between actual and apparent contact angles. Figure 3.24 demonstrates these definitions for a rough surface. The actual contact angle is the angle between the tangent to the liquid-fluid interface and the actual, local surface of the solid. The apparent contact angle is the angle between the tangent to the liquid-fluid interface and the line that represents the nominal solid surface, as seen macroscopically.

Figure 3.24 clearly demonstrates that the difference between the two angles may be very large. It turns out, that the actual contact angle equals the Young contact angle, if line tension is negligible. So, the actual contact angle is the one needed for the assessment of surface tension of solid surfaces, or as a boundary condition for theoretical calculations. However, a method to routinely measure the actual contact angle has not been developed yet. The contact angle that is currently amenable to measurement is the apparent one. Therefore, the main problem that needs to be solved is the correlation between the measurable, apparent contact angle and the ideal one.

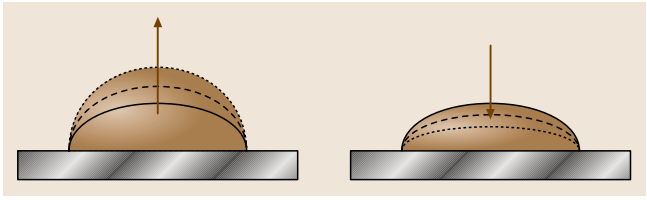

Fig. 3.25a,b Contact angle hysteresis: **(a)** increasing the drop volume increases the apparent contact angle up to the advancing contact angle; **(b)** decreasing the drop volume decreases the apparent contact angle down to the receding contact angle

Contact Angle Hysteresis. When apparent contact angles are measured on real surfaces, which may be rough or chemically heterogeneous or both, it becomes clear that there exists a range of practically stable, apparent contact angles. This is in contrast to the prediction by the Young equation of a single contact angle on an ideal surface. Experimentally, when the drop volume is increased, the contact line appears to be pinned, while the contact angle increases (Fig. 3.25a). The apparent contact angle eventually reaches a maximum value, which is termed the *advancing contact angle*. If the drop volume is further increased, the contact line advances. Therefore, the motion of the contact line is sometimes described as a *stick-slip* motion. Similar phenomena occur when the drop volume is decreased (Fig. 3.25b): the contact line appears to be pinned, while the contact angle decreases until it reaches a minimal value called the receding contact angle; further reduction in the drop volume causes the contact line to recede. The difference between the advancing and receding contact angles, which is termed the hysteresis range, may be very large. Thus, contact angle hysteresis is a major problem in the interpretation of contact angles and the assessment of the surface tension of a solid.

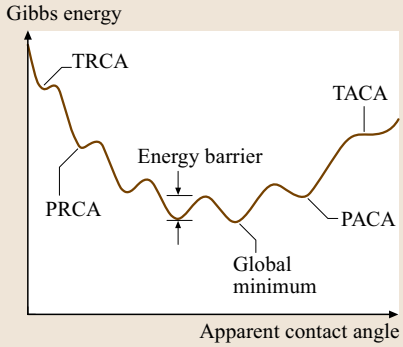

Fig. 3.26 A schematic of the Gibbs energy curve for a real surface with the following features: the global minimum, the theoretical advancing contact angle (TACA), a practical advancing contact angle (PACA), the theoretical receding contact angle (TRCA), a practical receding contact angle (PRCA), a potential barrier

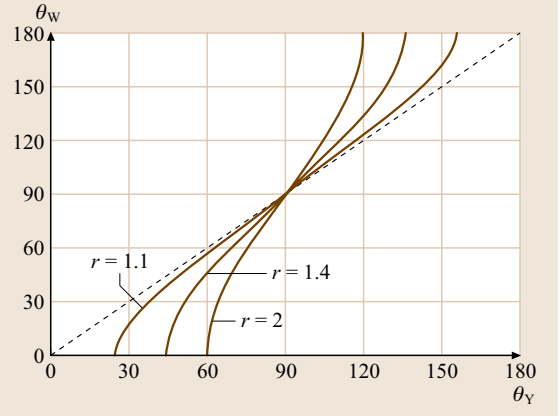

Fig. 3.27 The Wenzel versus Young contact angles for various roughness ratios. The *dashed line* corresponds to an ideal smooth surface with $r = 1$

In contrast to the Gibbs energy curve for a drop on an ideal solid surface, the energy curve for a real surface is characterized by multiple minima points, as demonstrated schematically in Fig. 3.26. Thus, many metastable apparent contact angles exist. In principle, the system tends to get to the most stable state, which is defined by the global minimum (Fig. 3.26). However, in-between the local minima in the Gibbs energy, local maxima exist. Therefore, in order to move from one local minimum to the next, the drop has to overcome an energy barrier (defined as the energy difference between a local minimum and an adjacent local maximum, Fig. 3.26). It is important to note that the energy barrier increases as the drop gets nearer to the global minimum.

Based on this theoretical picture, it is clear that the theoretical advancing contact angle is the highest angle for which there is a local energy minimum (Fig. 3.26). Similarly, the theoretical receding contact angle is the lowest angle for which there exists a local energy minimum. In practice, the system is always subject to some energy input from the environment, for example, via vibrations caused by the drop impact, or by the environment of the system. This energy input may enable overcoming energy barriers up to a certain level. Therefore, the advancing contact angle in practice is somewhat lower than the theoretical advancing contact angle (Fig. 3.26). Likewise, the practical receding contact angle is higher than the theoretical one.

The advancing and receding contact angles are measurable quantities. To some extent, they depend on the drop volume, so they should be measured for sufficiently large drops. An experimental indication for the drop being sufficiently large is minimal *stick-slip* behavior of the contact line. In other words, as the drop volume is increased or decreased, the drop retains the contact angle at its advancing or receding value, respectively, without featuring *stick-slip*. However, the correlation between the advancing, receding and the Young contact angle is not known yet. In some cases, especially when only a comparative study is required, the advancing contact angle serves as a convenient, reproducible measure. More information can be obtained from the most stable contact angle (at the global minimum in the Gibbs energy), as described in the following.

The Most Stable Apparent Contact Angle on Rough Surfaces. When a drop spreads on a rough surface, the actual solid–liquid interfacial area is higher than the nominal (projected) interfacial area. This has to be accounted for when the minimum in the Gibbs energy of the system is sought after. The surface roughness is characterized for this purpose by the roughness ratio r which is the ratio between the actual and nominal surface area of the solid. Thus, for a smooth surface $r = 1$, and for a rough surface $r > 1$. In 1936, Wenzel developed the following equation for the apparent contact angle θ_W on a rough surface

$$\cos\theta_W = r\cos\theta_Y \,. \tag{3.44}$$

This equation has an interesting practical prediction. If $\theta_Y < 90°$ (good wettability of a smooth surface of the same chemistry), roughness enhances wetting, i. e. $\theta_W < \theta_Y$. If, however, $\theta_Y > 90°$, roughness diminishes wetting, namely $\theta_W > \theta_Y$. This is demonstrated in Fig. 3.27 for a few values of r.

It is important to recognize that the Wenzel equation is based on the assumption that the liquid completely penetrates into the roughness grooves (Fig. 3.28a). This wetting situation on rough surfaces is termed *homogeneous wetting*. Under some roughness conditions, especially when roughness is high, this may not be the case: air bubbles may be trapped in the roughness grooves, underneath the liquid (Fig. 3.28b). The latter situation is referred to as *heterogeneous wetting* on rough surfaces, and will be described in detail below.

It turns out, that the Wenzel equation is an approximation, which becomes better as the drop becomes larger in comparison with the scale of roughness. The question of how large the drop should be in order for the Wenzel equation to apply has not yet been fully answered. However, based on some simulations and preliminary experimental data, it seems that if the drop is larger than the roughness scale by two to three orders of magnitude, the Wenzel equation applies. This is reasonable from an experimental point of view, since typical roughness is of the order of magnitude of microns, while typical drops are of the order of magnitude of millimeters.

The Wenzel contact angle represents the most stable contact angle on a rough surface, namely the contact angle that is associated with the global minimum in the Gibbs energy of the system. The methods for measuring the Wenzel contact angle will be described below. Once its value is known, the Young contact angle can be calculated using (3.44), assuming that the roughness ratio is also known. From the Young contact angle, the surface tension of the solid can be calculated as described above for an ideal solid surface. For example, the measurements and calculations can be repeated for two different liquids, then the surface tension of the solid can be calculated from (3.42) and (3.43).

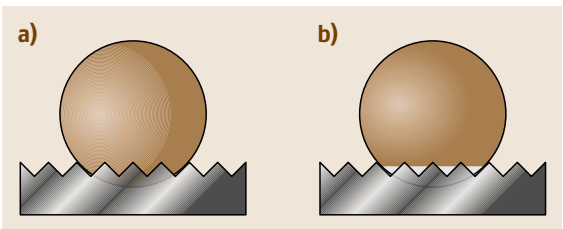

Fig. 3.28a,b Wetting on a rough surface: **(a)** homogeneous wetting – the liquid penetrates into the roughness grooves; **(b)** heterogeneous wetting – air bubbles are trapped in the roughness grooves, underneath the liquid

The Most Stable Apparent Contact Angle on Chemically Heterogeneous Surfaces. On a chemically heterogeneous solid surface, the surface tension varies from one spot to the other. Accordingly, the Young contact angle has a different, local value at each spot. Therefore, the characterization of chemically heterogeneous surfaces is more complex than that of rough surfaces. In general, the surface can be characterized by a properly averaged apparent contact angle.

The most stable apparent contact angle on a chemically heterogeneous surface θ_C is given by the Cassie equation, which was published in 1948 for the case of a surface with only two different chemistries

$$\cos\theta_C = x_1 \cos\theta_{Y1} + (1 - x_1)\cos\theta_{Y2} \,. \qquad (3.45)$$

In this equation, x is the area fraction characterized by a given chemistry, and the subscripts 1 and 2 indicate the two different surface chemistries. This equation can be generalized to state that the cosine of the Cassie contact angle is the weighted average of the cosines of all the Young contact angles that characterize the surface. The weighted averaging is done according to the area fraction of each chemistry.

Like in the case of the Wenzel equation, the Cassie equation is also an approximation that becomes better when the drop size becomes larger with respect to the scale of chemical heterogeneity. According to preliminary simulations, a size ratio of two to three orders of magnitude seems to be sufficient.

The Most Stable Apparent Contact Angle in Heterogeneous Wetting on Rough Surfaces. As mentioned above, under some roughness conditions, air bubbles may be trapped in the roughness grooves, under the liquid (Fig. 3.28b). In this case, the solid surface may be considered chemically heterogeneous, and the Cassie equation (3.45) may be applied:

$$\cos\theta_{CB} = f r_f \cos\theta_Y - (1 - f) \,. \qquad (3.46)$$

This equation was developed by Cassie and Baxter (CB), considering air to be the second chemistry in (3.45). In (3.46), θ_{CB} is the CB apparent contact angle, f is the fraction of the projected area of the solid surface that is wet by the liquid, and r_f is the roughness ratio of the wet area. The fraction f in this equation plays the role of x_1 in (3.45), and the contact angle of the liquid

with air is considered to be 180°, since the shape of a sufficiently small drop in air is very close to spherical. When $f = 1$, $r_f = r$, and the CB equation turns into the Wenzel equation.

The transition from homogeneous wetting (Wenzel equation) to heterogeneous wetting (CB equation) was theoretically analyzed by *Marmur* [3.44]. It was found to be dependent not only on the roughness ratio, but also on the specific geometry, in terms of the second derivative of $(r_f f)$ with respect to f. It was also found that heterogeneous wetting on rough surfaces may lead to super-hydrophobicity, which is defined as a state of a very high contact angle ($\gtrapprox 160°$) and very low roll-off (slip) angle. The latter is the inclination angle at which a drop slips from or rolls-off a solid surface. It turns out that the wetted area, i. e. the solid-liquid contact area, is much smaller in heterogeneous than in homogeneous wetting, even when the apparent contact angles are the same. Thus, it may be assumed that the force that holds the liquid to the solid is much smaller in heterogeneous wetting, thus leading to smaller roll-off angles.

Contact Angle Measurement and Interpretation. The most common method of measuring contact angles is by taking a side-view picture of a drop and evaluating the contact angle from this picture. The evaluation can be made either by direct measurement of the angle (preferably averaging the angles at the two sides of the drop), or by fitting a curve to the drop profile and calculating the angle from this curve. The fitting of the curve may be done either by using a polynomial or by using the solution to the Young–Laplace equation [as given by (3.32–3.34) of Sect. 3.2]. For many practical cases, the drop is sufficiently large for gravity to distort its shape from being spherical. Thus, fitting the shape by a circular segment is usually not satisfactory.

This method is simple, straightforward, and amenable to automation. However, the main disadvantage of this method is the lack of testing for the symmetry of the drop. If the drop is not axially symmetric, the measurement of the contact angle is questionable. Therefore, it is essential also to take a top view of the drop. If this picture of the drop assures axisymmetry, then the calculations based on the side-view are meaningful. Alternatively, it is possible to take only a top-view of the drop, and use the maximum drop diameter, drop volume, and the surface tension of the liquid to calculate the contact angle from the Young–Laplace solution for the drop shape. The drop volume is obtained via its weight and density.

In terms of interpretation, two approaches may be taken:

1. the hysteresis approach, and
2. the most stable apparent contact angle (MSACA) approach.

In the hysteresis approach, one measures the advancing and receding contact angles, θ_a and θ_r, and tries to estimate from them either the most stable contact angle θ_{ms} or the Young contact angle. The measurement of the advancing contact angle is done by increasing the drop volume until the highest possible contact angle is reached. Similarly, the receding contact angle is measured by decreasing the drop volume until the lowest possible contact angle is reached. Three methods of interpretation have been suggested within this approach. *Decker* et al. [3.45] suggested taking an average of the contact angles themselves:

$$\theta_{ms} = \frac{(\theta_a + \theta_r)}{2} \,. \tag{3.47}$$

Andrieu et al. [3.46] proposed an average of the cosines

$$\cos\theta_{ms} = \frac{(\cos\theta_a + \cos\theta_r)}{2} \,. \tag{3.48}$$

The third method is applicable only to rough surfaces, and aims at elucidating the Young contact angle. *Kamusewitz* et al. [3.47] suggested the following steps:

1. measuring the advancing and receding contact angles for a series of surfaces of the same chemistry but varying degrees of roughness;
2. drawing the advancing and receding contact angles versus the hysteresis range $(\theta_a - \theta_r)$;
3. fitting the best straight lines for the two sets of data in step 2; and
4. getting the Young contact angle from the extrapolated values of these two lines to zero hysteresis range.

In the MSACA approach, one tries to directly measure the most stable contact angle. The basic underlying idea is that by properly vibrating the surface, the drop may overcome the energy barriers and get to its most stable state. The practical problem is how to identify this most stable state. It was theoretically proven that a sufficiently large drop must be axisymmetric on a horizontal, real surface. The opposite statement has not been proven, but a working hypothesis based on it may be applied: a drop becomes more axisymmetric as it is vibrated and

approaches the most stable state. Thus, the measurement procedure involves vibrating the surface while monitoring the symmetry of the drop by viewing it from above; once the drop becomes symmetric, its contact angle is measured as described above.

Unfortunately, none of the above approaches has been sufficiently studied and substantiated. Also, no standard surfaces for comparing and calibrating contact angle measurements seem to exist. However, careful performance of contact angle measurement according to the above description and explanation may yield useful information. In particular, it should be emphasized that the following two principles should be applied in all cases and methods:

1. the drop should be sufficiently large, at least two orders of magnitude larger than the scale of roughness or chemical heterogeneity; and
2. the drop should be axisymmetric at the time of measurement.

3.3.2 Dynamic Contact Angle

Here, the concept of the dynamic contact angle, its origin and significance are introduced and current theoretical interpretations are briefly surveyed. The general experimental techniques used in its measurement are then discussed in detail with particular reference to the method by which a liquid drop is applied to a flat solid surface and allowed to spread. Other methods are also outlined to illustrate some of the experimental problems and their solution.

Introduction

Significance of the Dynamic Contact Angle. Many industrial and material processing operations require a liquid to be spread onto a solid. Examples include coating, painting, printing, plant protection, gluing and lubrication. The liquid may be paint, ink, insecticide, adhesive or some other liquid, and may be Newtonian or rheologically complex. Similarly, the solid may have a surface that is smooth or rough, uniform or chemically heterogeneous. It may be shaped as a sheet or a fibre or have some more complicated shape, and it may be porous. Evidently the properties of the materials involved can vary widely.

Apart from the fundamental problem of whether a given solid is wetted by the liquid in question, which is discussed in Sect. 3.3.1, many of the practical applications require a precise knowledge of how the rate of wetting affects the process. In particular, it is often helpful to know just how fast a liquid will wet or can be made to wet a given area of the solid surface. Such information is useful in process optimisation. The underlying phenomena are also relevant to our understanding of many other processes such as oil recovery from porous rocks and ground-water flow.

The dynamic behaviour of a liquid front moving across a solid has been studied extensively over the past several decades. A variety of different configurations have been examined, but most studies have been restricted to one or more of the following:

- drops spreading on a flat substrate – relevant to inkjet printing, the spraying of liquids such as paint or insecticide, etc.;
- drops moving down an inclined plane – relevant to droplet runoff;
- liquid penetration into capillary tubes or between parallel plates – relevant to flow in porous media;
- solid substrates, such as plates, cylinders, flexible tapes or fibres being drawn into or out of liquids – useful for fundamental coating studies;
- more complex configurations such as those involved in industrial coating processes, e.g., curtain and roller coating.

In simple cases, the main parameters required to quantify the dynamics of wetting are the relative velocity at which the liquid moves across the solid, i. e., the contact-line velocity v, and the dynamic contact angle θ_D, i. e., the angle formed between the moving liquid interface and the solid surface. The dynamic contact angle is the key boundary condition for the wetting process. Significantly, the experimentally observed dynamic angle generally differs from the static contact angle θ_S and may refer to either an advancing (wetting) or a receding (dewetting) interface. Since solid surfaces are often rough or chemically heterogeneous, even equilibrium contact angles may not be single-valued, but will depend on whether the interface has been advanced or recessed a phenomenon known as contact angle hysteresis (Sect. 3.3.1). On such surfaces, contact lines tend to pin, and when they do eventually move they do so in an unsteady way. Such factors complicate both the measurement and the interpretation of the contact angle. This is especially true on surfaces that swell or reorganise in some way on contact with the liquid.

Origin of the Dynamic Contact Angle. In forced wetting or forced dewetting, the contact line is made to move by application of an external force. In such cases, a single functional relationship is expected between θ_D and

v for any given system under a given set of conditions. On changing the system or the experimental conditions (e.g., the flow rate in a coating experiment) the precise form of this relationship may change. Recent studies seem to suggest that the form of the relationship depends on the flow field in a fairly complex way [3.48, 49], so that θ_D may not be a material property of the system at any level. Nevertheless, it is generally observed that advancing angles increase while receding angles decrease with increasing rates of steady contact-line displacement. In other words the contact angle depends on both speed and direction of displacement, i. e., it is velocity dependent. This is shown schematically in Fig. 3.29 for a system that also exhibits contact angle hysteresis. While anomalies have been observed [3.50], the relationship between θ_D and v is usually monotonic.

On the other hand, if we deposit a drop of liquid onto a solid it will tend to spread spontaneously under capillary forces alone (spontaneous wetting). Under these transient conditions, the instantaneous dynamic contact angle will relax, decreasing from 180° at the moment of contact towards its static value. At the same time, the contact-line velocity will decrease from its initial value to zero at equilibrium [3.51]. The reverse situation is observed if we forcibly spread a liquid on a surface that it wets only partially and then allow it to break up and retract into individual droplets (spontaneous dewetting). In this case, the contact angle will increase from its value on rupture towards its static value. Because of contact angle hysteresis, the final, static values may differ.

Since both forced and spontaneous wetting and dewetting are examples of moving contact lines, it should be possible to describe them in some equivalent way. Since the processes occur at a finite rate, possibly with associated changes in the shape of the liquid, but certainly with changes in the wetted area, the wetting processes must be dissipative. Indeed, the fact that the observed dynamic contact angle differs from its equilibrium value is evidence of this. Several attempts have been made in the literature to explain the observed behaviour, however these boil down to essentially two approaches, which differ from each other mostly in their consideration of the effective dissipation channel.

One of these two approaches, commonly known as the hydrodynamic theory, emphasises the dissipation due to viscous flows within the slowly-moving wedge of liquid near the contact line [3.52–57]. Changes in the observed dynamic contact angle are then ascribed to viscous bending of the liquid interface in this mesoscopic region. The microscopic angle θ_m is usually assumed to retain its static value θ_S.

The other approach, which originates from the Frenkel/Eyring view of flow as a stress-modified molecular rate process, discards dissipation due to viscous flow and focuses instead on that occurring in the immediate vicinity of the moving contact line due to the process of attachment or detachment of fluid particles to or from the solid surface [3.50, 58, 59]. According to this view, the channel of dissipation is effectively the dynamic friction associated with the moving contact line [3.60], and the microscopic contact angle is velocity dependent and identical with the experimentally observed angle. This approach is usually termed the molecular-kinetic theory.

A full discussion of these theories is beyond the scope of this chapter, but it is helpful to outline the basic equations and give some examples of the magnitude of the relevant parameters. In its most simple form, the equation describing the change in the dynamic contact angle due to viscous bending may be written in terms of the capillary number $\mathrm{Ca} = (\mu v/\sigma)$ as

$$\theta_D^3 - \theta_S^3 = 9\mathrm{Ca}\ln\left(\frac{L}{L_m}\right), \quad \theta_D < 3\frac{\pi}{4}, \quad \theta_m = \theta_S, \tag{3.49}$$

where μ and σ are, respectively, the dynamic viscosity and surface tension of the liquid and L and L_m are, respectively, appropriately chosen macroscopic and microscopic length scales. Setting $L = 10\,\mu\mathrm{m}$, which is the approximate distance from the contact line at which the contact angle can be measured, and $L_m = 1\,\mathrm{nm}$, i. e., the order of molecular size, then $\ln(L/L_m)$ is estimated to

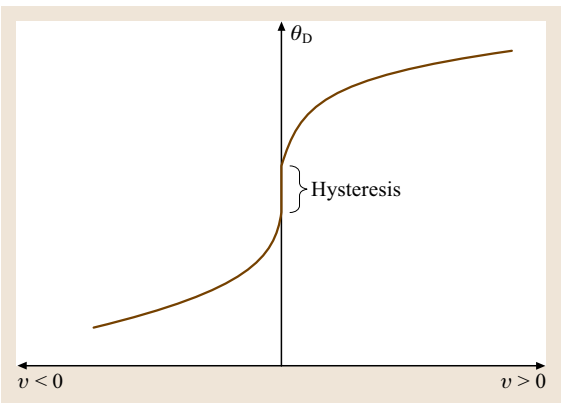

Fig. 3.29 Schematic representation of the velocity dependence of the contact angle, illustrating the behavior of the dynamic advancing and receding contact angles for a system that also exhibits contact angle hysteresis. If hysteresis is present, very low steady contact-line velocities may not be experimentally accessible

be of the order of 10. Experimental values vary widely, though values of about 10 have been found frequently for liquids that completely wet the solid. Much larger values have sometimes been reported for non-wetting liquids. These are usually thought to be non-physical, since they would appear to involve sub-molecular microscopic length scales.

For small drops and small angles (3.49) leads to simple scaling laws for the base radius R and the instantaneous contact angle as a function of time t:

$$R(t) \sim t^{1/10} , \tag{3.50}$$

$$\theta_D(t) \sim t^{3/10} . \tag{3.51}$$

These relationships have been widely confirmed for completely wetting liquids.

According to the contrasting viewpoint provided by the molecular-kinetic theory, the motion of the contact line is determined by the statistical dynamics of the molecules within its immediate vicinity. The key parameters are κ^0, the equilibrium frequency of the random molecular displacements occurring along the contact line, and λ the average distance of each displacement. In the simplest case, λ is supposed to be the distance between adsorption sites on the solid surface. The driving force for the wetting line to move in a given direction is taken to be the out-of-balance surface tension force that arises when wetting equilibrium is disturbed: $\sigma(\cos\theta_S - \cos\theta_D)$. The resulting equation for the contact-line velocity is then

$$v = 2\kappa^0\lambda \sinh\left[\sigma(\cos\theta_S - \cos\theta_D)\frac{\lambda^2}{2k_BT}\right] , \tag{3.52}$$

where k_B is the Boltzmann constant and T the temperature. If the argument of the sinh function is small, (3.52) reduces to its linear form

$$\begin{aligned} v &= \kappa^0\lambda^3\sigma\frac{(\cos\theta_S - \cos\theta_D)}{k_BT} \\ &= \frac{1}{\zeta}\sigma(\cos\theta_S - \cos\theta_D) , \end{aligned} \tag{3.53}$$

where $\zeta = k_BT/\kappa^0\lambda^3$ is the coefficient of contact-line friction. This has the same units as dynamic viscosity. While the experimentally determined values of λ are usually of molecular dimensions, those of κ^0 can vary widely. Some examples are listed in Table 3.10. Consistent with theory, experimental values of ζ are always larger than the viscosity of the liquid (Table 3.10), and appear to increase both with viscosity and the strength of solid–liquid interactions.

Crucially, (3.52) and (3.53) predict scaling laws that differ from those predicted by (3.49):

$$R(t) \sim t^{1/7} , \tag{3.54}$$

$$\theta_D(t) \sim t^{3/7} . \tag{3.55}$$

Comparison with experiment therefore offers the opportunity of assessing which mode of dissipation may be occurring.

Despite their fundamentally different bases, both models have been shown to work fairly well for experimental liquid/solid systems, though problems remain. As it seems likely that both types of dissipation occur simultaneously, combined theories have been suggested [3.61–63]. For example in the case of a spreading drop, it has been predicted and apparently confirmed that the wetting-line friction regime precedes the viscous regime, which becomes dominant only as the contact angle becomes small [3.63, 64]. However, it is also important to mention the continuum hydrodynamics approach adopted by *Shikhmurzaev* [3.63]. This accommodates dissipation through standard hydrodynamic channels, but also exploits non-equilibrium thermodynamics to describe dissipation due to the solid/liquid interfacial formation process. One consequence of this approach is that the microscopic dynamic contact angle is coupled directly to the flow. Analytical expressions can be obtained for certain simplifying conditions, such as small capillary number, which are very effective in describing the experimental results found in the literature [3.65, 66].

The reason for briefly discussing these theoretical interpretations in a chapter devoted to experimental methods is two-fold. First, experimental results, unless used in a purely descriptive way, will have to be interpreted in terms of a model of some sort, though it is important not to prejudge the observations in terms of any given model. Secondly, it is wise to ensure that sufficient ancillary measurements are made to enable the results to be interpreted as fully as possible. For example, in specifying the liquid, it will usually be essential to have sufficiently accurate measurements of its viscosity (assuming this to be Newtonian, which is not always the case with industrially interesting liquids), surface tension and density (Sects. 3.1,3.2 and 3.4). Similarly, if comparisons are to be made between different flows, then it is important to determine parameters such as geometry and flow rate that properly characterize them. It may also be desirable to determine other factors such as the roughness of the solid surface. In this latter case, techniques such as profilometry, optical scanning mi-

Table 3.10 Examples of the values of parameters obtained by applying the molecular-kinetic theory to experimental data for various systems

System	μ [Pa s]	σ [mN/m]	θ_S [°]	λ (nm)	κ^0 [s^{-1}]	ζ [Pa s]
Water on PET [3.50]	0.001	72.4	82	0.36	8.6×10^9	0.01
16% glycerol in water on PET [3.50]	0.0015	69.7	72.5	0.46	3.6×10^9	0.012
86% glycerol in water on PET [3.50]	0.104	65.8	65	0.46	3.5×10^7	1.2
Di-*n*-butyl phthalate on PET [3.51,67]	0.196	34.3	< 7	1.8	1.1×10^5	6.4
Silicone oil on glass [3.50,68]	0.958	21.3	0	0.79	2.3×10^5	35.9
Silicone oil on glass [3.50,68]	98.8	21.7	0	0.79	2.3×10^3	3580

croscopy or, ultimately, atomic force microscopy may be applied.

Useful reviews concerning the dynamic contact angle and its interpretation can be found in the references cited above, especially [3.50,56,57,65]. For further reading, *Dussan* [3.69] provides a perceptive survey of the older literature, covering both theoretical and experimental aspects, while *Blake* and *Rushak* [3.70] set the dynamic contact angle in the context of modern coating processes.

Generic Methods

General Principles and Techniques. The general principles of dynamic contact angle measurement can be illustrated by describing the experimental techniques used to study a liquid drop spreading on a flat solid substrate. Obviously, these techniques can equally be applied to the measurement of static contact angles, as discussed in Sect. 3.3.1.

The drops are usually supplied via a microsyringe, the needle of which is ground at right angles. Drop volumes of the order of 1 µl or larger are typical. If appropriate to the problem under investigation, useful measurements can be made with much smaller droplets, e.g., 100 pl [3.71], but these require special deposition techniques. For convenience, the solid substrate should be mounted on a three-axis translational stage. Both microsyringe and translation stage can be motorized and computer controlled for repeat measurements. If required, the stage can be thermostatically heated and the whole system enclosed in an environmental chamber. Sufficient time must be allowed to equilibrate the system before commencing measurements.

The profiles of the drops are easily captured using a high-resolution black and white digital video camera equipped with a suitable macro lens or long working distance microscope having the necessary magnification. The video camera is connected to a PC, which enables the images to be processed in real time and/or stored for subsequent processing. To get clear, sharp profiles, proper illumination is crucial. Diffuse uniform back-lighting seems to be best for routine video imaging of droplet profiles, whereas a collimated light source (Koehler illumination) is better for very precise measurements in the vicinity of the wetting line or for very small drops. Some means of adjusting the intensity of the light is desirable, such as a proprietary control unit or neutral density filters.

Existing set-ups are capable of capturing objects with sizes ranging from a fraction of a millimetre (such as ink-jet droplets) to about one centimetre. A typical image of a sessile drop is shown in Fig. 3.30. A computer program using suitable edge-detection algorithms and contour fitting then finds the contact angles from the profile. Typically, a full profile is discretised into about 1500 points and the best parameters are calculated in a few seconds.

Deposited drops are not always axially symmetric, so it is helpful to divide the data set for each drop into four parts, specifically the left and right side of the drop and left and right side of its reflection in the substrate. For each part we can calculate the best parameters to fit the Young–Laplace equation (Sect. 3.2) for the capillary pressure drop across a curved interface. For a drop in a gravitational field in the z direction, the equation may be written as

$$\Delta\rho g z = \sigma\left[\frac{z''}{\left(1+z'^2\right)^{1/2}} + \frac{z'}{x\left(1+z'^2\right)^{1/2}}\right], \tag{3.56}$$

where $z' = \mathrm{d}z/\mathrm{d}x$, $z'' = \mathrm{d}^2z/\mathrm{d}x^2$, $\Delta\rho$ is the difference in density between the drop and the air and g the acceleration due to gravity. In doing this, we are assuming implicitly that the Young–Laplace equation can describe the shape of non-equilibrium interfaces. This is true if the capillary number based on the contact-line velocity is small, but even if this approximation is not strictly valid, the procedure will usually give an acceptable fit

to the experimental data. See [3.72] for an experimental investigation of the influence of viscous deformation on the shape of a liquid meniscus during the immersion of a vertical cylinder into a pool of liquid.

To calculate the contact angle between the liquid and the substrate, it is vital to locate the exact position of the contact line. To find this with high precision, one should expand or contract the calculated profiles of the drop and its reflection, until they intersect each other symmetrically about the plane of the solid. The angle of the resulting curve with this plane is then easily calculated. Using this procedure, it is possible to calculate the left and right contact angles independently. Any small difference between the two angles is an indication of the precision of the measurement and/or the non-uniformity of the solid surface. This technique also allows one to edit the profile to eliminate anomalies. For example, it allows one to leave the needle used to deposit the liquid inside the drop while capturing the image; any deformation associated with the needle is edited out afterwards. To minimise the effect on the precision of the measurements, the diameter of the needle should be less then 1/3 of the diameter of the drop. With the needle inside the drop, it is possible to measure both advancing and receding contact angles by adding or subtracting liquid.

Another possibility is to set the focus on one contact region, rather than the whole drop. In this way, a higher magnification can be used, but information about the rest of the profile is lost. The profile of the part of the drop near the solid and its reflection can be fitted by a simple curve, such as a circular arc or a straight line. Both kinds of fits are satisfactory, and result in systematic differences in the contact angle of no more than 2°. One of the main advantages of this approach is that it can be fully automated and applied to geometries other than a spreading drop. It is particularly useful in forced wetting experiments, such as those involving plunging tapes (Fig. 3.31a) [3.66, 73] or coating processes (Fig. 3.31b) [3.49, 74, 75] where the wetting line remains more-or-less stationary in the frame of observation. With plunging tapes, a clearer image of the meniscus is obtained if the tape is curved slightly across its width at the point of entry into the liquid, creating what amounts to a plunging cylinder. By viewing along a tangent to the curve the contact angle can be measured at a single point rather than across the whole width of the tape [3.66]. Further details concerning dynamic contact angle measurements in these more specialised situations can be obtained from the references given.

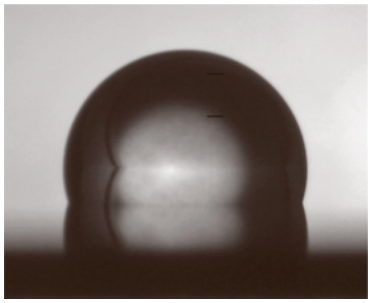

Fig. 3.30 Image of the profile of a sessile drop of water on an oxidized silicon wafer chemically grafted with octadecyltrichlorosilane. Here the equilibrium contact angle is 105°

A standard video system captures 50 or 60 images per second, giving one image every 20 or 17 ms. However, high-speed cameras and recording systems with rates up to at least 1000 frames per second are readily available and are especially helpful in determining the contact angle in the early stages of spreading [3.71]. Even higher effective framing rates are attainable using stroboscopic methods and suitable triggering. With such techniques, a temporal resolution of 1 μs is relatively straightforward and is especially helpful in studying rapidly evolving phenomena such as droplet deposition. However, high-speed imaging necessitates very high data transfer rates and may pose storage problems. Applied to dynamic contact angle measurements, they are more suitable if used with circular-arc or straight-line fitting techniques rather than those involving fitting entire profiles.

Computer programs for controlling drop deposition, image-capture and data processing can be custom written using standard methods. For image processing public domain packages such as NIH image are freely available [3.76]. Alternatively, all aspects of control and contact angle measurement can be implemented using high-level commercial software such as LabView or other scientific programming language, paying special attention to the quality of the edge detection algorithm. Commercial contact angle apparatus incorporating many of the features described above can also be purchased, but care should be taken to ensure they fully meet experimental requirements.

In practice, the solid/liquid systems that can be analyzed using the techniques described above have to meet the following requirements. First, the time of spreading should fall within the time frame of the equipment. This means that the contact angle should not change too much between consecutive images. Drop spreading exhibits the highest velocities just af-

ter deposition. Secondly, the first angle that can be measured clearly has to differ significantly from the equilibrium angle. If this is not the case, the dynamic behaviour is too fast to be captured. For example in inkjet printing most of the spreading process is over within 0.1 s [3.71]. Thirdly, the contact angles have to be larger then about 5°. Below this value, the angle cannot be distinguished from zero. Special techniques are required such as the optical interference methods used to study thin liquid films. It follows also that angles greater than about 175° cannot be distinguished from 180°.

Example. Figure 3.32 shows the results obtained on depositing 0.5 to 1 µl droplets of di-*n*-butyl phthalate (DBP) onto poly(ethyleneterephthalate) (PET) [3.51]. The dynamic contact angle is plotted as a function of time after deposition. The density, dynamic viscosity and the surface tension of the DBP (Fisons, SLR grade, 99%) were respectively 1.04 g cm^{-3}, 19.6 m Pa s and 34.3 mN/m at the temperature of the experiment (21 °C). The PET was provided by Kodak Ltd. as a flexible and transparent 35 mm tape. When fixed to a rigid solid (in this case a glass slide), the surface is flat. The PET has a low roughness and shows a homogeneous, moderately low energy surface giving small contact angle hysteresis with organic liquids. The DBP droplets eventually spread to achieve a static advancing contact angle of less than 7°.

Repeatability of the experimental curves is excellent except for the first few data. If we adjust the starting time, the curves collapse perfectly. This means that the experiment is fully reproducible, except for the initial condition. This is not a problem, as all the equations can be expressed in terms of velocity relative to the initial time. The standard deviation of the data indicates the error on the individual measurements to be to be less than 1°.

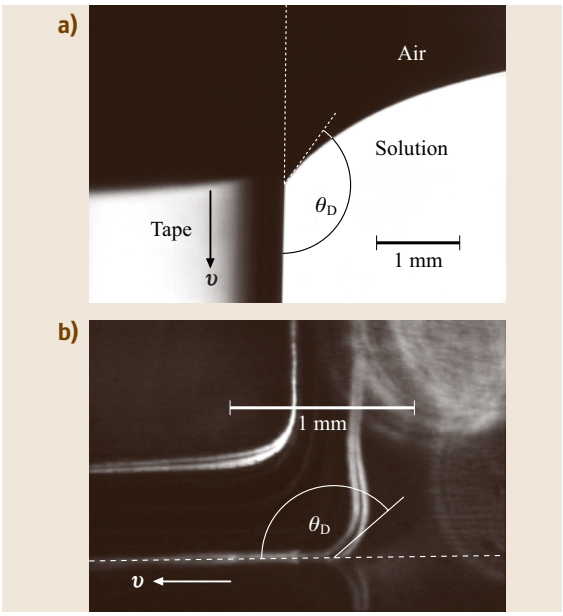

Fig. 3.31 **(a)** Image of a polyester tape entering a pool of aqueous glycerol at 0.05 m/s [3.70]. The tape is bent into a slight curve (to the left). By viewing along a tangent to the curve, the contact angle is measured at a single point rather than across the whole width of the tape. The air appears dark due to internal reflection. The dynamic contact angle through the liquid was determined to be (143±2)°. **(b)** Flow visualization of curtain coating showing the liquid impinging onto the moving substrate and being coated to the left as a uniform layer [3.49]. The various interfaces are marked by light scattered from streams of hydrogen bubbles, which are reflected in the interfaces and therefore appear doubled. The contact angle through the liquid was determined to be (140±5)°

Data Analysis. Figure 3.33 shows advancing dynamic contact angle data for DBP on PET obtained using the plunging tape method [3.51, 67]. At the lowest experimental velocity, the contact angle is about 16°. The contact angle increases with increasing velocity. Air entrainment is seen when the contact angle is close to 180° ($v \approx 52$ cm/s). This kind of curve is typical of the steady-state wetting behaviour observed for Newtonian liquids [3.50]. In forced wetting experiments, such as this, one obtains the dynamic contact angle directly as a function of wetting velocity, allowing direct theoretical comparison by standard curve-fitting techniques.

On the other hand, with spreading drops, some analysis is required to obtain the data in this direct form or to compare the results with theory. Only then can the resulting parameters be related to the physical characteristics of the system. To do this, one can make use of the scaling laws given in Sect. 3.1.2, however a more thorough analysis is preferable. For a fixed set of flow conditions, all the equations describing the different theoretical models can be expressed in general terms as

$$v = \frac{\mathrm{d}R}{\mathrm{d}t} = f(\theta_D, \theta_S, \sigma, \mu \ldots P_1, P_2 \ldots) , \qquad (3.57)$$

where f is an independent or at most a weak function of the base radius R, and P_1, P_2, etc. stand for the theory-specific parameters of interest, e.g., L/L_m for

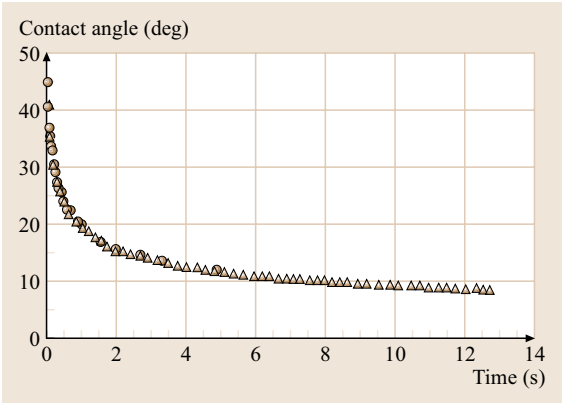

Fig. 3.32 Dynamic contact angle as a function of time for droplets of DBP on PET. The plot shows two sets of data: (*circles*) spreading followed for 5 s, and (*triangles*) spreading followed for 13 s (after [3.51])

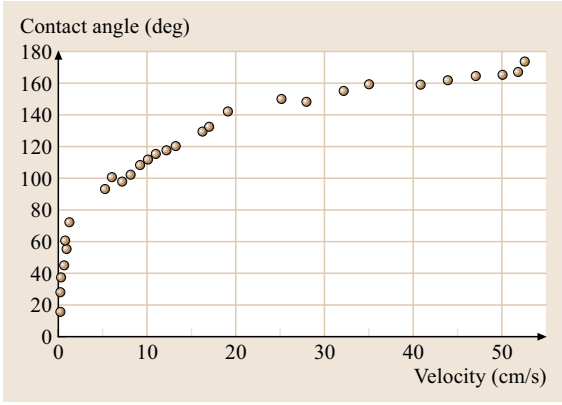

Fig. 3.33 Dynamic contact angle as a function of contact-line velocity for a PET tape plunging into a pool of DBP (after [3.51, 67])

the hydrodynamic theory, or either ζ or $\kappa^0\lambda$ and λ^2/k_BT for the molecular-kinetic theory. In addition, we have the following relation between R and the instantaneous contact angle θ at any time t:

$$R = \left(\frac{3V}{\pi}\right)^{1/3} \frac{\sin\theta}{\left(2-3\cos\theta+\cos^3\theta\right)^{1/3}} \,. \qquad (3.58)$$

Here, it is assumed that the drop has the shape of a spherical cap (Bond number $\mathrm{Bo} = \Delta\rho g V^{2/3}/\sigma \ll 1$) and that the volume of the drop V is constant (the liquid has low volatility). Differentiating this equation yields

$$\frac{\mathrm{d}R}{\mathrm{d}t} = -\left(\frac{3V}{\pi}\right)^{1/3} \frac{(1-\cos\theta)^2}{\left(2-3\cos\theta+\cos^3\theta\right)^{4/3}} \frac{\mathrm{d}\theta}{\mathrm{d}t} \,. \qquad (3.59)$$

Finally, on combining (3.53) and (3.55), we obtain

$$\frac{\mathrm{d}\theta}{\mathrm{d}t} = -\left(\frac{\pi}{3V}\right)^{1/3} \frac{\left(2-3\cos\theta+\cos^3\theta\right)^{4/3}}{(1-\cos\theta)^2} \times f(\theta_D, \theta_S, \sigma, \mu, P_1, P_2 \ldots) \,. \qquad (3.60)$$

For a given system and initial conditions [e.g., $\theta(t=0) = 180°$], (3.60) may be solved by a Runge–Kutta algorithm [3.77] to find the curve $\theta(t)$. This theoretical curve is then compared with the experimental data. The total difference between both curves is minimized by adjusting the values of the parameters P_1, P_2, etc. using the downhill Simplex or Levenberg–Marquard methods [3.77]. Although this provides one with the best-fit parameters related to the experimental data, it does not give any indication of the expected errors on these values. Indeed, the calculated total difference is merely a measure of the quality of the fit, not its reproducibility. Furthermore, if the system is overdimensioned (e.g., if the parameters P_1, P_2, etc. are linearly dependent), the error on one or more parameters can diverge to infinity. To analyse the reproducibility of the fits, one may use the so-called bootstrap method [3.77]. With this powerful method, the original experimental data are used as the basis for a Monte Carlo simulation. From the original data set, 37% (i. e., $1/\mathrm{e}$) randomly chosen points are replaced by duplicates. The duplicate points are chosen according to a normal distribution function, with the original data as average and the expected error on each datum as the standard deviation. In this way, we replace the original data set with a new one, for which the corresponding parameters are then calculated using the method described above. Successive cycles result in a simulated set of values for each parameter. If enough cycles are used (> 100), these sets turn out to be normally distributed, providing one with the mean value and standard deviation for each parameter.

Other Techniques

In this chapter, the spreading drop technique has mainly been used to illustrate the generic methods of dynamic contact angle measurement. However, several others, such as those based on plunging tapes and coating visualisation, have been touched on, as they are very powerful methods of studying forced wetting and are therefore prominent in the current literature. For similar reasons, two other approaches also deserve specific mention.

The first involves calculating the dynamic contact angle from the force exerted on a plate or fibre as it immersed or withdrawn from a pool of liquid [3.78]. Suitable equipment is available commercially or can be adapted from a Wilhelmy plate surface tension apparatus (Sect. 3.2.5). Useful data can be obtained over a good range of low speeds (typically 10^{-4}–1 cm/s) provided the solid is available in a suitable form. The surface tension of the liquid must be determined in a separate experiment, e.g., using a completely wetted plate ($\theta_S = 0$).

The second approach is based on direct or indirect measurements of the dynamic contact angle during capillary flow. In principle, the angle can be determined indirectly from measured parameters (such as the meniscus velocity, distance of penetration, and/or the pressure drop down the tube) provided the flow can be accurately modelled [3.79]. But, this is difficult and the most reliable methods are usually based on direct microscopic observation of the moving meniscus [3.68, 80, 81]. Both the Wilhelmy plate and capillary flow methods can be used in steady-state or transient modes.

Finally, mention should be made of simulation methods in which the "experiments" are done using computational techniques such as molecular dynamics [3.60, 82]. Traditionally, these are not seen as experimental methods, however as computer power increases, such techniques will find increasing value where true physical experiments are currently very difficult or essentially impossible.

3.4 Viscosity

In this section viscometers for the measurement of the viscosity of Newtonian fluids over a wide range of thermodynamic states with high precision are described. In the first three types of viscometers considered, a solid body is forced to perform oscillations while immersed in the fluid. The characteristics of the oscillation are determined by the viscosity of the fluid. In the two other types of viscometers non-oscillatory flow is employed, in one case by the fluid flow through a capillary tube, and in the other a body of revolution falling under gravity through the fluid. Each has its merits, which are discussed.

The dynamic viscosity μ of a fluid is a measure of its tendency to dissipate energy when it is disturbed from equilibrium by a velocity field $\boldsymbol{v}$, which distorts the fluid at a rate $\dot{\varepsilon}_{ij}$ given by

$$\dot{\varepsilon}_{ij} = \frac{1}{2}\left(\frac{\partial v_i}{\partial x_j} + \frac{\partial v_j}{\partial x_i}\right) . \tag{3.61}$$

For viscous Newtonian fluids the viscosity is defined by the constitutive equation

$$\sigma_{ij} = -P\delta_{ij} + \mu\left(\frac{\partial v_i}{\partial x_j} + \frac{\partial v_j}{\partial x_i} - \frac{2}{3}\delta_{ij}\frac{\partial v_k}{\partial x_k}\right) . \tag{3.62}$$

In this equation, σ_{ij} are the instantaneous stresses P the pressure and δ_{ij} is the Kronecker symbol. In (3.62) it is assumed, as usually done, that the so-called volume (dilatational) viscosity is zero. The viscosity depends on the thermodynamic state of the fluid and is usually specified by the pairs of variables (T, P) or (T, ρ) for a pure fluid, to which must be added a composition dependence in the case of mixtures. While (3.62) incorporates the viscosity it does not immediately suggest means of measurement because it is impossible to measure local shear stresses. It should further be pointed out that the type of rheometers that will be discussed undoubtedly will have a shear rate that is not constant – thus, the measured moment of the shear stress is measured at one location but the rate of strain is not known at the same location. Thus, methods of measurement of the viscosity must be based on the determination of some integral effect of the stresses amenable to precise measurement in a known flow field. Inevitably, the imposition of a shear field generates small pressure differences and dissipation causes local temperature gradients, both of which change slightly the reference thermodynamic state to which a measurement is assigned, from the initial, unperturbed, equilibrium state. The reference state for the measurement will be obtained by averaging so that it is important that the system is disturbed as little as possible from equilibrium during measurement.

3.4.1 Oscillating-Body Viscometers

Oscillating-body viscometers consist of an axially symmetric body suspended from a torsion wire so that the body performs oscillations in the fluid about its axis of symmetry. The oscillator can be a disk (oscillating freely or between fixed plates), a sphere or a cup. The fluid usually surrounds the oscillator but, in the case of the sphere or the cup, it can be inside them. The suspension wire is elastic and the system is gently rotated to start a motion. The fluid exerts a viscous drag on the oscillator causing the angular frequency of the oscillation ω and the damping decrement Δ of the resulting simple harmonic

motion to be different from those in vacuum, ω_0 and Δ_0. The magnitude of the change depends on the viscosity and on the density of the fluid in addition to the physical characteristics of the oscillator. Measurements of ω, ω_0, Δ, and Δ_0 can give the viscosity of the fluid with very low uncertainty, if the density is known from an independent determination. The only measurements necessary in this technique are those of mass, length and time, in addition to those of the pressure and temperature, all of which can be made with a very high resolution. It is relatively straightforward to make the induced perturbation small, so that a near-equilibrium state is maintained.

The characteristic equation for the torsional motion of any oscillating body viscometer can be expressed [3.83, 84] as

$$(s+\Delta_0)^2+1+D(s)=0\,. \tag{3.63}$$

Here, $D(s)$ is the torque on the body, calculated from solutions for the fluid flow close to the oscillating body. It is therefore the torque $D(s)$ that is characteristic of the particular type of oscillating viscometer employed.

Apart from roots that are associated with the initial oscillatory behavior of the body, the roots associated with the long-time behavior [3.83, 84] can be written in the form

$$s=\pm(\mathrm{i}-\Delta)\theta \tag{3.64}$$

where i is the imaginary unit and

$$\theta=\frac{\tau_0}{\tau}\,. \tag{3.65}$$

Here, τ is the period of oscillation in the fluid and the subscript zero denotes the same quantity in vacuo. The motion associated with these roots, characterized by an angular displacement a of an axially symmetric body, is

$$a(t)=a_0\,\mathrm{e}^{-\Delta\theta\omega_0 t}\cos(\theta\omega_0 t)\,, \tag{3.66}$$

and this is the motion observed experimentally after an initial transient of about two periods.

Since the characteristic equation is complex, two equations, the real and imaginary parts are obtained from (3.63).

$$2\theta(\Delta_0-\theta\Delta)+\mathrm{Im}[D(s)]=0\,, \tag{3.67}$$

$$(\Delta_0-\theta\Delta)^2+1-\theta^2+\mathrm{Re}[D(s)]=0\,. \tag{3.68}$$

Equation (3.68), for the real part, can be used to determine viscosity but it requires a higher precision in measurement to achieve the same accuracy in the viscosity as can be attained using the imaginary part of the equation. Consequently (3.67) for the imaginary part has usually been preferred.

Before proceeding it is important to introduce a natural length scale that appears in oscillatory systems, namely the boundary-layer thickness defined as

$$\delta=\left(\frac{\mu}{\rho\omega_0}\right)^{1/2}\,. \tag{3.69}$$

This natural length scale is important in the selection of the dimensions of oscillating-body viscometers for particular purposes as the following three sections describing specific oscillating-disk, oscillating-cup and oscillating-sphere viscometers will show.

Oscillating-Disk Viscometers

One of the first very successful oscillating-disk viscometers was developed by *Kestin* and *Leidenfrost* [3.85] in 1959, to measure the viscosity of gases near room temperature, in the pressure range 0.1–60 MPa.

The basic design of such a viscometer, consists of a disk of radius R, thickness d and moment of inertia I, oscillating between two parallel fixed plates at distances b_1 and b_2 from its surfaces. Figure 3.34 shows a development by *Vogel* [3.86] of the early disk viscometers of Kestin and his collaborators. The configuration between two fixed plates has generally been preferred to a free disk, because the presence of the two parallel fixed plates tends to increase the viscous drag on the disk, and hence produce a decrement that is easier to measure with high accuracy. The plates also reduce the likelihood of influence from spurious free convective flows within the bulk of the fluid. The characteristic equation for the torque $D(s)$ for this configuration is [3.84]

$$D(s)=\frac{\pi R^4\mu s}{Ib\omega_0}\left[C_\mathrm{N}+\frac{s}{3}\beta_1\beta_2-\frac{s^2\beta}{90}(\beta_1^2+\beta_2^2)+\frac{s^3\beta}{945}\left(\beta_1^2+\beta_2^2\right)+\ldots\right]\,, \tag{3.70}$$

where

$$\beta_1=\frac{b_1}{\delta}\,,\qquad \beta_2=\frac{b_2}{\delta}\,, \tag{3.71}$$

$$\beta=\frac{b}{\delta}\,,\qquad b=\frac{2b_1b_2}{(b_1+b_2)}\,. \tag{3.72}$$

Equation (3.70) is valid if

$$b_1+b_2+d\ll R\quad\text{and}\quad b_1+b_2+d\ll\delta\,. \tag{3.73}$$

These conditions are readily met in the dilute and moderately dense gas states, so that (3.70) can be employed as the basis of the evaluation of the viscosity of the fluid. The quantity C_N is an instrumental constant that depends only on the linear dimensions of the oscillatory system. It is unity for a disk of infinite radius and zero thickness. Expressions can be found for it for real geometries in the literature [3.83, 84]. The instrument constant can thus be evaluated independently from the characteristics of the assembled instrument. This allows the formulation of the final working equation for the disk instrument to be written as

$$C_N = \left[\frac{2I}{\pi\rho b R^4}(\theta\Delta - \Delta_0) + f_1\theta\Delta\right]\beta^2 + f_2\theta^2(3\Delta^2 - 1)\beta^4 + f_3\theta\Delta(\Delta^2 - 1)\beta^6 , \tag{3.74}$$

where the coefficients f_1, f_2 and f_3 only depend on the distances d_1 and d_2 between the disk and the plates

$$f_1 = \frac{1}{6}\left[\left(\frac{d_1}{d_2}+1\right) + \left(\frac{d_2}{d_1}+1\right)\right] , \tag{3.75}$$

$$f_2 = \frac{1}{720}\left[\left(\frac{d_1}{d_2}+1\right)^3 + \left(\frac{d_2}{d_1}+1\right)^3\right] , \tag{3.76}$$

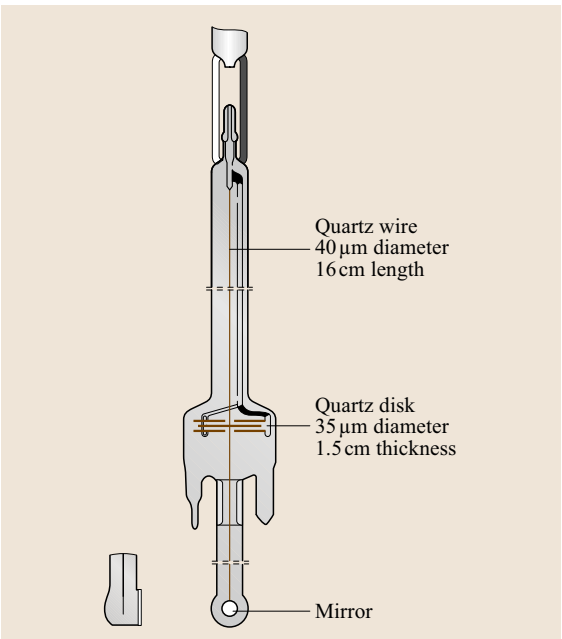

Fig. 3.34 Oscillating-disk quartz viscometer developed by *Vogel* (after [3.86])

$$f_3 = \frac{1}{7560}\left[\left(\frac{d_1}{d_2}+1\right)^5 + \left(\frac{d_2}{d_1}+1\right)^5\right] . \tag{3.77}$$

Equation (3.74) is a cubic equation in the square of β and the coefficients depend only on measurable quantities. The instrument can be used to obtain absolute measurements of the viscosity by solution for β for measured values of the frequency and damping of oscillations in the fluid and in vacuo, if C_N is known independently since from (3.69) and (3.72)

$$\mu = \frac{\omega_0\rho b^2}{\beta^2} . \tag{3.78}$$

It is essential for the accuracy of the instrument that a complete parallel alignment of the fixed plates and the disk, as well as their flatness, is achieved. The theoretical expression for C_N does not take into account the small amount of additional damping introduced by the stem and mirror attached to the disk in order to observe the oscillations and permit measurement of Δ, Δ_0, ω and ω_0. *Kestin* et al. [3.87] have shown that the value of C_N calculated from experiments in five different gases was within 0.1% of its theoretical value. The effect of the additional damping is therefore small but not always negligible.

Although (3.74) and (3.78) permit absolute measurements to be made, the conditions on their validity, namely the inequalities (3.73), make them inapplicable for very small boundary-layer thicknesses, such as occur in liquids and dense gases. In those cases an alternative formulation of the working equation has been developed in which an edge-correction factor is defined for an instrument. This edge-correction factor is a function only of the boundary-layer thickness so that it can be determined by calibration with fluids of known properties thus making relative measurements of the viscosity of other fluids, possible.

There has been a large series of oscillating-disk viscometers. It is worthwhile identifying some of the very successful instruments. As already mentioned, *Kestin* and *Leidenfrost* [3.85] developed the first instrument to measure the viscosity of gases near room temperature, in the pressure range 0.1–60 MPa with an uncertainty of about 0.1%. This instrument was employed over a wide range of conditions, including measurements near the critical point of carbon dioxide [3.88]. *Di Pippo* et al. [3.89] and *Kestin* et al. [3.90] designed a similar viscometer for high temperatures, up to 973 K, and low-pressure gases, with an uncertainty ranging from 0.1–0.3% at the highest temperatures. *Oltermann* [3.91]

also described an oscillating-disk viscometer for operation up to 673 K and 25 MPa in water near its critical point, with an estimated uncertainty of 1%. *Kestin* et al. [3.92] described an instrument to measure the viscosity of aqueous solutions of ionic salts at temperatures up to 573 K and pressures up to 35 MPa. It was operated in a relative mode with an estimated uncertainty of 0.3–0.5%. Finally, one of the most successful such instruments which is still in operation today is the quartz oscillating-disk viscometer (Fig. 3.34) designed by *Vogel* [3.86] for measurements on gases and vapors up to 650 K, with an uncertainty of 0.1–0.3%.

Oscillating-Cylinder Viscometers

The thick disk or cylinder configuration consists of a cylindrical body oscillating in an essentially infinite fluid. *Torklep* and *Oye* [3.93] have described an oscillating-cylinder viscometer designed for absolute measurements of low viscosity fluids up to temperatures of 1200 °C. The uncertainty quoted was 0.1% for water, where special efforts were made to achieve high accuracy, rising to 1% for routine measurements employing time-saving procedures.

Oscillating-Cup Viscometers

An oscillating-cup viscometer consists of an axially symmetric cylinder (cup) of inner radius R and height H, with the fluid contained inside. *Beckwith* and *Newell* [3.94] obtained the expression for $D(s)$ for the cases of a filled or partially filled cup. In the case of the filled cup, $D(s)$ is given by

$$D(s) = \frac{s^{3/2}}{I}\left(A\xi + B\frac{\xi^2}{s^{1/2}} + C\frac{\xi^3}{s} + D\frac{\xi^4}{s^{3/2}}\right) , \tag{3.79}$$

where I is the moment of inertia of the cup itself, and $\xi = \delta/R$. The coefficients in the above equation are

$$A = 4 + \frac{2R}{H} , \tag{3.80}$$

$$B = -6 - \frac{32R}{\pi H} , \tag{3.81}$$

$$C = \frac{3}{2} + \frac{18R}{H} , \tag{3.82}$$

$$D = 3.2 - \frac{16R}{\pi H} . \tag{3.83}$$

There are many successful oscillating-cup viscometers. *Grouvel* et al. [3.95] measured the viscosity of mercury in the range 20–260 °C with an uncertainty of 1.5%, while *Tippelskirch* et al. [3.96] employed an oscillating-cup viscometer to measure the viscosity of mercury from 470 to 1250 °C and to pressures up to 100 MPa. The uncertainty of this instrument was about 1% at the lower temperatures. *Abe* et al. [3.97] employed successfully such an instrument to measure the viscosity of molten salts in the temperature range 800–1200 °C. Finally, *Knapstad* et al. [3.98] measured the viscosity of many hydrocarbons up to 150 °C with an uncertainty of 0.5%.

Oscillating-Sphere Viscometers

In this type of viscometer, the fluid either fills a suspended, spherical shell or surrounds a suspended, solid sphere. Accurate expressions exist for the viscous torque in either case but the viscometer has not been as successful as have other types. This is partly because of the difficulty of manufacturing a sufficiently precise spherical shell, but also because the device offers little advantage over the simpler cylindrical viscometer. *Dumas* et al. [3.99] and *Brockner* et al. [3.100] employed oscillating-sphere viscometers to measure the viscosity of molten salts. However the uncertainty in the results achieved is higher than that obtained by oscillating-disk or oscillating-cup viscometers.

3.4.2 Vibrating Viscometers

The essential characteristic of the oscillatory viscometers discussed in the previous section was the observation of the effect of the viscosity of the fluid on the damping of the free, torsional motion of a rigid, solid body either immersed within it or surrounding it. In the case of the vibrating-wire viscometers, the oscillations involve periodic distortions of the solid body itself, which is in contact with the fluid whose viscosity is under investigation. The main advantages of vibrating viscometers are that the instruments are mechanically simpler than those of oscillatory bodies, and that the volume of fluid required for their use is much smaller, making operation at extremes of higher pressures and temperature easier.

Vibrating-Wire Viscometer

The vibrating-wire viscometer is a particularly simple form of vibrating viscometer, which has successfully been employed over a wide range of conditions. Indeed, it has played an important role in the investigation of the superfluid character of liquid helium [3.101].

A thin, circular-section wire of radius R, density ρ_s, subject to a tension, is constrained to be stationary at either end. It is surrounded by an infinite volume of the fluid of interest and performs oscillations transverse to its axis in a single plane containing the axis. If the os-

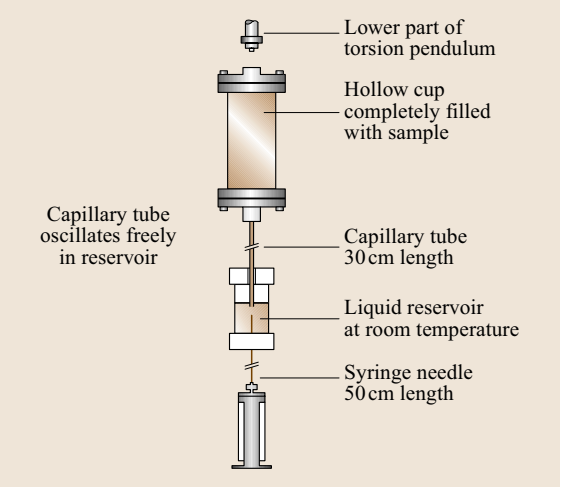

Fig. 3.35 Oscillating-cup viscometer developed by *Knapstad* et al. [3.98]

cillation is induced by an initial deflection at time $t = 0$ and subsequently allowed to decay, then the displacement of any point on the wire ξ ultimately conforms to a damped, simple harmonic motion [3.102]

$$\xi_a = A\,e^{-\Delta\omega t}\sin(\omega t + \phi)\,, \tag{3.84}$$

in which ω is the angular frequency and Δ the logarithmic decrement, and the subscript a indicates the asymptotic situation. At short times the displacement is affected by transients that cause a departure from (3.84)

$$\xi = F(t) + \xi_a(t)\,. \tag{3.85}$$

However, it has been shown [3.102] that the transient terms $F(t)$ decay rapidly compared with the decay time of the harmonic motion so that omission of the first few oscillations of an experiment is sufficient to eliminate them from consideration.

Provided that the design of the instrument is carried out to satisfy the constraints

$$\varepsilon \ll \Omega \ll \frac{1}{\varepsilon^2}\,, \tag{3.86}$$

where ε is the fractional amplitude of the motion, $\varepsilon = \xi_{max}/R$ and

$$\Omega = \frac{\rho\omega R^2}{\mu} \tag{3.87}$$

and

$$\omega\varepsilon\frac{R}{C} \ll 1\,, \tag{3.88}$$

where C is the sonic velocity in the fluid, then its motion should correspond to that of (3.84). The decrement and frequency of the motion are related to the viscosity μ, and density ρ, of the fluid by the equation [3.102]

$$\Delta = \frac{(\rho/\rho_w)k' + 2\Delta_0}{2\,[1 + (\rho/\rho_w)k]}\,, \tag{3.89}$$

where k and k' are given by

$$k = -1 + 2\mathrm{Im}(A)\,, \tag{3.90}$$

$$k' = 2\,\mathrm{Re}(A) + 2\Delta\mathrm{Im}(A)\,, \tag{3.91}$$

where

$$A = (\mathrm{i} - \Delta_0)\left(1 + \frac{2K_1(s)}{sK_0(s)}\right) \tag{3.92}$$

and

$$s = [(\mathrm{i} - \Delta)\Omega]^{1/2} \tag{3.93}$$

and K_0, K_1 are modified Bessel functions. Finally, Δ_0, denotes the logarithmic decrement of the wire's oscillations in vacuo which can be determined by direct measurement. Equation (3.87) and (3.89–3.93) can be used to calculate the viscosity of the fluid from the logarithmic decrement and the frequency of oscillation in the fluid and the logarithmic decrement in vacuo, provided that the density of the fluid is known.

Only one correction to the working equations given above is significant ($> 0.01\%$) and that arises from the fact that it is necessary to enclose the fluid within a solid wall. A correction for this effect has been derived [3.102, 103] and it is rather straightforward to allow for the presence of the boundary.

In the vibrating-wire viscometer [3.104, 105] shown in Fig. 3.36, the vibrations of the metallic wire are stimulated by a pulse of current through the wire in a permanent magnetic field. The observation of the motion of the wire uses measurements of the signal induced across the wire as it oscillates perpendicular to the same field. In the particular instrument shown, samarium–cobalt alloy permanent magnets provide the 1 T magnetic field required. The wire, at its lower end carries a central weight W. This weight is connected through a balancing mechanism to an outer stainless-steel weight. The balancing mechanism acts as a fulcrum for the two weights. The volumes of the two weights are chosen so that the net effect of changing the density of the surrounding liquid results in a negligible effect upon the tension in the wire and thus the frequency of oscillation. At the same time the difference in their masses produces a constant tension in the wire. The way of supporting the two weights

also produces a preferred plane of oscillation for the wire from among the degenerate set. The signal induced in the vibrating wire is observed with a bridge, and the out-of-balance signal, amplified by 30 000 times, is then interrogated with an analogue-to-digital (A/D) converter coupled to a computer. Representation of the decaying harmonic signal allows the determination of the frequency and decrement. This process is repeated in vacuo to provide all the information necessary to evaluate the viscosity using (3.87) and (3.89–3.93).

The uncertainty in the viscosity measurements made with such viscometers operated in an absolute manner is better than ±3%. Most of the uncertainty arises from those in the diameter of the vibrating wire and its density if they are determined independently. These two parameters can be determined with a greater precision through measurements on a fluid of known viscosity. When operated in the relative manner suggested by this calibration, the accuracy of viscosity measurements can be improved to one of ±0.5%, limited only by the uncertainty in the standard reference values for the viscosity. The precision in the viscosity measurements for liquids is about ±0.1%. For measurements in gases, the uncertainty is about ±1% when operated in an absolute way, and better than ±0.5% in a relative manner. Vibrating-wire viscometers have successfully been operated at Thessaloniki [3.104], London [3.105], Rostock [3.106] and Lisbon [3.107] over a wide range of conditions. A similar type of viscometer, but with the magnets outside the pressure vessel, was operated in Amsterdam [3.108]. The same types of viscometer have been operated in a continuous mode as well as the transient mode described here. In that case the resonant characteristics of the wire's vibrations have been measured with an impedance analyzer. These measurements have essentially the same accuracy as those performed in a transient mode but they have been used to make simultaneous measurements of density and viscosity on a single fluid, which has obvious advantages.

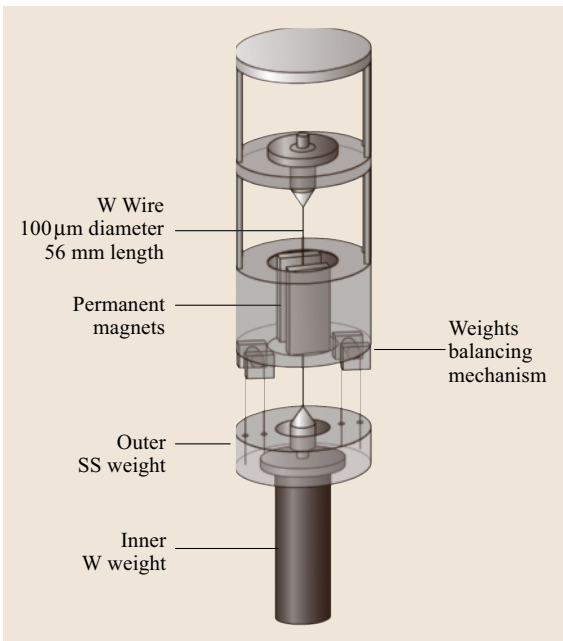

Fig. 3.36 Schematic diagram of a vibrating-wire viscometer for liquids developed by *Assael* et al. [3.104] and *Oliveira* [3.105]

3.4.3 Torsional-Crystal Viscometer

The torsional piezoelectric-crystal viscometer was introduced by *Mason* [3.109] in 1947. It has several important advantages over other viscometers. It can cover a very large viscosity range, from about $10–10^5$ µPa s, permitting measurements in a wide range of fluid states, ranging from low-pressure gases to liquids near freezing. The motion of the crystal is exceedingly small although of high frequency.

The basic principle of the technique is the following. If a cylinder of piezoelectric material is cut with its axis along the x-axis (electric), and a sinusoidal voltage is applied to four electrodes at its quadrants, the cylinder will vibrate with a nearly pure internal torsional motion. When the crystal is immersed in a fluid, a shear wave will be produced in the fluid and will be rapidly attenuated as it moves normal to the surface of the crystal. The viscous drag, exerted by the fluid on the surface of the crystal, changes the crystal's resonant frequency, its conductance at resonance, and its bandwidth at resonance from their values in vacuo. The equation, most frequently employed in recent work [3.110]

$$\mu\rho = \pi f_e \left(\frac{M}{S}\right)^2 \left(\frac{\Delta f_e}{f_e} - \frac{\Delta f_0}{f_0}\right)^2 , \qquad (3.94)$$

relates Δf_e, the crystal's bandwidth at resonance to the viscosity–density product of the fluid $\mu\rho$. Here, M, S and f_e are the mass, surface area, and resonant frequency of the crystal, respectively, while the subscript zero refers to the equivalent quantities in vacuo. In common with others this working equation neglects departures from pure torsion in the motion of the crystal and in the motion of the fluid.

Crystalline quartz is usually selected as the piezoelectric material because of its superior physical

properties. Crystal preparation includes obtaining the highest-quality starting material, orienting the cylinder axis along the x-axis (electric), grinding and polishing, locating the z-axis (optic) properly, sawing surface grooves at the midplane and parallel to the z-axis or plating electrodes on the crystal, measuring the crystal dimensions, and cleaning with appropriate solvents. Most torsional crystals have had electrodes plated directly on the surface of the crystal. However, several transducers [3.111, 112] have had a gap containing the test fluid between the surface of the crystal and the electrodes. An example of this type is shown in Fig. 3.37. This viscometer gives small repeatable bandwidths in vacuo. A typical crystal has a length of 5 cm, a diameter of 0.3 cm and a 39.5 kHz resonant frequency, which yields a fluid boundary layer of about 10^{-4} cm, whereas the gap containing the fluid is about 5×10^{-2} cm.

Torsional-crystal viscometers are in regular use today by *Haynes* [3.111], *Diller* and *Frederick* [3.112], *Bode* [3.113], *dos Santos* [3.114] and others. *Diller* and *Frederick* [3.112] have succeeded in expanding the temperature range of application up to 600 K. The estimated uncertainty of measurements made with these viscometers is about 2%.

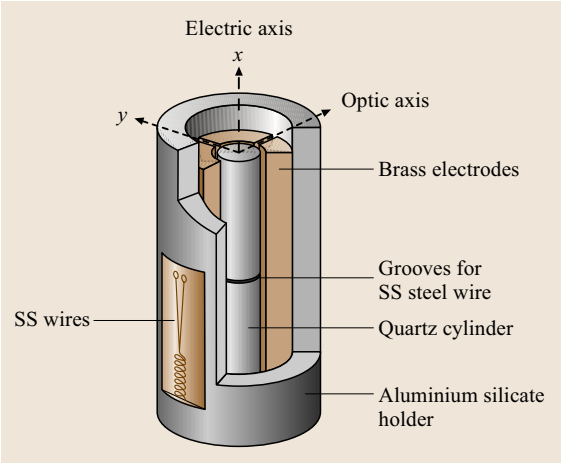

Fig. 3.37 Torsional-crystal viscometer developed by *Diller* and *Frederick* [3.112]

3.4.4 Capillary Viscometers

Capillary viscometers are the most extensively used instruments for the measurement of viscosity, especially for the liquid phase. They have the advantage of simplicity of construction and operation. They are in regular use in many countries, for standard measurements in support of industrial investigations of the viscosity of liquids at atmospheric pressure. Hence the first section describes such instruments, while the second section describes capillary viscometers for gases and liquids at high pressures.

The principle of the capillary viscometer is based on the Hagen–Poiseuille equation of fluid dynamics (first formulated by Hagen in 1839) and its alteration for practical viscometry by *Barr* [3.115] in order to include the so-called kinetic-energy correction and the end correction. The resulting equation expresses the viscosity of a fluid flowing through a thin capillary, in terms of the capillary radius a the pressure drop along the tube ΔP the volumetric flow rate Q and the length of the tube L as

$$\mu = \frac{\pi a^4 \Delta P}{8Q(L+na)} - \frac{m\rho Q}{8\pi(L+na)}\,, \tag{3.95}$$

where n is the end-correction factor and m is the kinetic-energy correction factor with $L \gg a$. The above equation is derived on the assumptions that:

1. the capillary is straight with a uniform circular cross section,
2. the fluid is incompressible and Newtonian, and
3. the flow is laminar and there is no slip at the capillary wall.

The correction factors n and m reflect the fact that in a practical viscometer two chambers must be placed at either end of the capillary in order to measure the pressure drop. Thus, for example, the parabolic velocity distribution characteristic of most of the flow can only be realized some distance downstream from the inlet of the capillary. *Kestin* et al. [3.116] obtained theoretical values for the two correction factors in the range of Reynolds numbers $0.5 \le \mathrm{Re} \le 100$, as

$$m = m_0 + \frac{8n}{\mathrm{Re}}\,, \tag{3.96}$$

where

$$m_0 = 1.17 \pm 0.03 \quad \text{and} \quad n = 0.69 \pm 0.04\,. \tag{3.97}$$

There are also a number of experimental determinations of m and n. The values for m proposed by *Swindells* et al. [3.117] are

$$m = 1.12 \text{ to } 1.16 \quad \text{for} \quad 106 \le \mathrm{Re} \le 648\,, \tag{3.98}$$

while *Kawata* et al. [3.118] reported

$$m = 1.08 \text{ to } 1.16 \quad \text{for} \quad 46 \le \mathrm{Re} \le 1466\,, \tag{3.99}$$

$$n = 0.79 \text{ to } 0.88 \quad \text{for} \quad \mathrm{Re} < 0.14\,. \tag{3.100}$$

There are a number of other secondary corrections to the working equation that can be found in literature. The most important ones are the effect of coiled capillaries [3.119], especially for gas phase measurements, the consequences of the nonuniformity of the capillary cross section [3.115] and the effects of surface tension in the case of the study of liquids.

Capillary Viscometers for Liquids

The capillary method has been employed for the absolute determination of the viscosity of primary standard liquids. The present viscosity standards within the International Organization for Standards (ISO), the American Society for Testing and Materials (ASTM), the Japanese Industrial Standards (JIS), the Deutsches Institut für Normung (DIN) are based on work by *Swindells* et al. [3.117] in 1952 with an absolute capillary viscometer. This group of workers determined the viscosity of distilled water at 20 °C and at atmospheric pressure. A schematic diagram of this viscometer is shown in Fig. 3.38. The viscometer itself was mounted in a thermostat bath together with a differential mercury manometer. The viscometer capillary, made of high quality glass tubing, had a radius of 0.2 mm, and was fitted into a glass chamber at either end. The flow of water through the capillary was generated by a piston–cylinder arrangement indicated as the main injector.

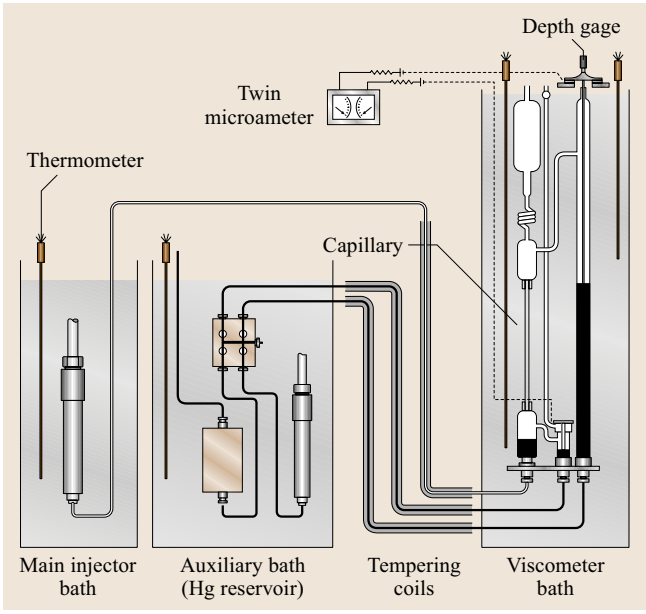

Fig. 3.38 Schematic diagram of the absolute capillary viscometer for water developed by *Swindells* et al. [3.117]

The mercury injector in the auxiliary bath forced mercury into the entrance chamber of the capillary and displaced water through it. The manometer consisted of a mercury-filled U-tube. The work of *Swindells* et al. [3.117], was characterized by great care in every aspect of measurement, to ensure the highest possible precision. The final value of the viscosity of water had an estimated uncertainty of better than 0.1%. *Kawata* et al. [3.118] described an absolute viscometer, employing a horizontal capillary, in order to check the value produced by *Swindells* et al. [3.117]. The accuracy claimed for all of these measurements has since been challenged and greater uncertainty bounds allowed but the absolute value reported by *Swindells* et al. remains intact.

For precise, measurements of the viscosity of liquids relative to this standard value, the capillary master viscometer shown in Fig. 3.39 is employed. The principle of each of the suspended-level viscometers shown in Fig. 3.39, is the measurement of the time taken for the meniscus of the sample liquid to fall from one timing mark to another in one arm of the viscometer. The marks are generally either side of a *timing* bulb and define the volume of liquid that flows during an experimental run under the influence of gravity. A master viscometer has a longer capillary, a larger timing bulb of oval shape and a cylindrical lower bulb compared with a routine viscometer. These differences serve to minimize the various errors, and render negligible the effect of the second term in (3.95).

For a capillary master viscometer, if $Q = V/t$, where t denotes the time required for volume V (in the timing bulb) to flow through the capillary, and $\Delta P = \rho g h$, where h is the mean effective height of the liquid column, then (3.95) becomes

$$\mu = \frac{\pi a^4 g h t}{8(L+na)V} - \frac{mV}{8\pi(L+na)t} \qquad (3.101)$$

or

$$\mu = c_1 t - \frac{c_2}{t}\,, \qquad (3.102)$$

where c_1 and c_2 are obtained from (3.101).

Routine capillary viscometers are used for many industrial measurements because they are very simple to use and permit rapid operation while yielding results of adequate accuracy. Some variations of such routine viscometers from among the many variants are shown in Fig. 3.39. For these viscometers (3.102) remains valid but the constants c_1 and c_2 are determined by calibration with fluids of known viscosity rather than from theory.

Capillary Viscometers for High Pressures

The capillary method is also suitable for application to gases and liquids at high pressures. However, in addition to the factor discussed in the previous section, a number of special precautions have to be considered. For example for measurements on gases, the measurement of the flow rate is difficult and corrections for compressibility and for slip at the capillary wall have to be considered. In addition, measurements at high pressures require a high-pressure construction for the whole system, a manometer to measure a small pressure difference in the presence of a high total pressure etc.

Assuming the fluid to be an ideal gas and the pressure drop between both ends of the capillary small, then the correction for compressibility is simple, and (3.95) becomes

$$\mu = \frac{\pi a^4 (P_1 - P_2)}{8 Q_1 (L + na)} \frac{(P_1 + P_2)}{2 P_1} - \frac{\rho_1 Q_1}{8\pi (L + na)} \left(m + \log \frac{P_1}{P_2} \right) , \quad (3.103)$$

where P_1 and P_2 are the pressures at the inlet and the exit of the capillary and Q_1 is the volumetric flow rate at entry. The slip correction, proposed by *Knudsen* for such circumstances, modifies the working equation to [3.83]

$$\mu = \frac{\pi a^4 (P_1 - P_2)}{8 Q_1 (L + na)} \frac{(P_1 + P_2)}{2 P_1} \left(1 + \frac{4\zeta}{a} \right) , \quad (3.104)$$

where the slip correction ζ is calculated as

$$\zeta = 2.16 \mu \sqrt{\frac{4}{\pi (P_1 + P_2) \rho}} . \quad (3.105)$$

For high-pressure and/or high-temperature measurements, coiled capillaries are sometimes employed in order to secure a sufficiently long flow tube while maintaining uniformity of temperature. This kind of arrangement modifies the basic working equation because of the introduction of new velocity components into the flow. In most circumstances the effects can be treated as a correction to the basic equation so long as appropriate care is taken. A successful gas capillary designed by Michels and operated by *Trapeniers* et al. [3.119] for measurements on gases up to 100 MPa, is shown in Fig. 3.40.

Nagashima et al. [3.120] employed a closed-circuit capillary viscometer for measurements of the viscosity of water and heavy water in the liquid and vapor phase at temperatures in the range 50–500 °C and pressures up to 80 MPa. A similar apparatus was described by *Rivkin* et al. [3.121] for measurements in the critical region of water. *Guevara* et al. [3.122] employed a capillary viscometer for gases up to 2000 K while *Ejima* et al. [3.123] applied a capillary viscometer to measurement of the viscosity of molten salts up to 1200 K.

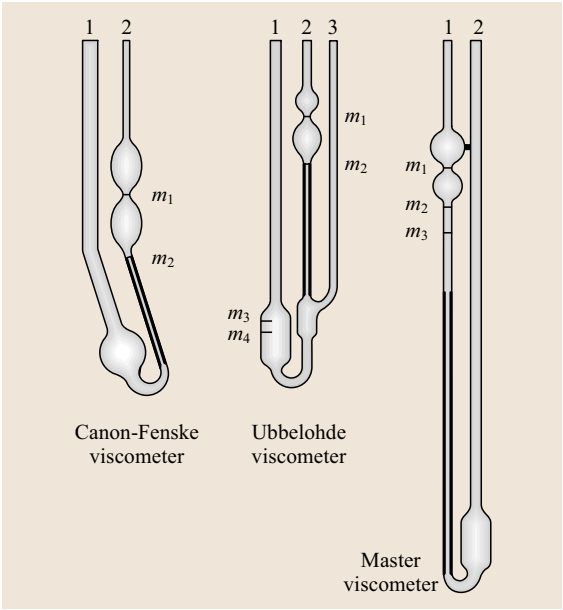

Fig. 3.39 Capillary master and routine viscometers

3.4.5 Falling-Body Viscometers

Falling-body viscometers involve the use of the time of free-fall of an object under the influence of gravity through the fluid of interest to determine the viscosity. Generally, the falling body is a body of revolution and has most commonly been a sphere or a cylinder. Generally, the instruments are not among those of the highest accuracy because it is rather difficult to ensure that the instrument operates in line with a theory of it. However, exceptionally, such instruments have been used for accurate measurements including work in Japan on a new standard reference viscometer [3.83]. More usual instruments of the same type have a number of advantages for operation at very high pressures that make them useful for routine measurements in industry.

Falling-Sphere Viscometer

The principle of a falling-sphere, or falling-ball, viscometer is based on Stokes' law. This law results from the creeping-flow Stokes equations valid for very low Reynolds numbers. For that reason this type of viscometer is usually applicable to the precision measurement of

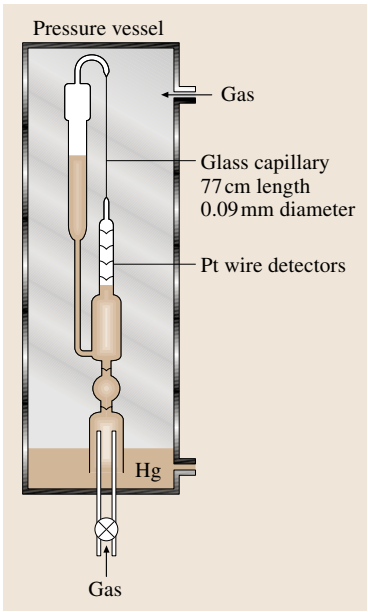

Fig. 3.40 High-pressure gas capillary viscometer developed by *Trapeniers* et al. [3.119]

the viscosity of highly viscous liquids or measurements under high pressure. In routine operation the viscometers are used in a relative manner using a calibration of the instrument with standard liquids. For a sphere of radius a, falling through a distance L, the viscosity of the fluid is given as

$$\mu = \frac{2a^2(\rho_s - \rho)gt}{9L} f_w \,, \tag{3.106}$$

where ρ_s is the density of the sphere, and t the fall time. This equation is valid provided the motion is very slow, the fluid is infinite, incompressible and Newtonian, and there is no slip between the fluid and the sphere's surface. Also the ball must fall vertically without rotation. The correction factor f_w accounts for the effect of the inevitable presence of a wall containing the fluid. It is usually obtained by calibration with fluids of known viscosity. If R is the radius of the cylindrical container and provided a/R and Re are sufficiently small (Re $\ll 1$), *Faxen* [3.126] has derived theoretically the following correction factor

$$f_w = 1 - 2.109\left(\frac{a}{R}\right) + 2.09\left(\frac{a}{R}\right)^3 - 0.95\left(\frac{a}{R}\right)^5 . \tag{3.107}$$

To measure the fall time, at atmospheric pressure a glass cylinder is often employed to contain the fluid because it allows optical observation of the fall time in a transparent fluid. *Flude* and *Daborn* [3.127] performed measurements using a laser Doppler effect and attained a precision of ±0.07% in the time. When the liquid is opaque, the fall velocity can be measured by various techniques for example by recording the inductance changes in a coil wound on the fall tube owing to the passage of the ball. For high-pressure measurements

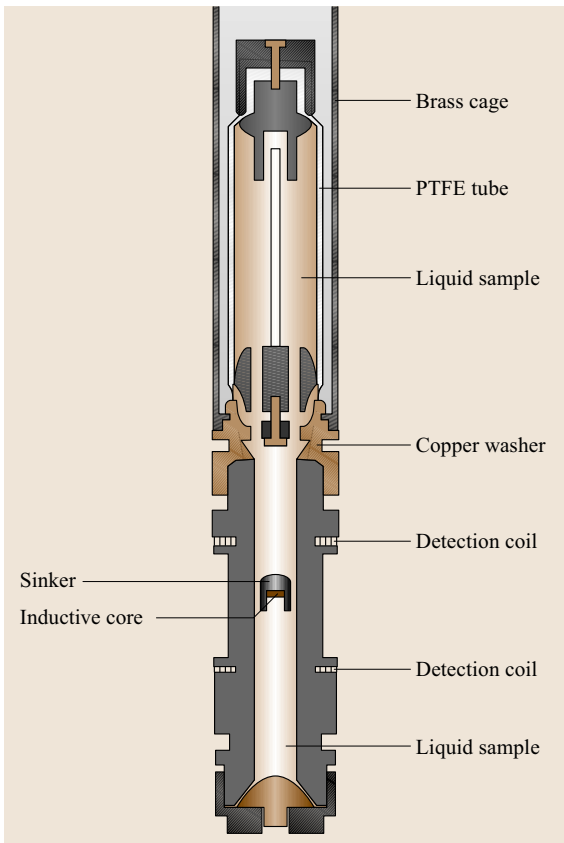

Fig. 3.41 Falling-cylinder viscometer developed by *Isdale* [3.124] and *Irvine* [3.125]

Table 3.11 Reference values for the viscosity of noble gases at a pressure of 0.1 MPa

	Viscosity (μPa s)				
T (°C)	Helium	Neon	Argon	Krypton	Xenon
25	19.86	31.76	22.62	25.39	23.09
100	23.16	37.06	27.32	31.22	28.84
200	27.35	43.47	32.85	38.06	35.91
300	31.28	49.50	37.83	44.28	42.38
400	35.04	55.00	42.35	49.99	48.32
500	38.60	60.19	46.63	55.34	53.84

Table 3.12 Viscosity μ (μPa s) of some *n*-alkanes in the liquid phase

		P (MPa)	273.15 K	298.15 K	323.15 K	348.15 K	373.15 K
n-Pentane	C_5H_{12}	0.101	286.4	220.3	174.8	141.0	114.3
		5	301.1	232.4	185.3	150.5	122.8
		10	316.1	244.4	195.6	159.7	130.8
		25	361.6	279.9	225.0	184.6	151.6
		50	439.8	338.7	271.4	222.1	181.3
n-Hexane	C_6H_{14}	0.101	384.7	295.7	237.8	196.5	164.5
		5	403.8	310.9	251.0	208.6	176.0
		10	423.5	326.3	264.1	220.4	187.0
		25	483.8	372.8	302.9	254.5	217.5
		50	590.4	452.4	367.1	308.8	264.3
n-Heptane	C_7H_{16}	0.101	530.9	392.5	307.4	249.8	207.6
		5	557.9	412.5	323.6	264.0	220.6
		10	586.0	433.1	340.1	278.1	233.3
		25	673.6	496.0	389.6	319.6	269.7
		50	831.7	606.6	474.0	388.2	327.6
n-Octane	C_8H_{18}	0.101	754.3	531.6	401.9	318.6	260.5
		5	795.5	559.9	423.4	336.4	276.1
		10	838.5	589.2	445.5	354.4	291.7
		25	974.3	680.4	513.0	408.3	337.1
		50	1225	844.7	631.4	500.0	411.9
n-Nonane	C_9H_{20}	0.101	995.5	677.5	498.3	387.1	312.4
		5	1052	714.2	524.9	408.2	330.2
		10	1112	752.4	552.5	429.8	348.2
		25	1298	872.4	637.4	495.0	401.6
		50	1649	1092	788.7	607.9	491.1
n-Decane	$C_{10}H_{22}$	0.101	1364	886.6	630.0	477.3	378.2
		5	1445	936.9	664.7	503.5	399.6
		10	1531	989.4	700.7	530.5	421.3
		25	1805	1156	813.0	613.2	486.6
		50	2328	1465	1016	758.8	598.2
n-Undecane	$C_{11}H_{24}$	0.101	1738	1098	761.5	565.9	441.8
		5	1844	1161	803.8	596.8	466.3
		10	1956	1228	847.8	628.7	491.2
		25	2318	1439	985.7	727.1	566.7
		50	3010	1835	1238	902.3	697.3
n-Dodecane	$C_{12}H_{26}$	0.101	2319	1404	941.2	681.4	521.9
		5	2466	1488	994.7	719.1	550.7
		10	2622	1576	1051	758.1	580.2
		25	3129	1859	1227	879.4	670.2
		50	4112	2395	1554	1098	827.8

sapphire optical windows are sometimes set into the pressure vessel to permit observation of the motion.

Falling-Cylinder Viscometer

An alternative realization of a falling-body viscometer makes use of a right circular cylinder falling under the influence of gravity along the axis of a coaxial cylindrical tube. This arrangement has the advantage that it is possible to secure a low Reynolds number for the fluid flow by choosing a suitable geometry, or by reducing the cylinder's mass by making it hollow.

For a cylinder of radius r_1 and length L_s, in a tube of radius r_2, the viscosity is given by [3.124]

$$\mu = \frac{(1-\rho/\rho_s)}{A} t \,, \tag{3.108}$$

Table 3.13 Viscosity μ (μPa s) of some alkenes in the liquid phase

		P (MPa)	273.15 K	298.15 K	323.15 K	348.15 K	373.15 K
Benzene	C_6H_6	0.101	857.6	593.8	435.4	334.0	265.0
		5	897.6	621.1	455.4	349.6	278.0
		10	939.5	649.5	476.0	365.6	291.0
		25	1072	737.9	539.5	414.0	329.8
		50	1314	897.8	651.8	497.5	394.7
Toluene	C_7H_8	0.101	761.7	538.2	408.5	326.6	271.1
		5	793.5	560.1	425.2	340.5	283.5
		10	826.5	582.8	442.4	354.7	296.0
		25	929.9	652.9	494.9	397.3	333.1
		50	1117	777.5	586.4	470.2	395.0
Ethylbenzene	C_8H_{10}	0.101	862.6	614.5	467.6	373.5	308.9
		5	900.0	640.8	487.8	390.4	324.0
		10	939.0	668.1	508.7	407.7	339.3
		25	1062	753.1	573.3	460.5	385.3
		50	1286	906.1	687.5	552.4	464.0
o-Xylene	C_8H_{10}	0.101	1091	749.8	559.8	444.4	369.1
		5	1137	780.5	582.5	462.8	385.1
		10	1186	812.5	606.1	481.7	401.5
		25	1338	912.3	678.9	539.8	451.3
		50	1617	1093	808.3	641.3	537.0
m-Xylene	C_8H_{10}	0.101	772.1	562.0	434.1	350.4	291.9
		5	804.9	585.7	452.8	366.2	306.2
		10	839.0	610.3	472.1	382.4	320.7
		25	946.1	686.8	531.5	431.9	364.4
		50	1141	824.3	636.6	518.1	439.1
p-Xylene	C_8H_{10}	0.101	798.2	583.3	452.1	365.9	305.5
		5	831.4	607.4	471.1	382.1	320.2
		10	866.0	632.4	490.7	398.7	335.1
		25	974.2	709.9	551.1	449.1	379.7
		50	1171	848.6	657.4	536.4	455.6
Mesitylene	C_9H_{12}	0.101	941.2	657.5	494.1	392.1	324.1
		5	983.8	686.8	516.3	410.4	340.3
		10	1028	717.4	539.3	429.2	356.8
		25	1169	813.2	610.9	487.4	407.3
		50	1429	987.5	739.6	590.3	495.5

where

$$A = \frac{2\pi L_s L_T}{mg\left\{\ln(r_2/r_1) - \left[\left(r_2^2 - r_1^2\right)/\left(r_2^2 + r_1^2\right)\right]\right\}} \,. \tag{3.109}$$

Here, ρ is the density of the liquid and ρ_s the density of the material of the cylinder, while L_s is the distance traveled by the falling body of mass m.

There are many difficulties in a practical instrument, because it is impossible to ensure that the falling body and its tube are perfectly cylindrical and that the former falls along the axis of the latter. A number of different designs have been developed to try to ensure correct operation that include a wide variety of shapes for the front face of the falling body itself. Pins protruding from the falling body perpendicular to its length have been employed in the past, to ensure concentricity. However, they were unsuccessful as the influence of friction between the pins and the wall was high.

An alternative approach is to design the falling body as a self-centering device. This was done successfully by

Table 3.14 Viscosity μ (μPa s) of some *n*-alcohols in the liquid phase

		P (MPa)	273.15 K	298.15 K	323.15 K	348.15 K	373.15 K
Methanol	CH_4O	0.101	772.2	568.3	408.1	312.3	271.5
		5	787.6	581.7	418.7	320.7	278.4
		10	803.0	595.0	429.1	328.9	285.1
		25	847.5	633.0	458.6	351.6	303.4
		50	917.4	691.8	503.2	385.2	330.0
Ethanol	C_2H_6O	0.101	1699	1104	719.5	494.4	380.3
		5	1743	1134	739.8	508.4	390.6
		10	1787	1164	760.2	522.3	400.7
		25	1920	1254	819.5	562.1	429.2
		50	2141	1401	914.0	624.1	472.6
1-Propanol	C_3H_8O	0.101	3535	1989	1141	827.2	854.8
		5	3653	2062	1185	858.6	885.7
		10	3774	2135	1229	890.4	916.6
		25	4145	2361	1362	985.1	1007
		50	4790	2749	1589	1143	1153
1-Butanol	$C_4H_{10}O$	0.101	4503	2524	1382	833	622.1
		5	4706	2644	1447	870	647.5
		10	4919	2769	1515	909	673.3
		25	5587	3160	1726	1026	750.1
		50	6812	3874	2104	1231	878.7
1-Pentanol	$C_5H_{12}O$	0.101	7203	3393	1706	1046	812.5
		5	7608	3581	1795	1094	844.9
		10	8037	3780	1887	1144	877.8
		25	9418	4415	2178	1297	976.1
		50	12057	5614	2713	1567	1141
1-Hexanol	$C_6H_{14}O$	0.101	8893	4303	2206	1263	809.3
		5	9451	4554	2319	1318	839.3
		10	10045	4820	2437	1374	869.7
		25	11979	5675	2810	1549	960.2
		50	15756	7311	3499	1855	1111
1-Heptanol	$C_7H_{16}O$	0.101	14217	5712	2658	1473	946.0
		5	15133	6041	2787	1533	978.7
		10	16110	6388	2921	1594	1012
		25	19301	7506	3345	1782	1110
		50	25568	9643	4123	2110	1273
1-Octanol	$C_8H_{18}O$	0.101	19606	7145	3240	1811	1182
		5	20866	7545	3392	1882	1222
		10	22208	7969	3551	1955	1263
		25	26598	9330	4050	2179	1385
		50	35222	11926	4962	2571	1588

Isdale [3.124], *Irvine* [3.125], *Glen* [3.128] and others, and measurements of the viscosity of hydrocarbons at very high pressures were reported. The measurements were performed on a relative basis with an estimated uncertainty of 2–3% in the final values.

3.4.6 Viscosity Reference Values

The internationally agreed standard for viscosity, ISO/TR 3666:1998, is the viscosity of water at 20 °C and atmospheric pressure (0.101325 MPa), and its approved

Table 3.15 Viscosity μ (μPa s) of some refrigerants in the liquid phase

		P (MPa)	248.15 K	273.15 K	298.15 K	323.15 K	348.15 K
R22	$CHClF_2$	5	292.1	224.0	173.4	131.8	94.2
		10	304.8	236.1	185.8	145.2	111.1
		25	341.0	269.0	217.0	175.4	142.3
R32	CH_2F_2	5	229.5	167.3	124.0	89.4	
		10	240.1	176.3	132.6	98.6	82.5
		25	269.0	199.0	152.2	116.1	112.4
R124	C_2HClF_4	5	529.2	369.8	274.3	210.8	159.2
		10	549.5	389.8	296.3	234.1	180.3
		25	610.6	448.2	356.6	292.8	228.2
R125	C_2HF_5	5	310.2	223.9	161.5	112.2	
		10	328.6	240.7	178.9	132.8	
		25	379.3	283.2	217.8	170.6	
R134a	$C_2H_2F_4$	5	405.7	295.2	219.4	161.8	114.6
		10	430.5	314.5	236.4	178.6	133.7
		25	503.6	368.6	280.8	218.3	172.0
R141b	$C_2H_3ClF_2$	5	829.5	577.5	429.8	333.3	265.5
		10	858.3	602.2	451.9	353.1	283.9
		25	946.8	677.5	518.1	410.5	335.4
R152a	$C_2H_4F_2$	5	337.8	230.9	173.7	134.8	103.3
		10	355.5	243.6	185.1	146.8	117.5
		25	407.9	279.3	215.4	176.0	147.8

value is

$$\mu = 1.0016\,\text{mPa s}\,. \tag{3.110}$$

This value has an estimated relative uncertainty of ±0.17%. This is based on the value of 1.0019 mPa s reported by *Swindells* et al. [3.117] in 1952, which was also the basis of ISO/TR 3666:1977. The small difference in value is due to the difference between the ITS-48 and ITS-90 temperature scales.

The temperature dependence of the viscosity of water at atmospheric pressure in the temperature range 0.01–100 °C, is given by the following recommended correlation [3.129]

$$\log \frac{\mu(\theta)}{\mu(20\,^\circ\text{C})} = \frac{\theta}{116-\theta} \times \left(1.2378 - 1.303\times10^{-3}\theta + 3.06\times10^{-6}\theta^2 + 2.55\times10^{-8}\theta^3\right)\,, \tag{3.111}$$

where $\theta = 20 - T(^\circ C)$. The estimated uncertainty of (3.111) is better than ±0.1%.

In the case of the viscosity of gases, nitrogen is usually employed as a standard, since it is readily available with high purity and is also inexpensive to obtain. The following value is recommended [3.83] for the viscosity of nitrogen at 25 °C and atmospheric pressure:

$$\mu = (17.710 \pm 0.016)\,\mu\text{Pa s}\,. \tag{3.112}$$

Recommended values for the viscosity of the noble gases at a pressure of 0.1 MPa are shown in Table 3.11. They have been calculated using a combination of experimental data and available theory and their estimated uncertainty is ±0.2% in the range 25–200 °C, and ±0.4% in the range 200–500 °C.

For use at higher pressures, up to 30 MPa, and at a temperature of 25 °C, the viscosity of nitrogen is represented by the equation [3.83]

$$\mu = 0.17763\times10^{-4} + 0.86870\times10^{-8}\rho + 0.14240\times10^{-9}\rho^2\,, \tag{3.113}$$

where μ is measured in Pa s and ρ in kg/m^3. Other secondary viscosity reference fluids are available in the literature [3.83].

3.4.7 Tables of Viscosity Values

In Tables 3.12–3.16, the viscosity of commonly encountered fluids is given for use in engineering calculations, as a function of both temperature and pressure. The val-

Table 3.16 Viscosity μ (μPa s) of some gases

		P (MPa)	273.15 K	298.15 K	323.15 K	348.15 K	373.15 K
Argon	Ar	0.101	21.26	22.73	24.14	25.50	26.82
		5	22.43	23.73	25.01	26.26	27.49
		10	24.32	25.29	26.32	27.39	28.48
Hydrogen	H_2	0.101	8.33	8.86	9.36	9.85	10.32
		5	8.40	8.92	9.42	9.90	10.36
		10	8.50	9.00	9.49	9.96	10.42
Nitrogen	N_2	0.101	16.54	17.62	18.66	19.66	20.62
		5	17.46	18.40	20.25	20.25	21.15
		10	18.89	19.59	20.34	21.12	21.91
Oxygen	O_2	0.101	19.12	20.48	21.79	23.05	24.28
		5	20.18	21.39	22.58	23.75	24.89
		10	21.90	22.80	23.77	24.77	25.78
Carbon monoxide	CO	0.101	16.47	17.61	18.70	19.75	20.77
		5	17.44	18.43	19.41	20.37	21.32
		10	18.99	19.70	20.49	21.30	22.13
Carbon dioxide	CO_2	0.101	13.96	15.14	16.28	17.38	18.46
		5		17.95	18.46	19.21	20.04
		10			29.35	23.64	23.16
Sulfur dioxide	SO_2	0.101	11.87	12.97	14.06	15.15	16.24
Hydrogen sulfide	H_2S	0.101	11.76	12.86	13.94	15.01	
		5				17.26	
Methane	CH_4	0.101	10.34	11.14	11.92	12.67	13.39
		5	11.49	12.11	12.75	13.39	14.04
		10	13.84	13.88	14.17	14.58	15.05
Ethane	C_2H_6	0.101	8.69	9.44	10.17	10.88	11.57
		5			13.47	13.26	13.51
		10			38.33	24.83	19.37
Propane	C_3H_8	0.101	7.61	8.28	8.93	9.57	

ues quoted are therefore not intended to be the best possible values for the viscosity of a particular fluid but are intended to be of sufficient accuracy to be useful. The fluids and the temperature and pressure conditions chosen are the same as chosen for the density and thermal conductivity in Sects. 3.1 and 3.4.

Values for the liquid viscosity are based on a large collection of experimental data correlated by a semi-empirical hard-spheres-based procedure available in the literature (n-alkanes [3.130], n-alkenes [3.131], n-alcohols [3.132], refrigerants [3.133]). The uncertainty of the quoted liquid viscosity values is much better than ±5%. Values for the gas-phase viscosity have been obtained from corresponding-states software [3.37], itself based upon experiment; it is estimated that the uncertainty is less than 2%.

3.5 Thermal Conductivity and Thermal Diffusivity

The thermal conductivity is defined by Fourier's law. In one group of instruments described in this chapter the use of a time-dependent heating perturbation is applied to the fluid, and the time dependence of the temperature in the fluid is measured and related to the thermal conductivity. In the second group a continuous and constant heat source establishes a steady temperature distribution in the fluid whose measurement again yields the thermal conductivity of the fluid. The instruments have different

attributes which make them suitable for particular applications.

The thermal conductivity of a fluid measures its propensity to dissipate energy, when disturbed from equilibrium by the imposition of a temperature gradient. For isotropic fluids the thermal conductivity λ is defined by Fourier's law

$$\boldsymbol{Q} = -\lambda \nabla T \,, \tag{3.114}$$

where $\boldsymbol{Q}$ is the instantaneous flux of heat, which is the response of the medium to the instantaneous temperature gradient. The thermal conductivity depends on the thermodynamic state of the fluid. Because it is impossible to measure local fluxes and local gradients, (3.114) cannot be employed directly to measure the thermal conductivity of a fluid.

The rate of heat propagation through a fluid is described by its thermal diffusivity a defined as

$$a = \frac{\lambda}{\rho C_\mathrm{p}} \,, \tag{3.115}$$

where ρ is the fluid density and C_p its isobaric heat capacity. In some techniques, the thermal conductivity is obtained indirectly from the measured thermal diffusivity, provided the density and the isobaric heat capacity of the fluid are known.

The starting point for the formulation of the working equations to measure the thermal conductivity of a fluid is the equation of energy conservation which, for a Newtonian, viscous, isotropic and incompressible fluid, with temperature-dependent properties, can be written [3.134]

$$\rho \frac{\mathrm{d}U}{\mathrm{d}t} = -\nabla \cdot \boldsymbol{Q} - P(\nabla \cdot \boldsymbol{v}) - \boldsymbol{\sigma} : \boldsymbol{\varepsilon} \,, \tag{3.116}$$

where U is the internal energy, t the time, P the hydrostatic pressure, $\boldsymbol{v}$ the hydrodynamic velocity of the fluid, $\boldsymbol{\sigma}$ the stress tensor, ρ the density and $\boldsymbol{Q}$ the heat flux vector. The notation $\mathrm{d}/\mathrm{d}t$ represents the substantive derivative [3.134]. On the assumption that the temperature perturbation is small and that a local-equilibrium thermodynamic state exists, (3.116) can be transformed to

$$\rho C_v \frac{\mathrm{d}U}{\mathrm{d}t} - T\left(\frac{\alpha_\mathrm{p}}{k_\mathrm{T}}\right)\left(-\alpha_\mathrm{p} + k_\mathrm{T}\frac{\mathrm{d}P}{\mathrm{d}T}\right)\frac{\mathrm{d}T}{\mathrm{d}t} = -\nabla \cdot \boldsymbol{Q} + \phi \,, \tag{3.117}$$

where C_v is the isochoric heat capacity, α_p the isobaric expansion coefficient, k_T the isothermal compressibility and $\phi = \boldsymbol{\sigma} : \boldsymbol{\varepsilon}$ is the rate of internal energy increase owing to viscous dissipation. Assuming that $k_\mathrm{T}(\mathrm{d}P/\mathrm{d}T) \ll \alpha_\mathrm{p}$, (3.117) can be written

$$\rho C_\mathrm{p} \frac{\mathrm{d}T}{\mathrm{d}t} = -\nabla \cdot \boldsymbol{Q} + \phi \,. \tag{3.118}$$

A general solution of (3.118) is not possible; thus it is necessary to apply a number of further restrictions before it can be employed as the basis of determinations of thermal conductivity. It is further assumed that fluid movements are avoided, so that $\boldsymbol{v} = 0$ and consequently $\phi = 0$. It is therefore necessary to make measurements of the thermal conductivity in such a way that the effect of convection is negligible even if it is unavoidable. Assuming further that the radiative heat flux is rendered negligible and employing Fourier's law (3.114) then, for an isotropic fluid with a temperature-independent thermal conductivity, density and heat capacity, (3.118) can be written

$$\rho C_\mathrm{p} \frac{\partial T}{\partial t} = \lambda \nabla^2 T \,. \tag{3.119}$$

Equation (3.119) is the basis for all experimental methods for the measurement of the thermal conductivity.

In the last 30 years a variety of experimental methods have been developed, both for liquid or gaseous phases, to cover a wide range of thermodynamic states. These methods, according to the use of (3.119) can be classified in two main categories:

- Transient or unsteady-state techniques, in which the full (3.119) is used and the principal measurement is the temporal history of the fluid temperature,
- Steady-state techniques, for which $\partial T/\partial t = 0$, and (3.119) reduces to $\lambda \nabla^2 T = 0$, which can be integrated for a given geometry.

3.5.1 Transient Methods for Thermal Conductivity

The main difficulty in performing accurate measurements of the thermal conductivity of fluids lies in the realization of two of the conditions above. It should be possible to isolate the conduction process from other mechanisms of heat transfer.

The imposition of a temperature gradient in a compressible fluid in the gravitational field of the earth inevitably creates a state of motion (natural convection) so that pure conduction in a fluid is very difficult to achieve. The success of transient techniques for the

measurement of the thermal conductivity of fluids is based on the fact that the characteristic time for the acceleration of the fluid by buoyancy forces is much longer than the propagation time of a temperature wave originated by a strong and localized temperature gradient. In this section two transient techniques are described: the transient hot-wire technique applicable over a wide range of conditions and an interferometric technique especially suited to the critical region.

The advantages of the transient hot-wire technique are that it permits the user to obtain the thermal conductivity by the use of an exact working equation resulting from a careful mathematical model of the instrument as well as to eliminate convective contributions to the heat transfer from the measurement. The transient hot-wire technique is an absolute technique and the instruments based on its principle are considered primary instruments and are capable of providing the lowest uncertainty possible at present. The uncertainty of the measurements has been confirmed by performing measurements in low-density noble gases, for which an exact molecular theory exists [3.135]. It has been applied successfully in most regions of the phase diagram, except very close to the critical point where the temperature gradients used are too large to maintain a state sufficiently near equilibrium, owing to large fluctuations in density and long-range correlations. It is in this particular region that the interferometric technique is singularly appropriate because it has the unique advantage that the nearer the critical point is approached the smaller can be the applied temperature gradient. Thus, the two transient techniques are complimentary.

Transient Hot-Wire Technique

A transient thermal conductivity measurement is one in which a time-dependent perturbation, in the form of a heat flux, is applied to a fluid initially at equilibrium. The thermal conductivity is obtained from an appropriate working equation relating the observed response of the temperature of the fluid to the perturbation. In principle, one can devise a wide variety of techniques of this kind. However, the only geometrical arrangement applied over a wide range of conditions is one in which the perturbing heat flux is applied by means of electrical dissipation in a thin, cylindrical wire as a step function. In this case the wire is itself used as the thermometer to monitor the temperature rise of the fluid at its interface.

The temperature rise in the fluid at a distance r from the wire at a time t, can be defined

$$\Delta T(r,t) = T(r,t) - T_0 \,. \tag{3.120}$$

It can easily be shown [3.136] that for a cylindrical wire of radius r_0, and for small values of the term $(r_0^2/4at)$,

$$\Delta T\,(r_0,t) = \frac{q}{4\pi\lambda}\left[\ln\left(\frac{4at}{r_0^2\gamma}\right) + \left(\frac{r_0^2}{4at}\right) + \ldots\right], \tag{3.121}$$

where $\Delta T(r_0,t)$ is the transient temperature rise of the fluid at the wire surface, λ and a the thermal conductivity and thermal diffusivity of the fluid, respectively, q the heat input power per unit length, and $\gamma = 0.577216$ is the Euler–Mascheroni constant. In the ideal model, (3.121) describes the temperature rise of the wire in contact with the fluid at its surface. In practice a real instrument departs from the ideal model in a number of respects and analytical corrections have been developed [3.136] for the departure of a practical instrument from the ideal one. The two major additive corrections to (3.121) that need to be applied in practice are:

1. The heat capacity correction ΔT_{hc} significant only at short experimental times [3.137],

$$\begin{aligned}\Delta T_{\mathrm{hc}} &= \frac{2q^{1/2}}{\pi^2 r_0^2}\int_0^\infty \left(1 - \mathrm{e}^{-a_{\mathrm{w}}u^2 t}\right) J_1(ur_0) \\ &\times\left[J_0\left(\sqrt{\frac{a_{\mathrm{w}}}{a}}ur_0\right)\phi(u) - Y_0\left(\sqrt{\frac{a_{\mathrm{w}}}{a}}ur_0\right)\phi(u)\right] \\ &\times\left\{u^3\left[\phi^2(u)+\psi^2(u)\right]\right\}^{-1}\mathrm{d}u\,,\end{aligned} \tag{3.122}$$

with

$$\begin{aligned}\phi(u) &= \lambda_{\mathrm{w}} a^{1/2} J_1(ur_0) J_0\left(\sqrt{\frac{a_{\mathrm{w}}}{a}}ur_0\right) \\ &\quad - \lambda a_{\mathrm{w}}^{1/2} J_0(ur_0) J_1\left(\sqrt{\frac{a_{\mathrm{w}}}{a}}ur_0\right)\,,\end{aligned} \tag{3.123}$$

$$\begin{aligned}\psi(u) &= \lambda_{\mathrm{w}} a^{1/2} J_1(ur_0) Y_0\left(\sqrt{\frac{a_{\mathrm{w}}}{a}}ur_0\right) \\ &\quad - \lambda a_{\mathrm{w}}^{1/2} J_0(ur_0) Y_1\left(\sqrt{\frac{a_{\mathrm{w}}}{a}}ur_0\right)\,.\end{aligned} \tag{3.124}$$

In these expressions, r_0 is the wire radius and the subscript 'w' refers to wire properties. Furthermore, J_0 and J_1 denote Bessel functions of first kind, of order zero and one, respectively, while Y_0 and Y_1 express Bessel functions of second kind, of order zero and one.

2. The outer boundary correction, ΔT_{ob}, significant only at long experimental times

$$\Delta T_{ob}(r_0, t) = \frac{q}{2\pi\lambda} \ln \frac{b}{r_0} + \frac{q}{2r_0\lambda} \sum_{n=1}^{\infty} e^{-aa_n^2 t} \times \frac{J_0^2(ba_n)\left[J_0(r_0a_n)Y_1(r_0a_n) - Y_0(r_0a_n)J_1(r_0a_n)\right]}{a_n\left[J_1^2(r_0a_n) - J_0^2(ba_n)\right]} , \quad (3.125)$$

where b is radius of the cylindrical fluid enclosure and α_n are the positive roots of the equation

$$J_1(r_0x)Y_0(bx) - Y_1(r_0x)J_0(bx) = 0 . \quad (3.126)$$

Healy et al. [3.136] proposed approximate expressions of (3.122) and (3.125) valid for large values of $(4at/r_0^2)$. These expressions together with (3.121) form a consistent set in order to calculate the thermal conductivity from the measured temperature rise. The application of this methodology to liquids and gases at moderate pressures has provided many reliable thermal-conductivity data over the last two decades. Unfortunately, the analytical corrections proposed by *Healy* et al. [3.136] proved to be inadequate [3.137] for the description of experiments in the gas phase at low densities, where fluids exhibit exceedingly high thermal-diffusivity values.

To overcome these difficulties, a numerical finite-element method was proposed by *Assael* et al. [3.137], in order to solve the complete set of energy-conservation equations that describe the heat-transfer experimental processes. The choice of this particular numerical method was dictated by the high accuracy the method exhibits in computational heat transfer problems. The energy equations to be solved are two coupled partial differential equations, one for the wire, $0 < r \geq r_0$:

$$\left(\rho c_p\right)_w \frac{\partial T_w}{\partial t} = \lambda_w \nabla^2 T_w - \frac{q}{\pi r_0^2} , \quad (3.127)$$

and one for the fluid, $r_0 \geq r < \infty$:

$$\left(\rho c_p\right) \frac{\partial T}{\partial t} = \lambda \nabla^2 T . \quad (3.128)$$

On the wire/fluid interface both the temperature and the heat flux are considered to be continuous. This means that for $r = r_0$,

$$\lambda_w \left(\frac{\partial T_w}{\partial r}\right)_{r=r_0} = \lambda \left(\frac{\partial T}{\partial r}\right)_{r=r_0} \quad (3.129)$$

and

$$T_w(r_0, t) = T(r_0, t) . \quad (3.130)$$

This set of equations was solved subject to a suitable set of initial conditions on a straight wire [3.137]. As it can be seen from the conditions (3.129) and (3.130), the problem is one-dimensional with respect to the radial direction. *Assael* et al. [3.137] employed a forward difference (Euler) scheme coupled with a modification of the Gaussian elimination method (LU decomposition method). In practice, experimental means are employed to yield a finite segment of a wire that behaves as if it were part of an infinite wire. This allows the numerical solution of the differential equations to be used iteratively to determine the thermal conductivity and diffusivity of the fluid that yields the best match between the experimental and calculated temperature rise of this finite segment of wire.

Since the technique was first employed by *Stalhane* and *Pyk* [3.138] in 1931 to measure the thermal conductivity of powders, there have been significant improvements in the practical realization of the technique. In modern instruments the wire sensor acts both as the heat source and as a thermometer. Rapid development of analogue and digital equipment as well as of computer-driven data-acquisition systems have meant that precise measurements of transient electrical signals can be made quickly. Thus, it has become possible to measure the resistance change taking place in the hot wire as a consequence of its temperature rise with a precision better than 0.1%. Furthermore, instead of a single wire, two wires identical in all respects except for length, are employed. This allows a practical and automatic means of compensating for the finite length of the wires. For electrically insulating fluids platinum has usually been employed as the heating wire and sensing thermometer because of its chemical stability and resistance/temperature characteristics. In order to allow measurements of electrically conducting fluids, tantalum wires are often employed, because tantalum upon electrolytic oxidation forms tantalum pentoxide on its surface, which is an electrical insulator. Together with a more systematic approach to the theory it has been possible to provide instruments with an uncertainty of $\pm 0.5\%$.

The theory assumes that the heat source is straight and stationary. To ensure that this is true a mechanism must be used to take up the thermal expansion of the wire as it undergoes transient heating. At the same time the expansion of the wire and its supports must not impose undue stresses during temperature

change of the whole assembly. The simplest means of doing this is illustrated in Fig. 3.42 where the wires are tensioned by small weights. In Fig. 3.43 the wires are pretensioned between fixed supports but the supports of the wires and the wires themselves are made of the same material, tantalum; so that the wires are kept under constant tension even when the temperature changes.

To register with high accuracy the resistance change of the wire, and thus its temperature change, an electronic type of bridge is usually employed. Recent bridges [3.140] allow measurements from 20 μs after the initiation of heating, resulting in a very large number of measurements within 1 s. At the same time they are characterized by a temperature resolution of 5 mK and a time resolution of 1 μs.

The transient hot-wire technique is unique when compared with other techniques of measuring thermal conductivity. The mathematical model of the technique permits a detailed assessment of its precision and verifies the absence of modes of heat transfer other than conduction. The technique has successfully been employed over a very wide range of pressures and temperatures, but not near the critical point for the reasons already discussed. Transient hot-wire instruments have been successfully operated in many laboratories (in London [3.141], Thessaloniki [3.137, 139], Lisbon [3.142], Tokyo [3.143], Boulder [3.144] and other places). In the best instruments, the uncertainty of the technique is in the region of ±0.3 to ±0.5%, although measurements performed prior to the development of the complete theory in 1976 are expected to have uncertainties larger than ±0.5%.

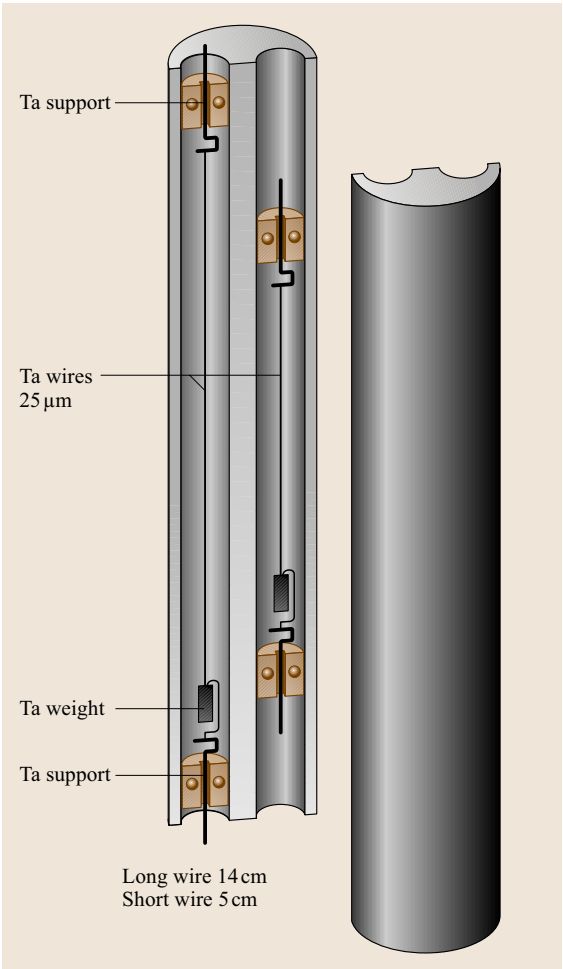

Fig. 3.42 Wires with weights arrangement developed by *Assael* et al. [3.139]

Interferometric Technique

At the critical point the thermal conductivity of the fluid diverges, its thermal conductivity becomes infinite and its thermal diffusivity becomes zero. This divergence is a consequence of the ever-increasing length scale of correlations among the molecules as the critical point is approached, and its effect extends over a wide region around the critical point. In this region a number of special techniques for the study of thermal conductivity have been developed and we describe just one that has had the distinction of having been operated on the Earth [3.145] and in space [3.146].

The principle of the technique is quite straightforward. An infinitesimally thin, uniform source of heat q is located at the junction of a two semi-infinite materials, a solid and a fluid. Initiation of the heat flux at time $t = 0$ causes the temperature of the fluid to rise according to the equation

$$\Delta T(z,t) = \frac{2q}{\lambda}\sqrt{at}\,\mathrm{ierfc}\left(\frac{z}{2}\sqrt{at}\right) , \qquad (3.131)$$

where z is the distance from the heat source ($z = 0$) measured along the normal to it into the fluid domain, and ierfc denotes the integrated complementary error function. The temperature distribution in the fluid at any instant can be determined by means of the effect of the temperature change on the density and refractive index n of the fluid using optical interferometry. In the simplest approach an interference pattern is produced in the fluid at a uniform temperature in a plane perpendicular to the heater surface by the superposition of two laser beams. Any subsequent nonuniformity of temperature induced

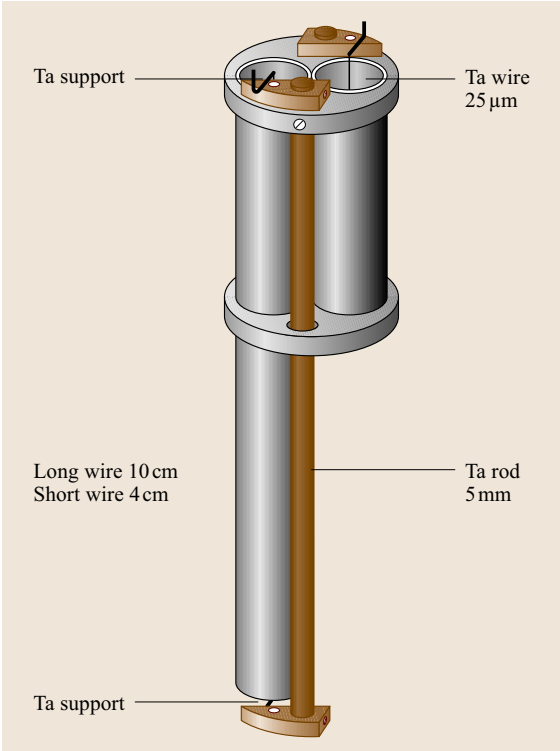

Fig. 3.43 Wires and support made of same material design developed by *Jawad* [3.147]

by the transient heating perturbs the fringe pattern in a manner described by (3.131) and $|\mathrm{d}n/\mathrm{d}T|$. Thus, in principle, measurements of the perturbation can be used to determine the thermal diffusivity of the fluid a. In the work of *Becker* and *Grigull* [3.145] this was achieved by means of holographic interferometry. The fringes in the cell (Fig. 3.44) at a state of uniform temperature are produced as a hologram and consequently subtracted from those produced in any other state, at any instant during the transient heating.

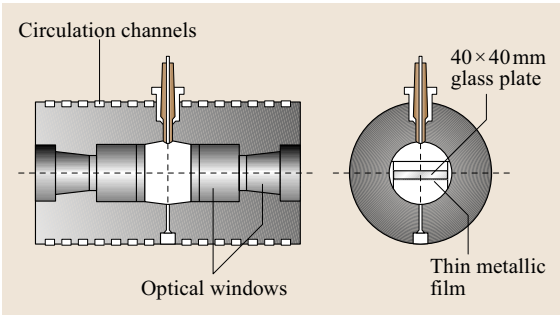

Fig. 3.44 Interferometric cell developed by *Becker* and *Grigull* [3.145]

Using the theory of ideal interferometry, in which all light paths are assumed straight, the fringe order k is given by

$$k = 2\sqrt{at}\,B\,\mathrm{ierfc}\left(\frac{z}{2}\sqrt{at}\right)\,, \tag{3.132}$$

where

$$B = \frac{ql}{\lambda\Lambda}\left|\frac{\partial n}{\partial T}\right| \tag{3.133}$$

for light of wavelength Λ, when l is the distance through the fluid over which the temperature disturbance takes place.

Thus, measurements of the position of fringes of various orders at any instant of time, following the initiation of transient heating, can be used to determine the thermal diffusivity a by nonlinear regression, and consequently the thermal conductivity from a knowledge of the fluid density and heat capacity.

The main advantage of the technique is that it is possible to employ temperature rises of the order of 10^{-4} K because the sensitivity of the technique increases as the critical point is approached. As with any measurement near the critical point a high degree of overall temperature stability and uniformity of the order of 10^{-6} K is essential and the nature of the cell required lends itself to the fulfillment of these conditions.

3.5.2 Steady-State Methods for Thermal Conductivity

In the case of the steady-state methods employed for the measurement of the thermal conductivity, (3.119) reduces to

$$\lambda\nabla^2 T = 0\,. \tag{3.134}$$

In these methods, the heat flux necessary to maintain a constant temperature difference is measured. The two surfaces are usually formed by concentric cylinders or by two parallel plates. All such instruments are characterized by quite simple working equations and the difficulties in their use arise from the painstaking alignment of the two surfaces, because defects in their alignment make a first-order contribution to the instrument's uncertainty. Attention must also be given to the avoidance of significant contributions from other modes of heat transfer such as natural convection or radiation.

Coaxial-Cylinder Technique

The coaxial-cylinder technique is a steady-state method that measures the heat exchange by conduction between two concentric cylindrical surfaces separated by a small gap filled with the fluid sample, each of these surfaces being maintained at constant temperature. The technique has an intermediate position between the transient hot-wire and parallel-plate techniques as far as the secondary heat flows are concerned. The instrumentation is somewhat more complex than that for the hot-wire cells, but less complex than that for the parallel-plate apparatus. The reduction of heat losses from non-isothermal sample boundaries is easier to realize with a system involving heat transmission between a heat source and a concentric heat sink separated by the fluid than with a planar cell. However, special care must be taken in the perfect machining of the two cylindrical surfaces, which must be highly polished. The same care must be taken in the centering of the two coaxial cylinders. The heat transfer arising from convection in the coaxial-cylinder system can be made negligible, except near the critical point of the fluid, by employing a small annular gap (typically 0.2–0.3 mm). Furthermore, the radiant heat transfer can be strongly reduced by choosing a low-emissivity material from which to make the cylinders. Silver is ideal for this purpose since it has a low emissivity, a high thermal conductivity and a good resistance to chemical agents. One of the main advantages of the coaxial-cylinder technique is its versatility. Almost any fluid can be investigated, whether an electrical conductor or not.

The basic principle of the technique assumes a thin layer of a homogeneous fluid with a uniform thermal conductivity λ enclosed between two coaxial cylinders of infinite length. The external radius of the inner cylinder is r_1, and the internal radius of the external cylinder is r_2. We assume that the heat flux is uniformly generated in the inner cylinder and propagates radially through the test sample to the heat sink (the outer cylinder), in steady-state conditions. Then, the temperatures of the external surface of the inner cylinder and of the internal surface of the outer cylinder will be respectively T_1 and T_2. Employing (3.134), the amount of heat transferred by conduction per unit time and per unit length through the fluid layer is given by

$$Q = \frac{2\pi\lambda}{\log(r_2/r_1)}(T_1 - T_2) \ . \tag{3.135}$$

The thermal conductivity is obtained from the above equation by measuring the heat flux Q passing through the test sample and the temperature difference $(T_1 - T_2)$. The value of the thermal conductivity determined corresponds to that at the average temperature $(T_1 + T_2)/2$.

In practice, the length of the cylinders is not infinite and the heat transfer through their ends must be considered.

In the classic coaxial-cylinder cell (Fig. 3.45), the end pieces (guard cylinders) are maintained at exactly same temperature as the inner cylinder emitter, so that all of the heat is transferred radially and (3.135) can be applied to obtain the thermal conductivity of the fluid.

Alternatively, if the end pieces are maintained at the same temperature as the inner surface of the outer cylinder, the thermal conductivity of the fluid is obtained from the equation

$$Q = \frac{\lambda}{C}(T_1 - T_2) \ , \tag{3.136}$$

where Q is the total amount of heat generated in the emitter and C represents a geometric instrument constant. The constant C depends just upon the geometry of the coaxial cylinders. It can therefore be determined from measurements of the heat flux when the annular gap is filled with a standard fluid of known thermal conductivity. Alternatively, it is possible to use the fact that there is a complete analogy between the equations of heat conduction and electrostatics so that a measurement of the electrical capacitance of the coaxial cylinder system when filled with a fluid of known dielectric constant also yields the constant C [3.148, 149].

In the measurement of the thermal conductivity, a number of corrections have to be made to obtain the thermal conductivity of the test specimen. Some of these corrections are related to the special features of the apparatus, for instance, the eccentricity between the internal and external cylinders; some are due to the fluid under investigation such as the heat transfer by convection. Others are related both to the instrument design and the fluid, the heat transfer by radiation including the absorption of radiation, or the temperature jumps between the walls of the cell and the test gas.

The coaxial-cylinder instrument shown in Fig. 3.45 [3.148, 149] incorporates two coaxial cylinders made completely out of silver. This instrument was used to measure several thermal conductivity of several samples, namely carbon dioxide, steam, ammonia, ethene, ethane, propane and many others [3.150] with special emphasis on the critical region. The large vertical extent of the cylinders (see dimensions in Fig. 3.45) means that the critical point can only be realized at one horizontal plane but measurements in the vicinity of the critical region

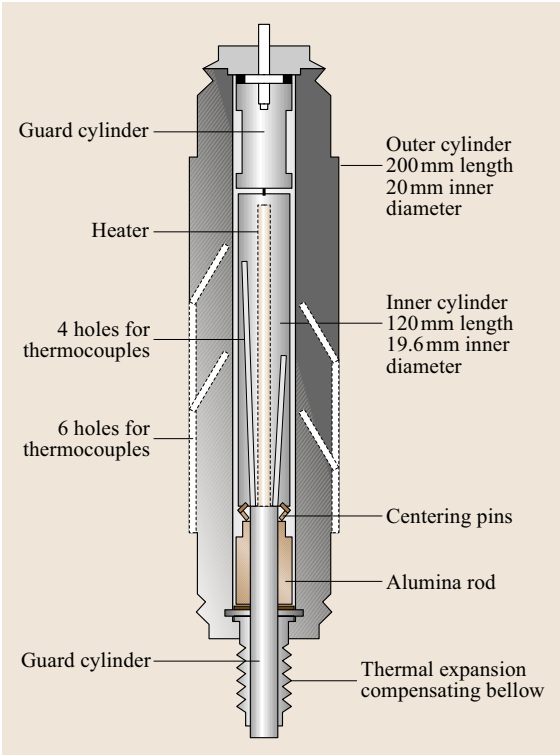

Fig. 3.45 Coaxial-cylinder cell developed by *LeNeindre* [3.148] and *Tufeu* [3.149]

were obtained successfully. The estimated uncertainty of these data is better than ±2% [3.150].

Coaxial-cylinder instruments have been successfully operated and reported in literature by many investigators, such as *Vargaftik* and *Smirnova* [3.152], *Vines* [3.153], *Ziebland* and *Burton* [3.154], *Yata* et al. [3.155], *Bailey* and *Kellner* [3.156] and others.

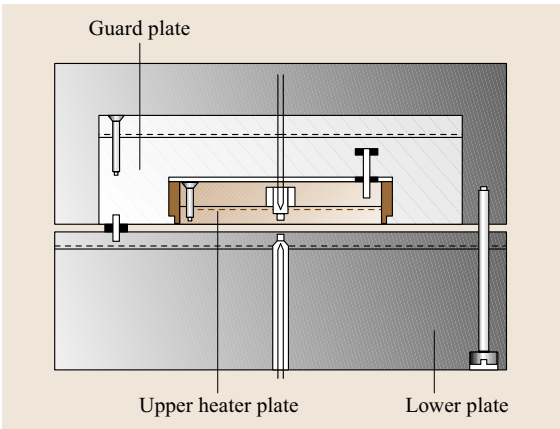

Fig. 3.46 Parallel-plate instrument (after [3.151])

Parallel-Plate Technique

In the parallel-plate technique for measuring the thermal conductivity, the fluid under investigation is confined between two horizontal plates. The system is heated from above so that the upper plate has a higher temperature than the lower plate. It follows from (3.134), that, if the upper and lower plates are maintained at constant, uniform temperatures T_1 and T_2 respectively, the heat flow across an area A and a fluid layer of thickness d, is

$$Q = \lambda A \frac{(T_1 - T_2)}{d} \,. \tag{3.137}$$

In this solution it is assumed that the thermal conductivity of the fluid is constant, that the plate dimensions are infinite and that the heat flux is in one dimension.

In practice the upper plate is surrounded by a guard plate, sufficiently close to the upper plate to eliminate the distortion of the temperature profile at the edges of the latter. Equation (3.137) shows that it is very important to measure accurately the area A and the thickness d apart from the temperature difference since they all enter the working equation in first order. The plates must also be perfectly parallel in order that the working (3.137) can be used. Since none of these conditions can ever be satisfied exactly, there are several corrections that must be considered. In practice, the guard plate is separated from the upper plate by a distance, smaller than the thickness d. Thus, A is not the area of the upper plate but an effective area for heat transfer.

Generally, the heat transfer between the plates is not only effected by conduction through the fluid layer, but also by convection and radiation. In addition, parasitic heat losses between the plates need to be taken into account. The effects of convection can be made negligibly small (although not eliminated) by taking great care to align the plates in a horizontal position and by using a small distance d. In most cases a correction is necessary for radiative heat transfer between the plates. To reduce the radiation correction the plate surfaces must have low emissivities. For this purpose the plate surfaces are polished and protected against oxidation, sometimes by coating with nickel, chrome, silver or silver dioxide. Finally, a correction has to be made for the reference state of the fluid usually taken as the average of the lower- and upper-plate temperatures. A description of all these corrections can be found in the literature [3.151, 157].

The parallel-plate instrument shown in Fig. 3.46 [3.151] was employed in the measurement of the ther-

mal conductivity of carbon dioxide in the liquid and dense gas states, with special attention to the critical region. In general, the parallel-plate technique makes it possible to perform accurate measurements of the thermal conductivity of fluids over a wide range of temperatures and pressures. The technique has successfully been employed from liquid-helium temperatures (*Ubbink* and *de Haas* [3.158], *Grenier* [3.159], *Roder* and *Diller* [3.157]) up to 500 °C (*Nuttall* and *Ginnings* [3.160], *Amirkhanov* and *Adamov* [3.161]) and at a pressure from a few mmHg up to 250 MPa (*Michels* et al. [3.162]). The classical work of *Sengers* and his coworkers [3.162] in the critical region demonstrated what can be achieved with this instrument given great care.

3.5.3 Light-Scattering Methods for Thermal Diffusivity

In the last 30 years there have been rapid developments in the application of optical techniques to the measurement of some of the transport properties of fluids. These techniques are applicable to a wide range of optically transparent fluids and have proved particularly valuable near the critical point of a fluid because, unlike the classic methods of measurement, it is not necessary to impose a macroscopic gradient on the fluid. In this section we consider two optical techniques. The bulk of our description of these techniques is associated with the underlying theory of the experiments because the physical aspects of the instrumentation are generally commercially available optical components assembled for particular purposes. First the application of photon-correlation spectroscopy to the measurement of the thermal diffusivity of fluids will be described. Secondly, a more recent optical technique that makes use of forced-Rayleigh scattering of light to determine the thermal diffusivity of fluids, such as molten salts, under extreme conditions, will be presented.

Photon-Correlation Spectroscopy Technique

A fluid in thermodynamic equilibrium is continuously subject to fluctuations of its thermodynamic variables. The fluctuations, although they are microscopic, are described statistically by the same equations that govern the corresponding macroscopic processes [3.163]. For example, the lifetime of entropy fluctuations is determined by the thermal diffusivity a of the bulk fluid. Light passing through a fluid is scattered by microscopic fluctuations of the local dielectric constant brought about by local fluctuations of the thermodynamic variables. The spectrum of the light scattered by such fluctuations has three peaks, namely the Rayleigh line and a symmetric pair of Brillouin lines. The Rayleigh line is the result of quasi-elastic scattering from fluid elements with entropy fluctuations and, in mixtures, also contains a component scattered from concentration fluctuations. Photon-correlation spectroscopy (dynamic light-scattering spectroscopy or light-beating spectroscopy), which operates in the time domain, is a high-resolution technique for measuring the widths of each of the lines of this scattered spectrum.

Use of photon-correlation spectroscopy to measure the thermal diffusivity and mass diffusion coefficient has the advantage that the measurements are made on a sample in thermal equilibrium so that no corrections for macroscopic temperature gradients are needed, and convective effects can be avoided. Because the transport information derives from sampling microscopic thermodynamic fluctuations with a laser beam, the total volume of material needed to make a measurement can be very small. Correspondingly, the time needed to reach equilibrium can be kept small, and experiment run times can also be short depending on the desired accuracy of the measurement. The technique is intrinsically absolute in nature, not requiring extensive calibration. It is, of course, particularly well suited to measurements of the thermal diffusivity in the critical region when fluctuations become more important. The major limitation of the technique has been inability to achieve a measurement uncertainty better than 5–10%, although recently [3.164] the uncertainty of the technique has improved to about 2.5%.

We now briefly examine the details of the theory of the method since they reveal what measurements may most easily be made. Incident light with wavenumber k (in the scattering medium) is scattered at an angle θ by fluctuations with a wavenumber q according to the Bragg condition

$$q = 2k \sin\left(\frac{\theta}{2}\right) . \tag{3.138}$$

The width of the scattered Rayleigh peak is determined by the diffusivities associated with thermal fluctuations in the fluid. For the entropy fluctuations this is the thermal diffusivity a whereas for the concentration fluctuations, the determining diffusivity is the mutual diffusion coefficient D. In the time domain one works with the autocorrelation function of the electric field E of the scattered light, defined by

$$G^{(1)}(\tau) = \left\langle E^*(\tau)E(0)\right\rangle . \tag{3.139}$$

In a one-component fluid $G^{(1)}(\tau)$ decays exponentially with delay time τ, as

$$G^{(1)}(\tau) = A_s \, e^{-aq^2\tau} \, , \tag{3.140}$$

where q is the wavenumber defined in (3.138), where the exponential contains the thermal diffusivity. Evidently, if it were possible to observe the autocorrelation function the thermal diffusivity could be evaluated directly. In actual photon-correlation experiments, the detectors of the scattered light are photomultiplier tubes, which respond to the intensity of the scattered light and not simply to its electric vector. Thus, when the scattered signal is processed by a digital correlator, it is the intensity correlation function

$$G^{(2)}(\tau) = \langle I(\tau) I(0) \rangle \tag{3.141}$$

that is obtained. The intensity is simply related to the electric field vector because

$$I(t) = |E(t)|^2 = E^*(t) E(t) \, , \tag{3.142}$$

in which the electric field $E(t)$ is a linear combination of all contributions to the scattered electric field at the detector. In all but the simplest of cases, the number of terms which arises from expanding (3.141) is very large. Special circumstances are employed to render the number of terms tractable.

In heterodyne measurements [3.165–167], which are most suitable for small intensities, the scattered light is mixed coherently with a static light source at the incident wavelength, usually light reflected from a window of the sample cell. In this case, the static field is added to the scattered fields at the detector, and (3.141) for a single-component fluid becomes

$$G^{(2)}(\tau) = (I_0 + I_s)^2 + I_s^2 \, e^{-2\tau/\tau_s} + 2 I_0 I_s \, e^{-\tau/\tau_s} \, , \tag{3.143}$$

where I_0 is the intensity of the static scattering, I_s is the intensity due to entropy fluctuations and τ_s is the decay time associated with the entropy fluctuations related to the thermal diffusivity a

$$a = \frac{1}{(q^2 \tau_s)} \, . \tag{3.144}$$

Fitting the heterodyne equations to extract the decay time τ_s, it is usual to arrange the condition $I_0 \gg I_s$ so that (3.143) simplifies to

$$G^{(2)}(\tau) = (I_0 + I_s)^2 + 2 I_0 I_s \, e^{-\tau/\tau_s} \, . \tag{3.145}$$

Equation (3.145) forms the basis of the usual photon-correlation spectrometer measurements.

A typical arrangement is shown in Fig. 3.47. The heterodyne arrangement is ensured by using a strong reference beam generated by a beam splitter which is then combined with the Rayleigh-scattered light at the photomultiplier. Here, q is obtained from the equation [3.164]

$$q = \frac{4\pi n}{\lambda_0} \sin\left(\frac{\theta_s}{2}\right) \, , \tag{3.146}$$

where n is the sample refractive index, λ_0 the laser wavelength in vacuum, and θ_s the angle between the direction of observation and the incident laser beam within the sample (Fig. 3.47). With these values taken from experiment, and with the decay time extracted from the measured correlation function, the thermal diffusivity a can be calculated from (3.144).

Recent publications [3.164] on the measurement of the thermal conductivity of toluene with a photon-correlation spectrometer showed an uncertainty of $\pm 2.5\%$, mostly attributed to errors in the angle measurement and the photon statistics, which can be improved by greater duration of the experiments.

Forced Rayleigh-Scattering Technique

The forced Rayleigh-scattering technique was initiated independently by *Eichler* et al. [3.168] and *Pohl* et al. [3.169] in 1973. *Eichler* and coworkers developed it for the determination of the thermal diffusivity of organic liquids and ruby crystals. More recently *Nagasaka* and *Nagashima* and their coworkers [3.170, 171] reworked the theory of forced Rayleigh scattering and applied it to the measurement of the thermal diffusivity of organic liquids, liquid crystals and, particularly, high-temperature molten salts (above 1000 °C).

The term *forced Rayleigh scattering* was created by analogy with spontaneous Rayleigh scattering, which we saw above is based on the scattering effect of statistical thermodynamic fluctuations in a fluid. If such weak and random fluctuations are replaced by stronger and more coherent excitations from a laser-induced grating, the forced scattering (or diffraction) of a probing beam becomes much stronger and coherent. The technique has also been called *laser-induced dynamic grating*.

The principle of the forced Rayleigh scattering method, is illustrated by reference to Fig. 3.48.

Two pulsed, high-power laser beams of equal wavelength and equal intensity intersect in an absorbing sample at an angle θ. They generate an optical interference fringe pattern whose intensity distribution is spatially sinusoidal. Following partial absorption of the laser light, this interference pattern induces a corresponding temperature distribution in the x-direction

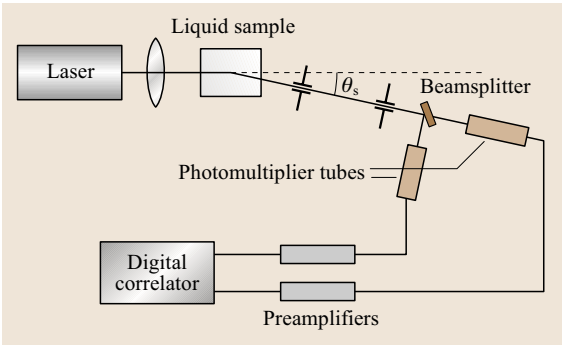

Fig. 3.47 Schematic diagram of a photon-correlation spectrometer

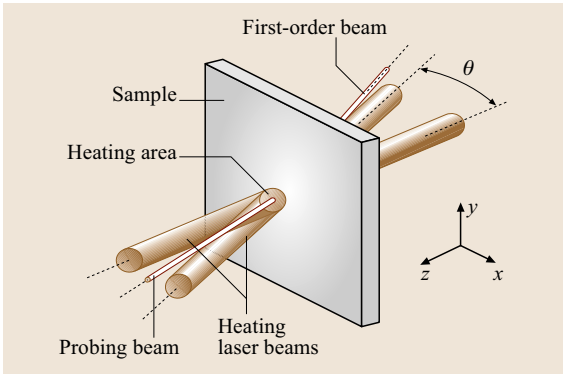

Fig. 3.48 Principle of forced Rayleigh scattering

of the sample. After the heating process, the excited temperature distribution decays exponentially owing to heat conduction and the decay of the distribution can be examined by using a non-absorbed probe-laser beam which is diffracted by the grating created by the influence of the temperature distribution on the refractive index of the fluid. It is assumed that heat conduction takes place in the x-direction only and this is permissible if the following conditions are satisfied. First the grating period Λ should be much smaller than the sample thickness d. Secondly, Λ should be sufficiently small compared with the light absorption length and finally Λ should be small compared with the diameter of the heated area. The simplest mathematical description of forced Rayleigh scattering is then provided by rewriting the thermal balance equation (3.119) in one dimension as

$$\frac{\partial T}{\partial t} = a\frac{\partial^2 T}{\partial x^2} \tag{3.147}$$

subject to the initial spatially periodic temperature distribution produced by the interference of two laser beams.

$$T = T_0 + \Delta T_0(1+\cos qx) \quad \text{at } t = 0\,. \tag{3.148}$$

Here, T is the temperature, t the elapsed time after heating, a the thermal diffusivity of the sample, T_0 the initial temperature, ΔT_0 the initial spatial temperature amplitude, and $q = 2\pi/\Lambda$ is the wavenumber of the interference pattern. The relation between the angle of inclination of the heating beams and the grating period is

$$\Lambda = \frac{\lambda_h}{2\sin(\theta/2)} \approx \frac{\lambda_h}{\theta} \quad (\theta \approx 0)\,, \tag{3.149}$$

where λ_h is the wavelength of the heating beam. The solution to (3.147) for the temperature distribution is

$$T(x,t) = T_0 + \Delta T_0\left[1+\cos(qx)\exp\left(\frac{-t}{\tau}\right)\right], \tag{3.150}$$

which demonstrates that the spatial temperature amplitude decays exponentially with the relaxation time characteristic of heat conduction τ

$$\tau = \left(\frac{1}{a}\right)\left(\frac{\Lambda}{2\pi}\right)^2\,. \tag{3.151}$$

As indicated earlier, the spatially periodic temperature distribution produces a corresponding refractive-index distribution. In turn this acts as an optical phase grating for a low-power probing laser beam of a wavelength λ_p not absorbed in the sample. According to the theory of diffraction, if the sample is thin enough, the first-order diffracted laser beam intensity I_1 is proportional to the square of the maximum phase variation of the grating ϕ so that for a probing laser beam of intensity I_p

$$I_1 = \frac{I_p\phi^2}{4}\,. \tag{3.152}$$

Table 3.17 Reference values for the thermal conductivity of noble gases at a pressure of 0.1 MPa

	Thermal conductivity ($\mathrm{mWm^{-1}K^{-1}}$)				
T (°C)	Helium	Neon	Argon	Krypton	Xenon
25	155.3	49.24	17.67	9.451	5.482
100	181.1	57.84	21.36	11.63	6.852
200	213.9	67.43	25.59	14.18	8.534
300	244.7	76.79	29.60	16.50	10.07
400	274.1	85.34	33.14	18.64	11.49
500	302.0	93.39	36.50	20.64	12.81

Table 3.18 Thermal conductivity λ ($mW\,m^{-1}K^{-1}$) of some *n*-alkanes in the liquid phase

		P (MPa)	273.15 K	298.15 K	323.15 K	348.15 K	373.15 K
n-Pentane	C_5H_{12}	0.101	125.1	113.7	102.4	91.3	80.5
		5	127.8	116.8	105.9	95.3	84.6
		10	130.4	119.7	109.2	98.8	88.3
		25	137.6	127.6	117.8	107.9	97.3
		50	147.8	138.6	129.4	119.7	108.8
n-Hexane	C_6H_{14}	0.101	128.4	118.9	109.8	100.9	92.1
		5	130.7	121.5	112.8	104.4	96.1
		10	133.0	124.1	115.7	107.6	99.6
		25	139.3	131.0	123.3	116.0	108.7
		50	148.4	140.9	134.0	127.4	120.6
n-Heptane	C_7H_{16}	0.101	132.8	123.5	114.5	105.9	97.4
		5	134.9	125.8	117.2	108.9	100.9
		10	137.0	128.2	119.8	111.8	104.1
		25	142.9	134.5	126.8	119.4	112.4
		50	151.4	143.7	136.6	130.0	123.5
n-Octane	C_8H_{18}	0.101	137.8	128.4	119.5	110.8	102.4
		5	139.8	130.7	122.0	113.6	105.5
		10	141.8	132.9	124.4	116.3	108.5
		25	147.4	139.0	131.0	123.6	116.4
		50	155.7	147.8	140.5	133.7	127.1
n-Nonane	C_9H_{20}	0.101	140.1	130.9	122.1	113.5	105.1
		5	142.1	133.1	124.4	116.1	108.0
		10	144.0	135.1	126.7	118.6	110.8
		25	149.3	140.9	132.9	125.3	118.1
		50	157.3	149.4	142.0	135.0	128.3
n-Decane	$C_{10}H_{22}$	0.101	143.5	134.2	125.3	116.6	108.3
		5	145.4	136.3	127.5	119.1	111.0
		10	147.2	138.3	129.7	121.5	113.6
		25	152.5	143.9	135.7	128.0	120.7
		50	160.4	152.2	144.5	137.4	130.6
n-Undecane	$C_{11}H_{24}$	0.101	145.0	135.9	127.0	118.3	110.0
		5	146.8	137.8	129.1	120.7	112.5
		10	148.6	139.8	131.2	123.0	115.0
		25	153.7	145.2	137.0	129.2	121.7
		50	161.4	153.3	145.5	138.2	131.2
n-Dodecane	$C_{12}H_{26}$	0.101	147.9	138.6	129.5	120.7	112.2
		5	149.7	140.5	131.6	123.0	114.7
		10	151.5	142.4	133.6	125.2	117.1
		25	156.5	147.7	139.3	131.2	123.5
		50	164.1	155.7	147.6	140.0	132.8

The interrelation between ϕ and the maximum temperature amplitude of (3.150) can be expressed by

$$\phi = \left(\frac{2\pi d}{\lambda_p}\right)\left(\frac{\partial n}{\partial T}\right)\Delta T_0 \exp\left(\frac{-t}{\tau}\right), \qquad (3.153)$$

where n is the refractive index of the sample. Substituting (3.153) into (3.152), the thermal diffusivity of the sample can be obtained from the following equation

$$a = -\left(\frac{1}{2}\right)\left(\frac{\Lambda}{2\pi}\right)^2\left(\frac{\mathrm{d}\log I_1}{\mathrm{d}t}\right). \qquad (3.154)$$

Table 3.19 Thermal conductivity λ ($mW\,m^{-1}K^{-1}$) of some alkenes in the liquid phase

		P (MPa)	273.15 K	298.15 K	323.15 K	348.15 K	373.15 K
Benzene	C_6H_6	0.101	153.1	143.7	134.0	124.1	114.2
		5	154.9	145.6	136.1	126.5	116.9
		10	156.6	147.5	138.2	128.8	119.4
		25	161.5	152.9	144.1	135.2	126.4
		50	169.0	160.9	152.7	144.5	136.2
Toluene	C_7H_8	0.101	138.5	130.0	121.9	114.4	107.2
		5	139.9	131.6	123.8	116.4	109.6
		10	141.4	133.3	125.6	118.4	111.8
		25	145.7	137.9	130.6	124.0	118.0
		50	152.1	144.8	138.1	132.0	126.7
Ethylbenzene	C_8H_{10}	0.101	135.6	128.6	121.7	115.1	108.6
		5	137.0	130.2	123.5	117.1	110.9
		10	138.4	131.7	125.3	119.1	113.2
		25	142.5	136.1	130.1	124.5	119.2
		50	148.6	142.8	137.4	132.4	127.9
o-Xylene	C_8H_{10}	0.101	142.1	134.6	127.6	121.2	115.3
		5	143.5	136.0	129.2	123.0	117.4
		10	144.8	137.5	130.8	124.8	119.4
		25	148.7	141.7	135.4	129.7	124.8
		50	154.6	148.0	142.2	137.1	132.8
m-Xylene	C_8H_{10}	0.101	133.9	127.5	121.2	115.0	108.9
		5	135.3	129.1	123.0	117.0	111.2
		10	136.7	130.6	124.7	118.9	113.4
		25	140.7	135.0	129.6	124.4	119.5
		50	146.8	141.6	136.8	132.3	128.2
p-Xylene	C_8H_{10}	0.101	132.2	125.7	119.4	113.1	107.0
		5	133.6	127.3	121.1	115.1	109.3
		10	135.0	128.8	122.8	117.0	111.5
		25	138.9	133.1	127.6	122.4	117.5
		50	144.9	139.7	134.7	130.2	126.0
Mesitylene	C_9H_{12}	0.101	135.6	129.1	122.9	117.1	111.5
		5	136.9	130.6	124.6	119.0	113.7
		10	138.2	132.1	126.2	120.8	115.8
		25	142.1	136.3	130.9	126.0	121.6
		50	148.0	142.6	137.8	133.5	129.9

Accordingly, the thermal diffusivity is determined by measuring the time dependence of I_1 and the grating period Λ. The optical instrumentation required to carry through these measurements is standard and does not merit description here.

The actual experimental conditions may differ from those described. There are several secondary effects that must be considered, for example in many fluids it is necessary to add a dye to the fluid so that it absorbs sufficient light and this may affect the property measured. It is also necessary to consider the fact that the heat conduction process is not in practice one-dimensional; these and other effects have been dealt with in the literature [3.172]. By comparison with conventional techniques for the measurement of the thermal diffusivity, the forced Rayleigh technique has several following advantages: it is contact-free, it is characterized by the short duration of the measurement time (< 1 ms), small temperature rise (< 0.1 K), small sample volume ($< 10\,mm^3$), and it is applicable to anisotropic

Table 3.20 Thermal conductivity λ ($mW\,m^{-1}K^{-1}$) of some *n*-alcohols in the liquid phase

		P (MPa)	273.15 K	298.15 K	323.15 K	348.15 K	373.15 K
Methanol	CH_4O	0.101	206.1	203.8	192.5	176.2	158.2
		5	208.7	206.9	195.9	179.5	161.2
		10	211.3	210.0	199.1	182.8	164.0
		25	218.5	218.4	208.2	191.6	171.8
		50	229.2	230.7	221.1	204.1	182.6
Ethanol	C_2H_6O	0.101	174.9	166.7	156.5	145.0	132.6
		5	177.0	169.0	159.0	147.5	135.0
		10	179.1	171.3	161.5	150.0	137.3
		25	185.0	177.8	168.3	156.8	143.6
		50	193.8	187.4	178.3	166.7	152.7
1-Propanol	C_3H_8O	0.101	159.1	156.1	150.2	141.5	130.5
		5	160.9	158.2	152.5	144.1	133.1
		10	162.8	160.3	154.9	146.6	135.5
		25	167.9	166.2	161.4	153.4	142.2
		50	175.7	175.0	171.0	163.3	151.9
1-Butanol	$C_4H_{10}O$	0.101	159.3	155.0	147.0	135.9	122.5
1-Pentanol	$C_5H_{12}O$	0.101	163.5	155.1	143.1	128.6	112.8
1-Hexanol	$C_6H_{14}O$	0.101	167.5	154.5	139.1	122.5	106.0

materials. The technique has successfully been applied to the measurement of the thermal diffusivity of molten salts [3.173] although its potential is greater.

3.5.4 Thermal Conductivity Reference Values

Toluene and water have been proposed as primary standard reference liquids. Under the auspices of the International Union of Pure and Applied Chemistry (IUPAC) Subcommittee on Transport Properties, *Nieto de Castro* et al. [3.174] recommended the following values as primary data:

for toluene at 298.15 K and 0.1 MPa

$$\lambda = (0.1311 \pm 0.0013)\,\mathrm{W m^{-1}\,K^{-1}} \qquad (3.155)$$

and for water at 298.15 K and 0.1 MPa

$$\lambda = (0.6067 \pm 0.0061)\,\mathrm{W m^{-1}\,K^{-1}}\,. \qquad (3.156)$$

The temperature dependence of the thermal conductivity is represented by the following equations, where $T^* = (T/298.15\,\mathrm{K})$, and $\lambda^* = [\lambda(T)/\lambda(298.15\,\mathrm{K})]$:

for toluene

$$\lambda^* = 1.68182 - 0.682022T^* \qquad (3.157)$$

at $230\,\mathrm{K} \le T \le 360\,\mathrm{K}$,

$$\lambda^* = 1.45210 - 0.224229T^* - 0.225873T^{*2} \qquad (3.158)$$

at $189\,\mathrm{K} \le T \le 360\,\mathrm{K}$,
for water

$$\lambda^* = -1.26523 + 3.70483T^* - 1.43955T^{*2} \qquad (3.159)$$

for $274\,\mathrm{K} \le T \le 360\,\mathrm{K}$.

The maximum deviation of the primary experimental data from (3.157) is 1.3%, from (3.158) is 1.5% and from (3.159) is 1.1%. Other secondary thermal conductivity reference liquids are available in the literature [3.167].

Recommended values for the thermal conductivity of the noble gases are shown in Table 3.17. They have been calculated using available theory and the corresponding viscosity data and their estimated uncertainty is ±0.3% in the range 25–200 °C, and ±0.5% in the range 200–500 °C.

For higher pressures up to 30 MPa and at a temperature of 27.5 °C, the thermal conductivity of argon is represented by the equation [3.175]

$$\lambda = 17.751 + 21.402\times10^{-3}\rho + 27.247\times10^{-6}\rho^2\,, \qquad (3.160)$$

Table 3.21 Thermal conductivity λ ($mW\,m^{-1}K^{-1}$) of some refrigerants in the liquid phase

		P (MPa)	248.15 K	273.15 K	298.15 K	323.15 K	348.15 K
R22	$CHClF_2$	5	111.6	98.8	86.8	76.2	65.8
		10	114.2	102.0	90.9	81.7	74.7
		25	120.8	110.1	100.5	93.3	89.8
R32	CH_2F_2	5	171.8	147.7	127.4	112.0	
		10	176.8	153.3	134.0	121.2	129.0
		25	189.7	166.7	148.6	137.9	165.6
R124	C_2HClF_4	5	87.5	78.9	70.5	63.6	57.6
		10	88.7	80.9	73.5	67.9	62.8
		25	92.2	86.0	81.0	77.5	73.3
R125	C_2HF_5	5	81.7	75.2	66.6	55.6	
		10	84.4	78.9	71.7	63.4	
		25	91.3	87.6	82.4	76.6	
R134a	$C_2H_2F_4$	5	104.9	94.6	84.6	74.1	62.3
		10	107.6	97.8	88.6	79.3	69.9
		25	114.8	105.9	98.0	90.6	83.8
R141b	$C_2H_3ClF_2$	5	108.5	101.1	93.6	86.0	78.2
		10	109.5	102.5	95.5	88.3	81.1
		25	112.4	106.5	100.6	94.4	88.2
R152a	$C_2H_4F_2$	5	127.8	116.8	106.1	94.6	81.3
		10	130.7	120.3	110.4	100.3	89.3
		25	138.2	129.0	120.9	113.0	104.9

where λ is measured in mW/(m K) and ρ in kg/m^3. Other secondary thermal conductivity reference fluids are available in the literature [3.167].

3.5.5 Tables of Thermal Conductivity Values

In Tables 3.18–3.22, the thermal conductivity of commonly encountered fluids is given for engineering purposes as a function of temperature and pressure. The fluids and the temperature and pressure conditions chosen are the same for the density and viscosity in Sects. 3.1 and 3.4.

Values for the liquid thermal conductivity are based on a large collection of experimental data correlated by a semi-empirical hard-spheres-based procedure available in the literature (*n*-alkanes [3.176], *n*-alkenes [3.177], *n*-alcohols [3.178], refrigerants [3.179]). The uncertainty of the quoted liquid thermal conductivity values is much better than ±5%. Values for the gas-phase thermal conductivity have been obtained from corresponding-states software [3.37] based on experimental data and they have an estimated uncertainty better than 2%. It is important to stress that the values listed for individual materials are not intended to be the best known values; they are, rather, a set of values that are consistent with those listed for other properties with sufficient accuracy to be useful.

3.6 Diffusion

The diffusion processes in liquids and gases are characterized by vastly different time scales; the process in liquids being some 10^5 times slower than in low-density gases. As a result, the types of instruments used to measure the diffusion coefficient differ dramatically between the two phases. We describe just some of the most successful among the many techniques that have been used in each phase concentrating upon optical techniques for liquids. We consider also two classical techniques for the gas phase. Just one technique is common to both gas and liquid phases, that relying upon the phenomena of Taylor dispersion.

The diffusion coefficient of a mixture of two or more chemical species is a measure of its tendency to produce

Table 3.22 Thermal conductivity λ ($mW\,m^{-1}K^{-1}$) of some gases

		P (MPa)	273.15 K	298.15 K	323.15 K	348.15 K	373.15 K
Argon	Ar	0.101	16.64	17.79	18.89	19.95	20.98
		5	19.47	20.34	21.21	22.08	22.95
		10	22.68	23.13	23.69	24.32	25.00
Hydrogen	H_2	0.101	172.46	183.61	194.36	204.70	214.80
		5	177.70	188.50	198.80	208.90	218.80
		10	182.00	193.20	203.20	213.05	222.60
Nitrogen	N_2	0.101	24.90	26.58	28.21	29.80	31.34
		5	28.25	29.60	32.34	32.34	33.70
		10	31.84	32.76	33.80	34.92	36.07
Oxygen	O_2	0.101	25.54	27.52	29.46	31.36	33.23
		5	28.83	30.49	32.16	33.84	35.52
		10	32.57	33.74	35.05	36.44	37.90
Carbon monoxide	CO	0.101	24.89	26.71	28.48	30.20	31.89
		5	28.43	29.89	31.38	32.87	34.36
		10	32.28	33.26	34.39	35.50	36.87
Carbon dioxide	CO_2	0.101	16.25	18.09	19.94	21.80	23.65
		5		26.30	25.96	26.76	27.93
		10			55.01	37.48	34.66
Sulfur dioxide	SO_2	0.101	9.84	11.00	12.20	13.43	14.68
Hydrogen sulfide	H_2S	0.101	16.39	18.08	19.81	21.55	
		5				29.22	
Methane	CH_4	0.101	32.75	36.08	39.51	43.04	46.68
		5	38.90	41.46	44.34	47.44	50.74
		10	47.69	48.26	50.06	52.44	55.21
Ethane	C_2H_6	0.101	19.65	22.55	25.62	28.86	32.26
		5			38.31	36.89	38.49
		10			75.26	61.66	52.42
Propane	C_3H_8	0.101	15.49	18.03	20.75	23.62	

entropy when it is disturbed from equilibrium by the imposition of gradient of the chemical potential of each species. As for the other transport coefficients, the diffusion coefficient is defined as the proportionality constant between a flux and a driving force. However, unlike the other transport processes, the diffusive flux of molecules has been defined with respect to a number of different frames of reference, and the driving force has also been expressed in a variety of alternative ways. There are therefore a variety of different diffusion coefficients in use. In this work, we choose the definition that leads to a phenomenological equation most closely related to the equation which describes the diffusion process in an experiment. We also confine ourselves to binary systems for simplicity. Consequently, we employ the gradient of molar density of a species for the driving force and consider molar fluxes of the two species, J_1 and J_2, with respect to a volume-fixed frame of reference defined by

$$v_1 J_1 + v_2 J_2 = 0\,, \tag{3.161}$$

where v_1 and v_2 are the partial molar volumes of the components of the mixture. Fick's law gives the molar fluxes, at any instant relative to this frame of reference as

$$J_1 = -D_{12}\left(\frac{\partial C_1}{\partial x}\right)_t\,, \tag{3.162}$$

$$J_2 = -D_{21}\left(\frac{\partial C_2}{\partial x}\right)_t\,, \tag{3.163}$$

where C_1 and C_2 are the molar densities of the two components. The coefficients D_{12} and D_{21} are the diffusion

coefficients for the mixture, and from the definition

$$v_1 C_1 + v_2 C_2 = 1 \,, \tag{3.164}$$

it follows that

$$D_{12} = D_{21} \,. \tag{3.165}$$

When $(\partial C_i/\partial x)_t$ changes with time, but the diffusion coefficient does not vary with concentration during the experiment, then

$$\frac{\partial C_i}{\partial t} = D_{12}\left(\frac{\partial^2 C_i}{\partial x^2}\right) \,, \quad i = 1, 2 \,. \tag{3.166}$$

The diffusion coefficient defined in this way is known also as the interdiffusion coefficient or mutual diffusion coefficient, and depends parametrically on the thermodynamic state of the fluid, which is characterized by the variables (T, P, C_i) or (T, ρ, C_i). In this section it will be referred to simply as the *diffusion coefficient*.

The diffusion coefficient, as defined above, must be distinguished from

1. the self-diffusion coefficient that refers to the diffusional motion in a single-component fluid, and is usually studied by techniques such as nuclear magnetic resonance, and
2. the intra-diffusion coefficient, or tracer diffusion coefficient, which characterizes the diffusion of each of the components i, j in an otherwise uniform mixture of two or more components where the component under study, i, is chemically identical with component j but can be distinguished by some label such as its isotopic form.

The work presented here is divided into two main sections: the first dealing with measurements in the liquid phase, and the second with measurements in the gas phase because for this property there are some substantial differences in techniques between the two phases.

3.6.1 Diffusion in Liquids

In this section, techniques that are able to yield measurements of the diffusion coefficients in liquids with a small uncertainty on a reasonable timescale (≤ 1 d), will be discussed. Thus, the methods which will be presented are the Diaphragm-cell technique, the Taylor-dispersion technique, and the Rayleigh and Gouy interferometric techniques. Other techniques can yield higher accuracy but take extreme precautions or a larger investment of time than can be justified for routine use.

Diaphragm-Cell Technique

The diaphragm cell is the simplest method of determining diffusion coefficients with an uncertainty of about 1%. It is very versatile and has been used for a wide range of temperatures and pressures. The essential features of a typical cell, of the type first employed by *Stokes* [3.180], are shown in Fig. 3.49. Each bulb contains a glass stirrer, always in contact with the glass diaphragm. The stirrers are rotated by means of external rotating magnets. For a measurement, of the diffusion coefficient of potassium chloride in aqueous solution, for example, the salt solution is placed in the bottom bulb and water in the top. After a certain period, samples are taken from both bulbs for analysis.

In the case of the diaphragm cell, the diffusion process is assumed to be one-dimensional but the characteristics of the diaphragm are not known so that application of (3.166) and its solution are heuristic. If an analysis of the compositions of the two samples in the top and bottom bulbs is conducted after a diffusion time t then the diffusion coefficient D_{12} is obtained from the set of equations [3.181, 182]

$$D_{12} = \left(\frac{1}{\beta t}\right) \log\left[\frac{(C_\mathrm{B}^0 - C_\mathrm{T}^0)\,(1-\lambda/6)}{(C_\mathrm{B} - C_\mathrm{T})}\right] \,, \tag{3.167}$$

with

$$\beta = \left(\frac{A}{l}\right)\left(\frac{1}{V_\mathrm{B}} + \frac{1}{V_\mathrm{T}}\right)\left(1 - \frac{\lambda}{6}\right) \,, \tag{3.168}$$

and

$$\lambda = \frac{2V_\mathrm{D}}{(V_\mathrm{B} + V_\mathrm{T})} \,. \tag{3.169}$$

Here, the subscripts 'B' and 'T' denote the bottom and top compartments, while the superscript 0 denotes initial concentrations. A is the effective area of the membrane, l its effective length and V_D the liquid content in the membrane (note that A and l are not simply related, as the effective area of the membrane could be the same for a whole range of membranes while their length could be increased). Excellent measurements with this technique were carried out by *Woolf* and *Tilley* [3.183] on aqueous solutions of potassium chloride.

Taylor-Dispersion Technique

The Taylor-dispersion technique originated by Sir Geoffrey *Taylor* in 1953 [3.184], provides a means whereby

rapid measurements of diffusion coefficients can be made with moderate accuracy over a wide range of conditions. The method is a dynamic chromatographic technique that has few of the limitations of the other techniques of measuring diffusion coefficients.

In an idealized Taylor-dispersion experiment a narrow pulse of solute is injected near the axis into a long uniform tube of length L and radius R, in which solvent is flowing in a slow, laminar manner. As the pulse is carried through the tube, it spreads owing to the combined action of convection in the axial direction and molecular diffusion in the radial direction. The peak center, or the maximum, continues to move at the mean velocity of the laminar profile. Eventually, the peak elutes from the end of the long tube, where a suitable detector is employed to measure the radially averaged concentration profile as a function of time.

In cylindrical coordinates, the continuity equation for a species in terms of its molar concentration C, at fixed point (r, x) is written

$$D_{12}\left(\frac{\partial^2 C}{\partial r^2}+\frac{1}{r}\frac{\partial C}{\partial r}+\frac{\partial^2 C}{\partial x^2}\right)=u(r)\frac{\partial C}{\partial x}+\frac{\partial C}{\partial t}\,, \tag{3.170}$$

where $u(r)$ is the axial velocity of the flow relative to laboratory coordinates. The diffusion coefficient is assumed constant which is valid if the concentration gradient is small. It is further assumed that there is no chemical reaction occurring, the fluid density is constant, and that the fluid is in laminar flow with the familiar parabolic velocity profile for Newtonian fluids,

$$u(r)=2\overline{u}\left[1-\left(\frac{r}{R}\right)^2\right]\,, \tag{3.171}$$

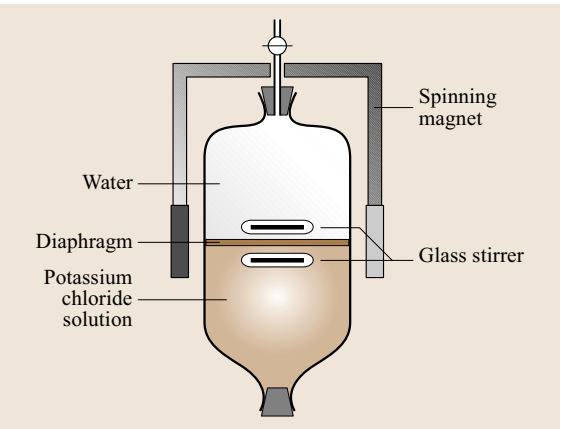

Fig. 3.49 Diaphragm cell (after [3.180])

where $\overline{u}$ is the mean flow velocity. It is, however, more convenient to measure the concentration distribution relative to an axial coordinate z, which moves with the mean speed of flow $\overline{u}$. Then the velocity in this frame of reference is

$$v(r)=u(r)-\overline{u}=\overline{u}\left[1-2\left(\frac{r}{R}\right)^2\right]\,. \tag{3.172}$$

Taylor showed that, by choosing appropriate experimental conditions, the effects of longitudinal diffusion upon the injected pulse may be neglected [3.185]. Therefore, neglecting the axial dispersion term and considering convection across a plane which moves at $\overline{u}$, (3.167) reduces to

$$\frac{\partial^2 C}{\partial r^2}+\frac{1}{r}\frac{\partial C}{\partial r}=\frac{R^2}{D_{12}}\frac{\partial C}{\partial t}+\frac{R^2\overline{u}}{D_{12}}\left[1-2\left(\frac{r}{R}\right)^2\right]\frac{\partial C}{\partial z}\,, \tag{3.173}$$

where $z=x-\overline{u}t$. Although (3.173) cannot be solved directly for the concentration perturbation, it is readily solved for the spatial moments of the distribution C at a particular time. In particular, *Aris* [3.186] has shown that, after a sufficient time, the concentration perturbation averaged over a cross section of the tube has a Gaussian distribution along the length of the tube. The variance of the distribution is related to the dimensions of the tube, the velocity of the flow, and the diffusion coefficient of the fluid mixture. Indeed, this result formed the basis of Taylor's original measurements of diffusion coefficients.

It is experimentally more convenient to monitor the cross-section-averaged concentration distribution at an axial position $z=L$ as a function of time [3.187, 188]. In this case, the first moment of the temporal distribution $\overline{t}_{\mathrm{id}}$ is given by [3.187]

$$\overline{t}_{\mathrm{id}}=\frac{L}{\overline{u}}\,(1+2\zeta)\,, \tag{3.174}$$

whereas the variance of the temporal distribution, which is no longer Gaussian, is [3.187]

$$\sigma^2_{\mathrm{id}}=\left(\frac{L}{\overline{u}}\right)^2\left(8\zeta^2+2\zeta\right)\,, \tag{3.175}$$

where

$$\zeta=\frac{\overline{u}R^2}{48D_{12}L}\,, \tag{3.176}$$

and the subscript 'id' denotes the ideal experimental arrangement. These equations lead to a final working equation for the evaluation of the diffusion coefficient

from the measured temporal moments of the distribution in the form [3.187]

$$D_{12} = \frac{R^2}{24\bar{t}_{id}} \frac{\left(1+\frac{4\sigma_{id}^2}{\bar{t}_{id}^2}\right)^{1/2}+3}{\left(1+\frac{4\sigma_{id}^2}{\bar{t}_{id}^2}\right)^{1/2}+\frac{2\sigma_{id}^2}{\bar{t}_{id}^2}-1} . \quad (3.177)$$

The principle of Taylor dispersion was first applied to the measurement of diffusion coefficients in gases by *Giddings* et al. [3.189]. However, the uncertainty of the measurements was very large. The development of very sensitive refractive-index detectors for liquid chromatography encouraged the development of the method, for use in liquids by *Ouano* [3.190] and *Wakeham* et al. [3.191,192]. Figure 3.50 shows the instrument employed by *Alizadeh* and *Wakeham* [3.187,188] for their measurements of the diffusion coefficients of *n*-alkanes in the temperature range 20–80 °C. They showed that diffusion coefficients with an uncertainty of ±1% may be obtained in an experiment lasting only one hour.

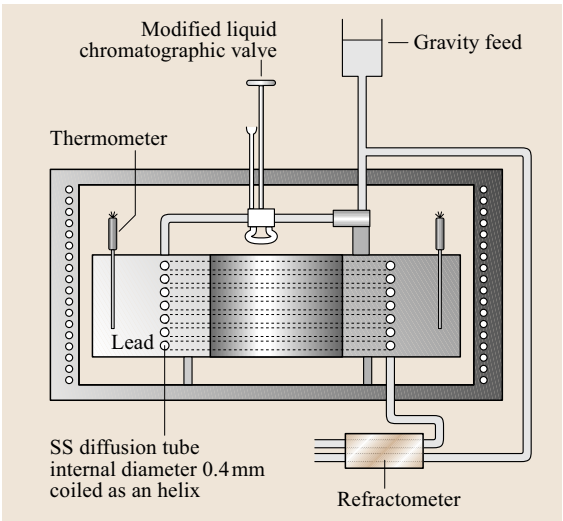

Fig. 3.50 Schematic diagram of a Taylor-dispersion instrument employed for diffusion coefficient measurements in liquids developed by *Alizadeh* et al. [3.187] and *Wakeham* [3.188]

Rayleigh Interferometric Technique

The most precise methods for measuring interdiffusion coefficient in two- or three-component liquid systems have been the Rayleigh and Gouy optical interferometric methods. Both have been employed to obtain values of binary diffusion coefficients with a typical uncertainty of about 0.2% and a precision of 0.1–0.2%. There are many possible practical arrangements that can be used in experiments, but most workers have chosen the *free-diffusion* case described below. Whatever arrangement is adopted the process of diffusion produces a time-dependent distribution of refractive index or refractive index gradient in the mixing fluid that enables the diffusion process to be followed.

Free diffusion in a vertical column starts from an infinite sharp boundary between two uniform solutions of two species of different concentrations. The free-diffusion experiment is stopped before concentration changes are observed at the top or bottom of the cell [3.193]. The initial concentrations of the two solutions are normally chosen to be only slightly different so that the diffusion coefficient can be taken as a constant. In such a case, the closed-form solutions of the diffusion equation given below can be used. The diffusion (3.166), in a binary system with a constant diffusion coefficient, can be rewritten for one solute as

$$\frac{\partial C}{\partial t} = D_{12}\left(\frac{\partial^2 C}{\partial Z^2}\right) . \quad (3.178)$$

Here C is the molar concentration, t the time elapsed from the start of the experiment, and Z the vertical distance from the starting boundary (positive in the direction of higher density and, usually, higher concentration). The solution to this equation for free diffusion is

$$C = \overline{C} + \frac{\Delta C}{2}\mathrm{erf}\left(\frac{y}{\sqrt{D}}\right) , \quad (3.179)$$

where

$$y = \frac{Z}{2\sqrt{t}} , \quad (3.180)$$

$$\overline{C} = \frac{C_T + C_B}{2} , \quad (3.181)$$

and

$$\Delta C = C_B - C_T . \quad (3.182)$$

In the above equations the subscripts 'B' and 'T' refer to the initial bottom and top solutions, respectively.

In the usual case, the refractive index n can be described by a linear function of the solute concentration

$$n = \overline{n} + R(C - \overline{C}) , \quad (3.183)$$

so that for free diffusion in a binary system

$$n = \overline{n} + \frac{\Delta n}{2}\mathrm{erf}\left(\frac{y}{\sqrt{D_{12}}}\right) , \quad (3.184)$$

where Δn is the difference of refractive index of the top and bottom solutions initially. This distribution of refractive index can be revealed by Rayleigh interferometry.

A schematic view of a Rayleigh interferometer for the measurement of the diffusion coefficient in liquids [3.194] is shown in Fig. 3.51. A monochromatic light source from a vertical slit is focused onto the camera plane by the main lens. The light passes through two parallel slits one in front of each of the two channels of a Rayleigh-type diffusion cell, and then through a horizontal cylindrical lens.If both channels contain fluids of the same refractive index, the interference pattern observed is determined solely by the superposition of the diffraction envelopes generated by the two slits. In this way, equally spaced fringes are produced within the diffraction envelope known as reference fringes. The zeroth-order fringe, which corresponds to equal optical path lengths for the two beams is located at the center of the envelope. If the refractive index of one channel is increased the interference fringes that are conjugate to the channel move sideways within the diffraction envelope and the displacement of any given fringe is proportional to the refractive index difference between the two channels. If, to this system one adds a horizontal, cylindrical lens so that the cells are imaged on the camera plane and also makes one channel a cell in which free diffusion takes place according to (3.179), accompanied by the refractive index changes of (3.184), then different vertical positions in the cell are subject to different refractive index changes so that the resulting fringe pattern will be that shown in Fig. 3.52. In this case, each fringe is shifted by an amount depending upon the extent of diffusion at each vertical position from a corresponding reference fringe. The reference fringes can themselves be obtained continuously from interference in regions of both cells where there is no diffusive perturbation such as the ends of the cell.

Measurements of the fringe shifts at a vertical position Z with respect to the initial boundary position may be used to determine the diffusion coefficient. If j denotes the j-th minimum in the fringe pattern about its center and J is the total number of fringes which corresponds to the refractive-index difference between the two initial solutions in the diffusion cell, then (3.184) leads to the result

$$(2j - J) = \mathrm{erf}(y^*) \,. \tag{3.185}$$

Now

$$y^* = \frac{Z}{2\sqrt{D_{12}t}} \tag{3.186}$$

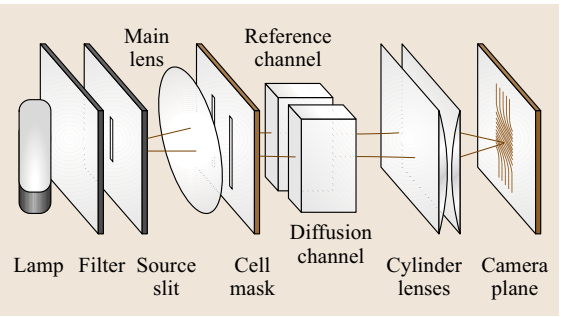

Fig. 3.51 Schematic view of Rayleigh interferometer [3.194]

so that, if (3.185) and (3.186) are written for both the j-th and $(J - j)$-th fringes, it is possible to obtain the result that for an interferogram photographed at time t:

$$D_{12} = \frac{\left[(X_{J-j} - X_j)/2y^*\right]^2}{4M^2 t} \,, \tag{3.187}$$

where X_j and X_{J-j} are the fringe shifts for the j-th and $J - j$-th minima in the pattern on the photographic plate, y^* is the appropriate solution of (3.185) and M is the magnification factor of the optical system.

The Rayleigh interferometric technique has been employed for a number of precise measurements of diffusion coefficient by *Sundelöf* [3.195], *Longsworth* [3.196] and *Svensson* [3.197] among others. In recent years, laser light sources have considerably

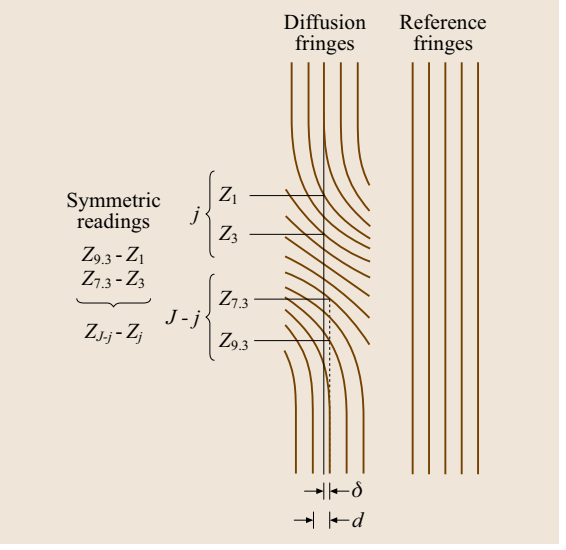

Fig. 3.52 Schematic diagram of Rayleigh interference fringes

simplified the design of Rayleigh interferometers and its modifications [3.198, 199]. This is because the coherence of the laser light removes the need for careful matching of the optical paths of the two beams which is necessary to observe interference fringes with ordinary light sources. In general, the Rayleigh interferometric technique is a very good method for measuring diffusion coefficients at moderately low (0.01 molar) to high concentrations. It is also characterized by a simple run procedure and theory, but it has seldom been applied far from ambient temperature because of the difficulties of ensuring stable optical paths in large temperature gradients.

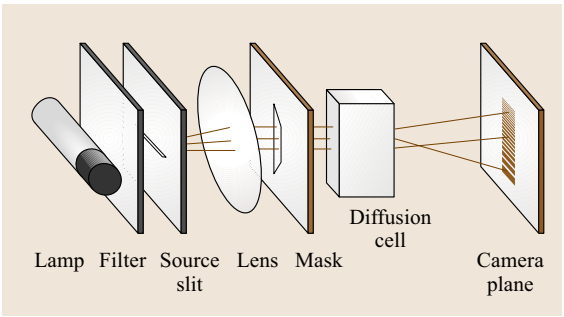

Fig. 3.53 Schematic view of Gouy interferometer (after [3.200])

Gouy Interferometric Technique

As already discussed, fringe positions in Rayleigh patterns yield the refractive index at corresponding levels of the diffusion cell. Fringe positions in Gouy fringe patterns are a Fourier transform of the refractive-index gradient $\partial n/\partial z$ and are related to the symmetrical positions of the gradient about the position of the maximum gradient.

Figure 3.53 illustrates a common configuration for a Gouy apparatus. The instrument is physically simpler than the Rayleigh one shown in Fig. 3.51; there is only one lens, and besides the cell, the only other optical components are the lamp, filter and slit. However, the theory of the device is more complicated.

In the Gouy system any light ray that passes through the diffusion-affected region of the free-diffusion cell will be deflected away from its point of intersection with the photographic plate in the absence of diffusion. The amount of this displacement is, to a first-order approximation, proportional to the refractive index gradient at the position in the diffusion cell at the height where the light crosses the cell. Interference fringes then arise at the photographic plate because rays that follow paths through different parts of the diffusion cell may have the same point of intersection with the photographic plate.

A set of *Gouy* [3.200] fringe patterns is illustrated in Fig. 3.54 together with a set of Rayleigh reference fringes. The Rayleigh fringes are formed by using light passing through regions of the diffusion cell undisturbed by diffusion and they are used to determine the position of the undeviated image of the slit on the photographic plate. Here $Y_0, Y_1, \ldots, Y_j$ are the distances from the undeviated slit image to the outermost fringe minimum ($j = 0$), next outer minimum ($j = 1$), etc. The distance C_t is the maximum Y-position that light would reach according to ray optical theory [3.201]. Equations for the analysis of Gouy interferometric fringe patterns to determine binary diffusion coefficients were derived independently by *Kegeles* and *Gosting* [3.201] and *Coulson* et al. [3.202]. According to Kegeles and Gosting, the positions of fringe minima Y_j are related to a parameter z_j by

$$Y_j = C_t \exp\left(-z_j^2\right) . \tag{3.188}$$

The parameters z_j may be evaluated from the equations

$$f(z_j) = \operatorname{erf}(z_j) - \left(2\frac{z_j}{\sqrt{\pi}}\right)\exp\left(-z_j^2\right) , \tag{3.189}$$

$$f(z_j) = \frac{(j + Z_j)}{J} . \tag{3.190}$$

Here Z_j is a quantity for fringe j, which is calculated for fringe minima from wave optics [3.203]; it approaches 3/4 for large j. The binary diffusion coefficient is related to C_t by

$$D_{12} = \frac{(J\lambda b)^2}{4\pi C_t^2 t} , \tag{3.191}$$

where b is the optical distance from the center of the cell to the camera plane.

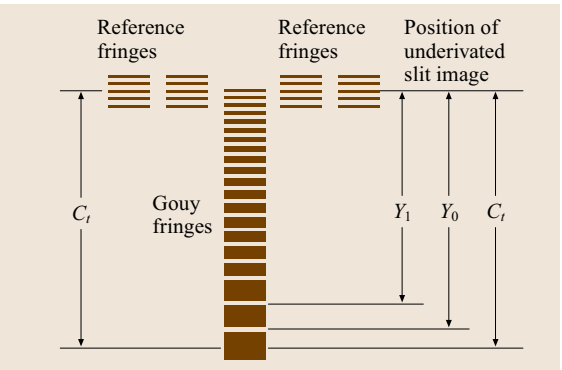

Fig. 3.54 Schematic diagram of Gouy interference fringes

Gouy interferometry has been the most widely used technique for the study of diffusion in liquids. Many careful experiments can be found in literature [3.201, 203]. As with most interferometric techniques there have been few applications far from ambient conditions.

3.6.2 Diffusion in Gases

The study of diffusion in gases began in 1863 with *Graham* [3.205], who was not only a pioneer in the field but also one its most ingenious experimentalists. Indeed, his experiments were performed even before the formulation of Fick's law. Since his work, numerous attempts have been made to devise new methods and to improve existing methods of measurement. A survey given by *Marrero* and *Mason* [3.206] summarizes the most important developments until that date and a more recent monograph by *Dunlop* et al. [3.207] provides a comprehensive review of experimental techniques.

The purpose of this section is to discuss widely used and accurate methods rather than to give an extensive overview of all the available techniques. As in the previous section on diffusion in liquids, the attention is focused only on the measurement of the mutual diffusion coefficient in binary systems.

Closed-Tube Technique

The closed-tube technique originally developed by *Graham* [3.205] in 1863 was employed by *Loschmidt* [3.208] to determine the diffusion coefficient for 10 gases in the temperature range 252–293 K. This type of instrument has therefore become known as the Loschmidt cell. In Fig. 3.55, a schematic diagram of a high-pressure Loschmidt cell employed by *Shankland* and *Dunlop* [3.204] is shown. The cell was constructed in two antisymmetric halves joined about a central pivot. The cell could be operated at pressures up to 2 MPa without leakage. At the start of an experiment the two halves of the cell were filled with different pure gases to the same total pressure. After thermal equilibrium was attained, the diffusion process was begun by rotating the upper half-cell about the central pivot to bring the two sections into coincidence.

Assuming that the diffusion coefficient D_{12} is independent of the mixture composition, for a total tube length L, the solution of (3.166) is [3.209, 210]

$$C_1(z,t) = \sum_{n=0}^{\infty} A_n \cos\left(\frac{n\pi z}{L}\right) \exp\left(-\frac{n^2\pi^2 D_{12} t}{L^2}\right), \tag{3.192}$$

where the coefficients A_n depend on the initial concentrations

$$A_0 = \frac{b}{L} C_{1B} + \left(\frac{L-b}{L}\right) C_{1T} \tag{3.193}$$

and for $n \geq 1$,

$$A_n = \left[\frac{-2(C_{1T} - C_{2B})}{n\pi}\right] \sin\left(\frac{n\pi b}{L}\right). \tag{3.194}$$

In these equations, b is the position of the boundary between the two cells, and

$$\begin{aligned} C_1(z,0) &= C_{1T}\,, & b \leq z \leq L\,, \\ C_1(z,0) &= C_{1B}\,, & 0 \leq z \leq b\,. \end{aligned} \tag{3.195}$$

There are two different ways in which this basic solution may be employed for the measurement of the diffusion coefficient. In the first method the concentrations are measured at two planes normal to the longitudinal axis of the cells which are equidistant from the initial boundary. Then, all of the even terms in the summation of (3.192) disappear. Further simplifications can be made if the distance of the detection planes from the initial boundary is chosen to be $L/3$ because then the equation – truncated to include just the first term with

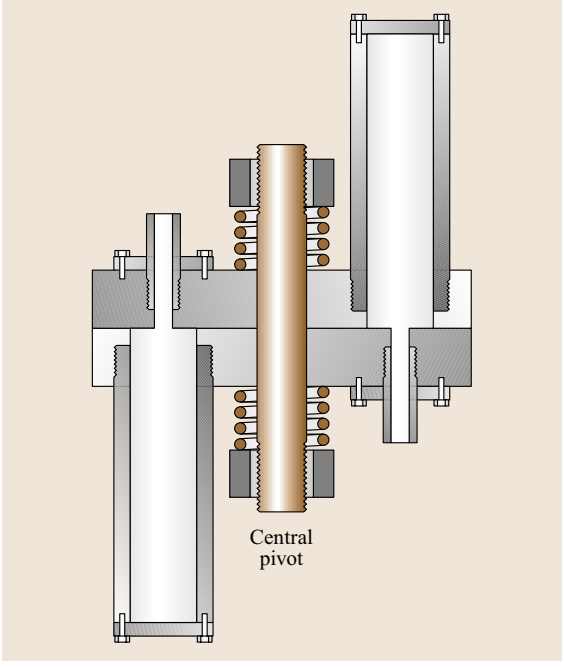

Fig. 3.55 High-pressure Loschmidt cell developed by *Shankland* and *Dunlop* [3.204]

negligible error – becomes

$$\Delta C_1(t) = 2A_1 \cos\left(\frac{\pi}{6}\right) \exp\left(-\frac{\pi^2 D_{12} t}{L^2}\right) \quad (3.196)$$

and the diffusion coefficient can be determined from measurements of ΔC_1 as a function of time by a least-squares regression technique. In this case the measurements of concentrations at the selected planes can be done by a variety of in situ means that have included interferometric means and thermal conductivity sensors.

In an alternative method of using the Loschmidt cell, the diffusion process is stopped after a time t_m before mixing is complete [3.210]. If the initial boundary is formed at $z = b = L/2$, and the two halves of the cell can be isolated from one another after the time t_m (Fig. 3.55), the average concentration in each half of the cell can be measured. If the average concentration of species 1 in the upper half of the cell at time t_m is denoted by $\langle C_{1T}\rangle$ and that in the lower half of the cell by $\langle C_{1B}\rangle$ these two quantities can be evaluated by averaging the concentration distribution of (3.192) over the length of each half-cell at time t_m, so that

$$\frac{\langle C_{1T}\rangle - \langle C_{1B}\rangle}{C_{1T} - C_{1B}} = \frac{8}{\pi^2} \sum_{n=0}^{\infty} \frac{\exp\left[-(2n+1)^2 \pi^2 D_{12} t_m / L^2\right]}{(2n+1)^2}, \quad (3.197)$$

which enables D_{12} to be determined from measurements of $\langle C_{1T}\rangle$, $\langle C_{1B}\rangle$, t_m and L. This equation can further be simplified by the proper choice of time t_m [3.210]. The method of composition analysis in this type of instrument can be any means that has adequate precision for the gaseous systems under study, including mass spectrometry.

In the first approach, the exact nature of the initial experimental conditions do not influence the evaluation of the diffusion coefficient from $\Delta C_1(t)$ as a function of t. This approach depends on the time interval between concentration measurements but not on the absolute time at which these measurements are made. On the other hand, the second method depends upon the measured time from the start of the diffusion process, as well as upon the initial concentrations in the two halves of the cell prior to a measurement.

Two-Bulb Technique

The two-bulb technique is the most widely used method for determining the diffusion coefficients of gases [3.211]. The basic arrangement for a two-bulb cell consists of two chambers of relatively large volume joined by a small-bore, small-volume diffusion tube. Initially, the two chambers are filled with fluid mixtures of different composition at the same pressure which are allowed to approach a uniform composition by means of diffusion through the tube. In an ideal model of this type of instrument, it is assumed that the diffusion coefficient of the gas mixture is independent of composition, the gas mixtures are ideal, so that there is no volume change upon mixing or heat of mixing, and the transient temperature rises due to Dufour effects are insignificant [3.181]. It is also assumed that the concentration gradient is confined to the connecting tube whereas the composition within each bulb remains uniform at all times. In addition, the pressure is assumed to be uniform throughout the cell, so that viscous effects are negligible, and high enough to minimize free-molecular (Knudsen) diffusion [3.211].

Following these assumptions, (3.166) can be solved [3.181] to produce the working equation

$$C_{1T}(t) - C_{1B}(t) = [C_{1T}(0) - C_{1B}(0)] \exp\left(\frac{-t}{\tau}\right), \quad (3.198)$$

where

$$\tau = \left[\left(1 - \frac{V_c}{3(V_B + V_T)}\right) \frac{A D_{12}}{L} \left(\frac{1}{V_B} + \frac{1}{V_T}\right)\right]^{-1}. \quad (3.199)$$

In the above equations, the subscripts 'B' and 'T' refer to the bottom and top cell volumes, V_c the volume of the connecting tube of cross-sectional area A and length L. Therefore the diffusion coefficient can be obtained from measurements of the difference between the concentrations of one species in the top and bottom bulbs as a function of time, together with the dimensions of the diffusion cell.

The two-bulb cell shown in Fig. 3.56 was employed by *van Heijningen* et al. [3.212] for the measurement of the diffusion coefficients of monatomic gas mixtures in the temperature range 65–300 K. The estimated uncertainty of the measurements was ±0.5%. To monitor the concentration changes they employed thermistors, in the same way as *Yabsley* and *Dunlop* [3.211] in their measurements of the diffusion coefficient of helium–argon and helium–oxygen mixtures near room temperature. *Taylor* and *Cain* [3.213] monitored the composition changes by withdrawing samples of gas for mass spectrometric analysis at specific time intervals during the diffusion process. Their estimated uncertainty was ±2%.

Taylor–Dispersion Technique

The Taylor-dispersion technique described in the case of diffusion in liquids has also been applied to the measurement of the diffusion of gases. The principles of the application of the technique to gases are identical to those for liquids so that no new description is necessary here. However, it is necessary to point out one important difference between the application of the theory of the method to gases and liquids which derives from the fact that in the dilute gas phase the diffusion coefficient is approximately 10^5 times larger than in the liquid phase. As a consequence the principal contribution to the dispersion of a pulse of solute gas in gas-phase measurements is the direct molecular diffusion in the axial direction and not the Taylor-dispersion contribution arising from radial diffusion.

For the same reason the dimensions of the diffusion tubes employed for measurements in the dilute gas phase [3.214] are quite different from those employed in the liquid phase. Generally, a diffusion tube with a length of a few meters and a diameter of a few millimeters is employed for measurements in the dilute gas state. When combined with the low viscosity of the gas this means that it is very difficult to satisfy all of the conditions [3.210] necessary for absolute measurements. Thus, although the technique yields a gas-phase diffusion coefficient within a period of 15 min, and is readily applied over a wide range of temperature, the uncertainty of the results has generally been modest [3.210].

More recently the same technique has been applied to measure the diffusion coefficients of gases at elevated pressure with particular emphasis on the supercritical state [3.215, 216]. Under these conditions the diffusion coefficient of the system is much closer to that characteristic of the liquid phase so that the conditions of the theory are more easily satisfied and the apparatus is essentially identical to that employed for liquids. The Taylor-dispersion technique is particularly suitable for high-pressure applications because the element to be pressurized is simply a cylindrical-section tube and because the time required for a diffusion measurement can be retained within reasonable bounds (about one hour) without a loss of uncertainty [3.215, 216].

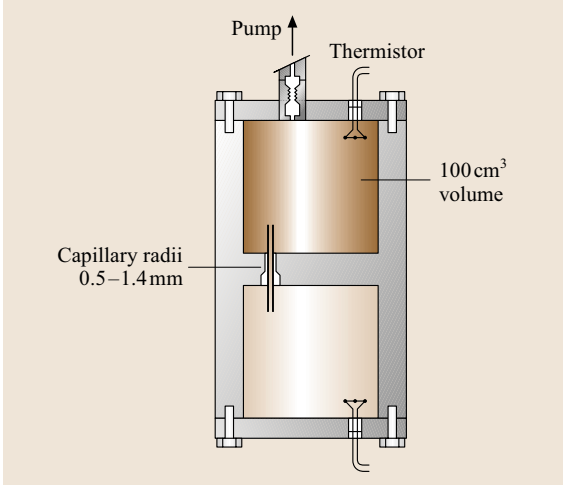

Fig. 3.56 Two-bulb cell of *van Heijningen* et al. [3.212]

Table 3.23 Integral diffusion coefficients for aqueous potassium chloride solutions at 25 °C

C_1 (mol dm^{-3})	$\overline{D}_{12}(C_1)\times10^9$ (m^{2}s^{-1})	C_1 (mol dm^{-3})	$\overline{D}_{12}(C_1)\times10^9$ (m^{2}s^{-1})
0.001	1.973	0.060	1.890
0.002	1.966	0.070	1.886
0.003	1.961	0.080	1.882
0.004	1.956	0.090	1.878
0.005	1.953	0.100	1.874
0.006	1.949	0.200	1.857
0.007	1.947	0.300	1.850
0.008	1.944	0.400	1.848
0.009	1.941	0.500	1.848
0.010	1.939	0.600	1.849
0.020	1.923	0.700	1.850
0.030	1.911	0.800	1.852
0.040	1.903	0.900	1.855
0.050	1.896	1.000	1.858

3.6.3 Diffusion Reference Values

The interdiffusion coefficient of aqueous solutions of potassium chloride is recommended as the reference standard [3.181] for the liquid phase. The values given in

Table 3.24 Calibration data for gas-phase diffusion coefficients at a pressure of 0.101325 MPa

System	$D_{12}(0)\times10^5$ m^{2}s^{-1}	a_1	a_2
He–Ar	7.344	0.0846	1.4825
He–N_2	7.067	0.0676	1.4883
He–O_2	7.469	0.0564	1.1270
He–CO_2	6.029	0.0905	2.3952
N_2–Ar	2.034	0.0041	0.0

Table 3.25 Diffusion coefficient D_{12} ($\times 10^{-9} m^2 s^{-1}$) of some hydrocarbons in supercritical CO_2

		299.15 K 9.0 MPa	299.15 K 10.5 MPa	303.15 K 10.5 MPa	305.65 K 10.5 MPa	308.15 K 10.5 MPa
n-Pentane	C_5H_{12}	13.7	13.0	14.1	15.7	17.6
n-Hexane	C_6H_{14}	13.7	13.0	14.0	15.4	17.6
n-Heptane	C_7H_{16}	13.4	12.6	14.0	15.4	17.1
n-Octane	C_8H_{18}	13.2	12.4	13.5	15.2	17.1
n-Nonane	C_9H_{20}	12.9	12.1	13.3	14.9	16.7
n-Decane	$C_{10}H_{22}$	12.5	11.8	13.0	14.6	16.1
n-Undecane	$C_{11}H_{24}$	12.2	11.5	12.7	14.5	16.1
n-Dodecane	$C_{12}H_{26}$	11.3	11.0	12.0	13.9	15.7
n-Tetradecane	$C_{14}H_{30}$	9.53	9.41	10.9	12.4	14.1
Acetone	CH_3COCH_3	14.3	14.2	15.2	16.2	17.6
Benzene	C_6H_6	14.3	14.0	15.0	15.8	17.4

Table 3.26 Diffusion coefficient D_{12} ($\times 10^{-9} m^2 s^{-1}$) of some organic solutes in *n*-hexane

	213.2 K	233.2 K	253.2 K	273.2 K	299.2 K	313.2 K	333.2 K
Benzene	1.21	1.80	2.57	3.43	4.70	5.53	6.96
o-Difluorobenzene	1.10	1.60	2.41	3.35	4.46	5.26	6.61
p-Difluorobenzene	1.10	1.72	2.49	3.36	4.63	5.42	6.62
1,2,4-Trifluorobenzene	1.18	1.72	2.33	3.20	4.40	5.20	6.34
1,2,3,5-Tetrafluorobenzene	1.05	1.67	2.27	3.34	4.40	4.95	6.48
1,2,4,5-Tetrafluorobenzene	1.05	1.68	2.22	3.16	4.40	5.17	6.20
Pentafluorobenzene	1.06	1.70	2.26	2.98	4.00	4.83	5.95
Hexafluorobenzene	1.01	1.62	2.16	2.84	4.05	4.62	5.81
Octafluorobenzene	0.88	1.40	1.83	2.47	3.50	4.07	4.98

Table 3.23 are the integral diffusion coefficient defined as

$$\overline{D}_{12}(\overline{C}_1) = \frac{1}{\overline{C}_1} \int_0^{\overline{C}_1} D_{12}\, dC_1 \,, \qquad (3.200)$$

where D_{12} is the true *differential* diffusion coefficient and C_1 is the concentration of species 1 in one of the two chambers of a diaphragm cell [3.217]. The values in Table 3.23 have been derived from the data of *Woolf* and *Tilley* [3.183].

For gas mixtures recommended values of the diffusion coefficients of five mixtures at 300 K and 0.101325 MPa can be calculated from

$$D_{12} = D_{12}(0)\left(1 + \frac{a_1 x_2}{1 + a_2 x_2}\right) . \qquad (3.201)$$

Here, x_2 represents the mole fraction of the heavier component and values of $D_{12}(0)$, a_1 and a_2 are listed in Table 3.24. Equation (3.201) represents the experimental data by *Dunlop* et al. [3.218]; the estimated uncertainty of these data is about ±0.1%.

Temperature dependencies of diffusion coefficients in the range 50–1000 K are given by *Kestin* et al. [3.219].

3.6.4 Tables of Diffusion Coefficient Values

In Tables 3.25–3.27, the interdiffusion coefficient for some commonly encountered systems is given for en-

Table 3.27 Diffusion coefficient D_{12} ($\times 10^{-9} m^2 s^{-1}$) of some organic solutes in toluene

	299.2 K	323.2 K	348.2 K
n-Hexane	2.50	3.21	
n-Decane	1.84	2.52	3.22
n-Tetradecane	1.46	1.98	2.61

gineering purposes as a function of temperature and pressure. The data in Table 3.25 have been obtained by the Taylor dispersion technique with an estimated uncertainty of 3% [3.220]. Measurements presented in Tables 3.26 and 3.27 have an estimated uncertainty of 2.5% [3.221].

3.7 Electric and Magnetic Parameters of Liquids and Gases

This section describes measurements of the dielectric constant and electrical conductivity of fluids, as well as magnetic susceptibility. In the introduction some relevant electromagnetic parameters are discussed. Throughout the chapter the term permittivity will always be equivalent to the electrical permittivity, conductivity to the electrical conductivity, and permeability to the magnetic permeability.

3.7.1 Introduction

The speed of all electromagnetic radiation (the speed of light) in vacuum is the same for all the frequencies and is denoted by c. The value of c is 2.99792458×10^8 m/s. The speed of light c can be expressed via the permittivity ε_0 and permeability μ_0 of free space, as

$$c^2 = \frac{1}{\varepsilon_0\mu_0}\,, \tag{3.202}$$

where $\varepsilon_0 = 8.85418782\times10^{-12}\,\mathrm{F/m}$ and $\mu_0 = 4\pi\times10^{-7}\,\mathrm{N/A^2}$ (in SI units).

In other substances, however, the speed of electromagnetic radiation is a function of the radiation frequency and of the material properties. The factor by which the speed of a particular frequency of the electromagnetic radiation is changed relative to c when it travels inside a material is called the refractive index of the material at that particular frequency. That is, if v is the phase velocity of radiation of a particular frequency in a specific material, then the refractive index n is given by

$$n = \frac{c}{v}\,. \tag{3.203}$$

The refractive index for a number of materials and aqueous solutions is given in Tables 3.28 and 3.29, respectively. The dependence of the refractive index of a material on frequency (except in vacuum, where all frequencies travel at c) is seen in the effect known as dispersion. This is the division of white light into its constituent spectral colors, such as when it travels through a prism, and is the cause of chromatic aberration in lenses. If the refractive indices of two materials are known for a given frequency, then one can compute the angle by which radiation of that frequency will be refracted as it moves from the first material into the second using Snell's law. The refractive index is typically larger than one. The speed of light in air, for example, is slightly less than c. In denser media, such as water and glass, light can slow down to fractions of c such as $0.75c$ and $0.67c$.

The characteristic permittivity ε and permeability μ of a medium together determine the phase velocity of electromagnetic radiation through that medium according to

$$v^2 = \frac{1}{\varepsilon\mu}\,. \tag{3.204}$$

Thus the refractive index can be written as:

$$n^2 = \frac{\varepsilon\mu}{\varepsilon_0\mu_0}\,. \tag{3.205}$$

Also

$$\varepsilon = \varepsilon_\mathrm{r}\varepsilon_0\,, \tag{3.206}$$

$$\mu = \mu_\mathrm{r}\mu_0\,, \tag{3.207}$$

where ε_r is the relative permittivity or dielectric constant and μ_r is the relative permeability of the material. For nonmagnetic materials like, for example, most polymer solutions, μ_r is unity and thus the square of the refractive index is equal to the dielectric constant.

On the atomic level, the deceleration of the electromagnetic radiation as it enters a material may be attributed to the continuous process of absorption and emission of photons as they interact with the atoms of the material. Between atoms, the photons travel at the speed c, as in vacuum. As they interact with the atoms, they are absorbed and re-emitted, which results in a slight delay. On a sufficiently large scale the delay manifests itself as an overall reduction in the speed of light in the material. The absorption and emission process can be thought of as the electric field of a photon creating an oscillating force on the charges of each atom (primarily the electrons). This oscillation of charges itself causes the radiation of an electromagnetic field, which is slightly out of phase compared to that of the original photon,

Table 3.28 Some representative values of the refractive index at the wavelength of $\lambda = 589\,\text{nm}$ (yellow sodium light). Unless stated otherwise, the temperature is 298.15 K. Melting point is abbreviated by m.p.

Substance	n
Air	1.0002926
Bromine	1.661
Carbon dioxide	1.00045
Diamond	2.419
Glass	1.5–1.9
Glycerin	1.4729
Helium	1.000036
Sodium chloride at m.p. (1123.15 K)	1.408
$Na_2O \cdot SiO_2$ (solid)	1.52
Rock salt	1.516
Water (liquid) (293.15 K)	1.333
Water (solid) (273.15 K)	1.31

Table 3.29 Refractive index of several aqueous solutions at the wavelength of 589 nm (yellow sodium light) at 293.15 K and a weight concentration of 20% unless otherwise indicated

Solute	n
Acetic acid - CH_3COOH	1.3472
Acetic acid - CH_3COOH (100%)	1.3716
Ammonia – NH_3	1.3440
Ammonium chloride – NH_3CL	1.3708
Ammonium sulfate – $(NH_3)_2SO_4$	1.3677
Barium chloride – $BaCl_2$	1.3664
Calcium chloride – $CaCl_2$	1.3839
Cesium chloride – CsCl	1.3507
Citric acid – $(HO)C(COOH)_3$	1.3598
Ethanol – CH_3CH_2OH	1.3469
Ethanol – CH_3CH_2OH (100%)	1.3614
Formic Acid – HCOOH	1.3437
Glycerol – $CH_2OHCHOHCH_2OH$	1.3572
Glycerol – $CH_2OHCHOHCH_2OH$ (100%)	1.4735
Hydrochloric acid – HCl	1.3792
Magnesium chloride – MgCl	1.3859
Methanol – CH_3OH	1.3381
Methanol – CH_3OH (100%)	1.3290
Potassium bromide – KBr	1.3591
Silver nitrate – $AgNO_3$	1.3574
Sodium chloride – NaCl	1.3684
Sulfuric acid – H_2SO_4	1.3576

leading to a slight retardation of the field and an apparent delay in the photon's travel. Sometimes the refractive index is defined as a complex number, with the imaginary part representing the absorption of the material. This representation is particularly useful when analyzing the propagation of electromagnetic waves through metals.

The magnetic permeability μ used in physics and engineering is the degree of magnetization of a material in response to a magnetic field and is defined as the ratio of magnetic flux density $\boldsymbol{B}$ (also called magnetic induction) to the magnetic field strength $\boldsymbol{H}$

$$\mu = \frac{\boldsymbol{B}}{\boldsymbol{H}} \,. \tag{3.208}$$

Although magnetic permeability is related in physical terms most closely to electric permittivity, it is probably easier to think of permeability as of a sort of *resistance to magnetic flux*; just as those materials with high electrical conductivity let electric current through easily, materials with high permeabilities allow magnetic flux through more easily than others.

Sometimes, for non-ferromagnetic substances the permeability is so close to μ_0 that the magnetic susceptibility χ is used:

$$\mu_\mathrm{r} = 1 + \chi \,. \tag{3.209}$$

The magnetic susceptibility is also defined as the ratio of magnetization $\boldsymbol{M}$ to magnetic field strength $\boldsymbol{H}$. The magnetization is defined as the total vector sum of the magnetic moments of all the atoms in a given volume V divided by that volume. From Table 3.30, it is clear that the permeabilities of common diamagnetic and paramagnetic materials do not differ substantially from that of free space. In fact, to all intents and purposes, the magnetic properties of such materials can be safely neglected ($\mu_\mathrm{r} = 1$). Measurements of the magnetic susceptibility are described in detail in [3.222–226].

3.7.2 Dielectric Constant

The dielectric constant ε_r is an expression of the extent to which a material concentrates electric flux, and is the electrical equivalent of the relative magnetic permeability μ_r. As the dielectric constant increases, the electric flux density (the displacement current) increases. In electromagnetism, the permittivity ε of a medium is also introduces as the ratio $\boldsymbol{D}/\boldsymbol{E}$ of the electric displacement $\boldsymbol{D}$ to the electric field strength $\boldsymbol{E}$ when an external field is applied to the substance. Similarly to the magnetic susceptibility the electric susceptibility is defined as

$$\chi_\mathrm{e} = \varepsilon_\mathrm{r} - 1 \,, \tag{3.210}$$

Table 3.30 Magnetic susceptibilities of some ferro-, para- and diamagnetic materials at different temperatures. For temperatures other than room temperature, the value is given next to the material name. The following notation is used: (l) liquid, (g) gas, (s) solid. The values were taken from the sources indicated in the table

Material	χ
Acetone (C_3H_6O) (l) [3.227]	-5.7803×10^{-06}
Aluminum (s) [3.228]	2.2×10^{-5}
Ammonia (g) [3.228]	-1.06×10^{-5}
Antimony (l, 903.78 K) [3.229]	-5.74409×10^{-7}
Bismuth (l, 544.55 K) [3.229]	-6.63033×10^{-6}
Bismuth (s) [3.228]	-1.67000×10^{-4}
Cadmium (l, 673.15 K) [3.230]	-1.63049×10^{-3}
Chlorine (Cl_2) (l, 238.65 K) [3.231]	-1.11623×10^{-5}
Copper (s) [3.228]	-9.8×10^{-6}
Diamond (s) [3.228]	-2.2×10^{-5}
Ethanol (C_6H_6O) (l) [3.227]	-3.55392×10^{-6}
Germanium (l, 1211.67 K) [3.232]	6.25289×10^{-6}
Glycerol ($C_3H_8O_3$) (l) [3.227]	-9.82884×10^{-6}
Hydrogen (H_2) (l, 20.3 K) [3.231]	-2.29758×10^{-6}
Hydrogen (g, 1 atm) [3.228]	-2.1×10^{-9}
Indium (l, 673.15 K) [3.230]	-8.26742×10^{-4}
Indium (l, 429.75 K) [3.229]	-5.02831×10^{-6}
Iron (s) [3.228]	3.0×10^{3}
Lead (l, 600.62 K) [3.232]	-1.1773×10^{-5}
Lead (l, 600.61 K) [3.229]	-8.97515×10^{-6}
Mercury (l) [3.231]	-2.84026×10^{-5}
MnZn ($Fe_2O_4)_2$ (s) [3.228]	2.5×10^{3}
Nitrogen (g, 1 atm) [3.228]	-5.0×10^{-9}
Oxygen (O_2) (l, 90 K) [3.231]	3.44981×10^{-3}
Oxygen (g, 1 atm) [3.228]	2.09×10^{-6}
Potassium (l, 673.15 K) [3.230]	2.07219×10^{-4}
Silicon (s) [7]	-3.7×10^{-6}
Silver (l, 1234.93 K) [3.232]	-2.64816×10^{-5}
Silver (l, 1234.93 K) [3.229]	-2.57661×10^{-5}
Sulphuric acid (H_2SO_4) (l) [3.231]	-9.1473×10^{-6}
Terbium (s) [3.228]	9.51×10^{-2}
Tin (l, 505.08 K) [3.232]	-3.1157×10^{-6}
Tin (l, 505.08 K) [3.229]	-1.31758×10^{-6}
Toluene (C_7H_8) (l) [3.227]	-7.69998×10^{-6}
Tungsten (s) [3.228]	6.8×10^{-5}
Water (l) [3.231]	-9.04015×10^{-6}
Water (l) [3.228]	-9.0×10^{-6}

where the electric susceptibility χ_e, is also defined as the ratio of polarization $\boldsymbol{P}$ to the electric field strength $\boldsymbol{E}$. In general, the dielectric constant can be defined as a complex number, with the real part expressing reflective surface properties (Fresnel reflection coefficients), and the imaginary part expressing the radio absorption coefficient k_v.

When an electric field is applied to a medium, an electric current propagates. The total current propagating in a real medium is in general composed of two parts: a conduction current $\boldsymbol{J}_c$ and a displacement current $\boldsymbol{J}_d$. A perfect dielectric is a material that shows displacement current only. In the case of a leaky dielectric medium (i. e., when conduction currents are not negligible) the total current density is

$$\boldsymbol{J}_{tot} = \boldsymbol{J}_c + \boldsymbol{J}_d = \sigma\boldsymbol{E} + i\omega\varepsilon\boldsymbol{E} = i\omega\varepsilon^*\boldsymbol{E}\,, \tag{3.211}$$

where σ is the specific conductivity of the medium, and the complex permittivity ε^* is defined as

$$\varepsilon^* = \varepsilon_r - i\frac{\sigma}{\varepsilon_0\omega}\,, \tag{3.212}$$

where $i = \sqrt{-1}$, and $\omega = 2\pi f$ is the angular frequency.

The permittivity of liquids in the radio frequency and microwave regions can also be presented by the Debye equation [3.233, 234]:

$$\varepsilon^* = \varepsilon' + i\varepsilon''\,, \tag{3.213a}$$

where

$$\varepsilon' = \varepsilon_\infty + \frac{\varepsilon_s - \varepsilon_\infty}{1+\omega^2\tau^2}\,, \tag{3.213b}$$

$$\varepsilon'' = \frac{(\varepsilon_s - \varepsilon_\infty)\,\omega\tau}{1+\omega^2\tau^2}\,. \tag{3.213c}$$

ε_s is the permittivity measured in a static field or at low frequencies where no relaxation effects occur, and ε_∞ is a parameter describing the permittivity in the high-frequency limit. τ is the relaxation time for molecular orientation. The values of the dielectric constant for a number of liquids and gases are given in Table 3.31.

3.7.3 Electric Conductivity

The electric conductivity is a measure of how well a material accommodates the transport of electric charge (the detailed physical mechanisms of conductivity in liquids are discussed in Chap. 22). Conductance is an electrical phenomenon where a material contains movable particles of electricity. When a difference of electrical potential is applied across a conductor, its movable charges flow, and an electric current appears. A conductor such as a metal has high conductivity, and an insulator like glass, or vacuum, has low conductivity.

Table 3.31 The dielectric constants ε_r measured in static fields or at low frequencies where no relaxation effects occur

Solvent	ε_r	T (K)
Acetone[1]	20.7	298.15
Acetonitrile[1]	36.7	298.15
Ammonia[1] (239 K)	22	298.15
Ammonia[2]	16.61	293.2
Argon[2]	1.3247	140
Benzene[1]	2.27	298.15
Bromine[2]	3.1484	297.9
Bromine trifluoride[2]	106.8	298.2
Chlorine[2]	2.147	208.0
Dimethyl acetamide[1]	37.78	298.15
Dimethyl sulfoxide[1]	46.7	298.15
Dioxan[1]	2.21	298.15
Ethanol	24.3	298.15
Ethylene diamine[1]	12.9	298.15
Hydrogen[2]	1.2792	13.52
Hydrogen chloride[2]	14.3	158.9
Hydrogen cyanide[1] (289 K)	118.3	298.15
Hydrogen fluoride[2]	83.6	273.2
Iodine[2]	11.08	391.25
Krypton[2]	1.664	119.8
Oxygen[2]	1.5684	54.478
Ozone[2]	4.75	90.2
Phosphorus[2]	4.096	307.2
Pyridine[1]	12	298.15
Selenium[2]	5.44	510.65
Sulfur[2]	3.4991	407.2
Sulfuric acid[1]	101	298.15
Water	80.1	293.15
Xenon[2]	1.88	161.35

[1] denotes the values adopted from [3.235] and [3.236],
[2] denotes the values adopted from [3.237–239]

A semiconductor has a conductivity that may vary with conditions, such as exposure to certain frequencies of light.

Electric currents in electrolytes are flows of electrically charged ions. For example, if an electric field is applied to a solution of salt NaCl, which dissociates to Na^+ and Cl^-, the sodium ions will move towards the negative electrode (anode), and the chlorine ions will move towards the positive electrode (cathode). If the conditions are right, redox reactions will take place, which release electrons from the chlorine, and allow electrons to be absorbed into the sodium. In water ice and in certain solid electrolytes, flowing protons constitute the electric current.

The specific electrical conductivity σ is the reciprocal of the specific electrical resistivity measured in SI units in Ohm m (Ω m). The corresponding units of σ are S/m ($S = \Omega^{-1}$ stands for Siemens). Table 3.32 shows the value of σ measured for a number of substances. It is equal to the ratio of the current density $\boldsymbol{J}$ to the electric field strength $\boldsymbol{E}$, as defined in the previous section. The latter also applies to the electrolytic conductivity of fluids.

Since in ordinary nonmetallic liquids the electric charge and current are generally related with dissolved ions, charge may be induced in poorly conducting liquids even though equilibrium net charge initially is absent. In electrohydrodynamics most work until the 1960s focused on the behavior of perfect or good conductors (mercury or water), or almost perfect dielectrics (apolar liquids such as benzene). That began to change following studies of poorly conducting liquids – leaky dielectrics [3.240].

The leaky dielectric can be modeled by the Navier–Stokes equations to describe fluid motion and an equation of charge conservation employing its Ohmic

Table 3.32 Representative values of specific conductivities

Substance	σ (1/Ωcm)	T (K)
Copper	5.8×10^5	293.15
Iron	1.1×10^5	273.15
Lead	4.9×10^5	273.15
Lithium chloride (melt)	6.221	983.15
Mercury	1.1×10^4	293.15
Molten oxide $CaO\cdot SiO_2$	0.8	2023.15
Molten oxide $K_2O\cdot 2SiO_2$	1.5	2023.15
Molten oxide $Li_2O\cdot SiO_2$	5.5	2023.15
Molten oxide $Li_2O\cdot 2SiO_2$	2.5	2023.15
Molten oxide $Na_2O\cdot SiO_2$	4.8	2023.15
Molten oxide $Na_2O\cdot 2SiO_2$	2.1	2023.15
Potassium chloride (0.01%) in water	1.3×10^{-2}	298.15
Potassium chloride (melt)	2.407	1145.15
Sodium chloride (solid)	1×10^{-3}	1073.15
Sodium chloride (melt)	3.9	1173.15
Sodium at melting point (m.p.)	1.04×10^5	370.98
Sodium chloride at m.p.	3.58	1074.15
Sulphuric acid (0.4%) in water	7.5×10^{-1}	291.15
Water	4×10^{-8}	291.15
Xylene	1×10^{-19}	298.15

conductivity. Electromechanical coupling occurs only at the interfaces where charge, carried to the interface by conduction, results in stresses of electric origin different from those present in perfect dielectrics or perfect conductors. With perfect conductors or dielectrics with no embedded charges, the stresses of the electric origin are perpendicular to the interface and alterations of the interfacial shape combined with the interfacial tension serve to balance the electric stress. Leaky dielectrics are different because free charges accumulated on the interface modify the field, and in particular, produce shear stresses. Viscous flow develops to provide stresses to balance the action of the shear stress components resulting from the tangential electric field acting on the interfacial charge.

The leaky dielectric model arises naturally through a scale analysis. Under static conditions, electric and magnetic phenomena are independent since their fields are uncoupled [3.241]. Insofar as the characteristic time for electrostatic processes is large compared to that for magnetic phenomena, the electrostatic equations furnish an accurate approximation. When external magnetic fields are absent, magnetic effects can be ignored completely. From Maxwell's equations, the characteristic time for electric phenomena τ_c can be identified as the ratio of electric permittivity and conductivity,

$$\tau_c = \frac{\varepsilon}{\sigma} . \tag{3.214}$$

For magnetic phenomena the characteristic time τ_M is the product of the magnetic permeability, conductivity and the square of the characteristic length

$$\tau_M = \mu\sigma l^2 . \tag{3.215}$$

Transport process time scales τ_P arise from viscous relaxation, diffusion, oscillation of an imposed field, or motion of a boundary. Slow processes are defined as those where $\tau_P \geq \tau_c \gg \tau_M$. The second inequality can be rearranged to give $(\varepsilon_r/\mu_r)^{1/2}\,\varepsilon_0/\sigma \gg l\,(\varepsilon_0\mu_0)^{1/2}$, and since $c = (\varepsilon_0\mu_0)^{-1/2}$, the right-hand side of this inequality is extremely small for leaky dielectric systems, for example most polymer solutions. On the other hand, if $\tau_P \gg \tau_c$, the liquid could be considered a perfect conductor, while for $\tau_P \sim \tau_c$ it is a leaky dielectric (a poor conductor), where interaction of the electric and hydrodynamic fields is still very important in spite of the fact that the fluid is electrically neutral in the bulk and the excessive charge accumulates only at the interfaces.

Ion Mobility

In general, ions are responsible for the transport of the electric charge in fluids. There are two aspects of ionic motion. First, there is the individual aspect. This concerns the dynamic behavior of separate ions. These ionic motions are basically random in direction and speed. Second, ionic motions have a group aspect that is of particular significance when more ions move in certain directions than in the others, and produce a drift, or flux, of ions. A flux of ions can come about in three ways. If there is a difference in the concentration of ions in different regions of the electrolyte (a leaky dielectric), the resulting concentration gradient produces a flow of ions. This phenomenon is termed diffusion (Sect. 3.6). If there are differences in the electrostatic potential at various points in the electrolyte, then the resulting electric field produces an additional flow of charge (and thus, of the ions) in the direction of the electric field. This is termed migration or conduction. Finally, if a difference in pressure, density, or temperature exists in various parts of the electrolyte, then the liquid begins to move as a whole or parts of it move relative to the other parts. This is an ordinary hydrodynamic flow, which, however, results in ion/charge convection [3.236]. There are of course fluids where the electric charge is transported by electrons and holes irrespective of the motion of the molecules/ions in the fluid. This is characteristic of metallic fluids such as mercury or molten alloys. The electric charge carriers in a fluid can consist of both ions and electrons. Examples of such fluids are solutions of conducting polymers like MEH-PPV [poly(2-methoxy, 5-(2'-ethyl-hexoxy)-1, 4-phenylene-vinylene)] [3.242, 243], polypyrrole [3.244] and polyaniline doped with d,l-camphorsulfonic acid [3.245].

Ions, like electrons, do not move at the speed of light when carrying charge from one point to another. Ions in solution participate in random (Brownian) motion in which they change momentum as a result of collisions with the other molecules and ions. Statistical bias in the motion of ions without electric field is the result of diffusion due to inequalities in the ion numbers in different regions. *Robinson* and *Stokes* [3.246] note that in the case where there are no other forces, it may be convenient to consider the electric field as representing a force. In this discussion we will concentrate on the electric field as the driving force for ion drift.

A Simplified Picture of Ionic Motion under the Influence of an Applied Electric Field. Under the influence of an external force like those corresponding to an applied electric field, ion motions are affected because of the fact that the ions are charged. Hence, the imposition of an electric field singles out one direction in space for preferential ionic movement. The walk is no longer per-

fectly random – the ions drift. Were an ion is completely isolated (in vacuum), it would accelerate indefinitely until it will collide with an electrode. In an electrolyte solution, an ion very soon collides with some other ion or with a solvent molecule that crosses its path. The ion changes directions; however, the electric field imparts to the ion a direction.

The initial velocity of the ion can be ignored precisely because it is random and therefore does not contribute to the preferred motion (drift) of the ion. The applied electric field imparts a sure component to the random velocities of the ion. This extra velocity component is in the direction of the electric force vector $\boldsymbol{F}$ and is called the drift velocity.

From Newton's second law we have the acceleration as

$$\frac{\mathrm{d}\boldsymbol{v}}{\mathrm{d}t} = \frac{\boldsymbol{F}}{m} , \tag{3.216}$$

where m is the ion mass.

The drift velocity ($\boldsymbol{v}_\mathrm{d}$) is estimated as the product of the acceleration and the average time between collisions τ,

$$\boldsymbol{v}_\mathrm{d} = \frac{\mathrm{d}\boldsymbol{v}}{\mathrm{d}t}\tau = \frac{\tau}{m}\boldsymbol{F} . \tag{3.217}$$

The flux of ions is related to the drift velocity in the following way

$$\text{Flux} = \text{Concentration of ions} \times \text{Drift velocity} . \tag{3.218}$$

Thus, if $\boldsymbol{F}$ is an electric force that induces conduction, then this equation is the molecular basis of the fundamental relation used in the macroscopic view of conduction, i. e.

$$\text{Flux} \propto \text{Electric field} . \tag{3.219}$$

The expression (3.217) reveals the condition under which the proportionality between the drift velocity (flux) and electric field breaks down. It is essential that in a collision an ion does not preserve any part of its extra velocity component arising from the electric force. If it did, then the actual drift velocity would be greater than that calculated by (3.217) because there would be a cumulative carryover of the extra velocity from collision to collision. Thus, every collision must eliminate all traces of the force-derived extra velocity, and the ion must start afresh to acquire the additional velocity. This condition can be satisfied only if the drift velocity, and therefore the field, is sufficiently small.

The proportionality constant τ/m in (3.217) is referred to as the (generalized) absolute mobility M_abs because it is an index of how mobile the ions are

$$M_\mathrm{abs} = \frac{\tau}{m} = \frac{\boldsymbol{v}_\mathrm{d}}{\boldsymbol{F}} . \tag{3.220}$$

The force acting on an ion in an electric field ($\boldsymbol{E}$) is equal to the charge of the ion times the field at the point where the ion is situated

$$\boldsymbol{F} = z_\mathrm{i} e_0 \boldsymbol{E} , \tag{3.221}$$

where e_0 is the electron charge, and z_i the valence of the ion. In the literature, mobilities are usually defined as the ratio of $\boldsymbol{v}_\mathrm{d}$ to $\boldsymbol{E}$, which introduces the conventional or electrical mobility

$$M_\mathrm{e} = \frac{\boldsymbol{v}_\mathrm{d}}{\boldsymbol{E}} = M_\mathrm{abs} z_\mathrm{i} e_0 . \tag{3.222}$$

Though the two types of mobilities are closely related, it must be stressed that the concept of absolute mobility is more general because it can be used for any force that determines the drift velocity of ions and not only the electric force used in the definition of electrical mobilities.

The Relation between the Equivalent Conductivity and the Absolute Mobility of an Ion. The motion of an isolated body is obviously governed by Newton's second law, but in dealing with the motion of ions it is not usually necessary to consider the acceleration unless electrical fields of very high intensities or frequencies are involved. Under normal conditions, the ions are almost instantaneously accelerated to the point where their motion is limited by the viscous drag of the solvent, and all the energy supplied by the electric field is dissipated by the viscous forces. The ions thus move with a constant limiting or terminal velocity, which for all reasonably small fields is directly proportional to the applied field. This is of course the reason for the validity of Ohm's law for electrolytes subjected to ordinary electric fields, and for the fact that the conductivities of ion-containing liquids have no simple relation to the ion masses. There is, for example, little difference between the ionic conductivities of electrolytes containing chloride and iodide ions even though the latter have nearly four times the mass of the former.

From (3.218) and (3.220), the flux of ions depends on the ion's absolute mobility M_abs, where the absolute mobility is defined as the ion's speed due to a unit force acting on it [3.247]. In (3.221), the electric force is expressed as acting per ion but may be more conveniently expressed as that acting per mole of ions. Thus M_abs can

relate the limiting speed $\boldsymbol{v}_\mathrm{d}$ to the magnitude of the force per mole $\boldsymbol{f}$

$$\boldsymbol{v}_\mathrm{d} = M_\mathrm{abs}\boldsymbol{f} \,. \tag{3.223}$$

In the case of an electric field, we can express the force per mole as $\boldsymbol{f}_\mathrm{e}$

$$\boldsymbol{f}_\mathrm{e} = z_\mathrm{i}F_\mathrm{a}\boldsymbol{E} \,, \tag{3.224}$$

where z_i is the valence and F_a is the Faraday number and $F_\mathrm{a} = e_0 N_\mathrm{A}$ (Coulomb/mol), N_A is Avogadro's number. Thus $z_\mathrm{i}F_\mathrm{a}$ is the charge per mole of ions and

$$\boldsymbol{v}_\mathrm{d} = M_\mathrm{abs}z_\mathrm{i}F_\mathrm{a}\boldsymbol{E} \,, \tag{3.225}$$

or

$$\boldsymbol{v}_\mathrm{d} = M_\mathrm{e}\boldsymbol{E} \,, \tag{3.226}$$

as in the case where all forces but $\boldsymbol{E}$ can be neglected. Then

$$M_\mathrm{e} = M_\mathrm{abs}z_\mathrm{i}F_\mathrm{a} \,. \tag{3.227}$$

Neither M_abs nor M_e can be conveniently measured but they can be related to the equivalent ionic conductivity λ, which can be measured. To find this relationship, consider a column in the electrolyte solution of length l and of uniform cross-sectional area A. If there is a potential difference V between the ends of the column, it will drive a current I of one ion species through the column. If G is the conductance of the column for that ion species, the current will be given by Ohm's law as

$$I = GV \,. \tag{3.228}$$

The conductance G depends on length and area and is proportional to the specific ionic conductivity σ, so

$$G = \frac{\sigma A}{l} \,. \tag{3.229}$$

The equivalent conductivity λ is obtained by dividing the specific conductivity σ by the ionic concentration in *equivalents*

$$\lambda = \frac{\sigma}{z_\mathrm{i}C_\mathrm{i}} \,, \tag{3.230}$$

where C_i is the concentration in mol/m^3 and $z_\mathrm{i}C_\mathrm{i}$ the concentration in *equivalents*. When the ion concentration tends to zero in a solution, λ tends to λ^0, the limiting equivalent conductivity. The electric field driving the current is the voltage gradient

$$|\boldsymbol{E}| = \frac{V}{l} \,. \tag{3.231}$$

From (3.228) to (3.231), we obtain the electric current

$$I = \lambda z_\mathrm{i}C_\mathrm{i}A|\boldsymbol{E}| \,. \tag{3.232}$$

We can also relate the current to the drift velocity. Since the electric charge per unit volume is, $z_\mathrm{i}C_\mathrm{i}F_\mathrm{a}$, the charge in the column considered is $\rho_\mathrm{e} = z_\mathrm{i}C_\mathrm{i}F_\mathrm{a}Al$. This charge moves out of the column in the time $l/|\boldsymbol{v}_\mathrm{d}|$. Thus the rate of passage of electric charge, which is actually the electric current, is

$$I = \frac{C_\mathrm{i}z_\mathrm{i}F_\mathrm{a}Al}{l/|\boldsymbol{v}_\mathrm{d}|} = C_\mathrm{i}z_\mathrm{i}F_\mathrm{a}A|\boldsymbol{v}_\mathrm{d}| \,. \tag{3.233}$$

Equating the two expressions for the current, (3.232) and (3.233), we have

$$\boldsymbol{v}_\mathrm{d} = \frac{\lambda|\boldsymbol{E}|}{F_\mathrm{a}} \,. \tag{3.234}$$

From (3.226) and (3.234) we express the electric mobility M_e in terms of λ as

$$M_\mathrm{e} = \frac{\lambda}{F_\mathrm{a}} \,, \tag{3.235}$$

whereas from (3.225) and (3.235) the absolute mobility M_abs is related to λ as

$$M_\mathrm{abs} = \frac{\lambda}{z_\mathrm{i}F_\mathrm{a}^2} \quad \text{(for force per ion)} \,, \tag{3.236a}$$

$$M_\mathrm{abs} = \frac{\lambda N_\mathrm{A}}{z_\mathrm{i}F_\mathrm{a}^2} \quad \text{(for force per mole)} \,. \tag{3.236b}$$

The ratio between M_abs of an ion X to M_abs of K^+ (potassium ion) is defined as the relative mobility $M_\mathrm{rel\,X}$ of ion X. Hence, the relative mobility of ion X of valence z_X is given by

$$M_\mathrm{rel\,X} = \frac{\lambda_\mathrm{X}}{z_\mathrm{X}\lambda_\mathrm{K}} \,, \tag{3.237}$$

since z is $+1$ for K^+. Both mobilities must be taken at the same temperature. For a monovalent ion Y, its relative mobility will simply be given by

$$M_\mathrm{rel\,Y} = \frac{\lambda_Y}{\lambda_\mathrm{K}} \,, \tag{3.238}$$

where λ_Y is the equivalent conductivity of Y at the same temperature as for λ_K. Table 3.33 contains the values of the limiting equivalent conductivity λ^0, the relative mobility M_rel, the absolute mobility M_abs and the electric mobility M_e for a number of ions in water at 298.15 K. Table 3.34 shows the dependence of the limiting equivalent conductivity on temperature for a number of ions in water. Tables 3.35 and 3.36 contain the values of λ^0 for

a number of ions in protic and aprotic solvents, respectively. Protic solvents are strong hydrogen donors. For large concentrations the influence of the ions on each other because of proximity must be taken into account.

The Viscous Force Action on an Ion in Solution – The Stokes–Einstein Relation. If asserting the similarity between a macroscopic sphere moving in an incompressible fluid and a particle (ion) moving in a solution, then the calculations for viscous force acting on a macroscopic sphere can be used for that acting on an ion. The value of the viscous force depends on several factors – the velocity $\boldsymbol{v}$ and diameter $d = 2r$ of the sphere (an ion) and the viscosity μ and density ρ of the medium. When the hydrodynamic conditions are such that the Reynolds number (3.239) is much smaller than unity, the viscous force opposing the sphere is given by Stokes' law (3.240).

$$\mathrm{Re} = \frac{|\boldsymbol{v}|d\rho}{\mu} , \tag{3.239}$$

$$\boldsymbol{F}_{\mathrm{Stokes}} = 6\pi r\mu\boldsymbol{v} . \tag{3.240}$$

The net driving force due to the concentration gradient and the external applied force (electric field) produces a steady-state diffusion/conduction flux of ions J for which one can imagine a drift velocity of the diffusing particles. Since the drift velocity is a steady-state velocity, the net driving force ($\boldsymbol{F}_{\mathrm{net}}$) must be opposed by an equal resistive force which can be taken to be the Stokes viscous force. Hence,

$$-\boldsymbol{F}_{\mathrm{net}} = 6\pi r\mu\boldsymbol{v}_{\mathrm{d}} . \tag{3.241}$$

with $\boldsymbol{v}$ being equal to the drift velocity $\boldsymbol{v}_{\mathrm{d}}$.

If we, for example, consider a bath containing a polymer solution in an electric field between two electrodes (like in the electrospinning of polymer solutions), we can estimate the drift velocity of the charge carriers, which is mainly ionic impurities (depending on the polymer and solvent). Using the following values: $|\boldsymbol{E}| = 1\,\mathrm{g}^{1/2}/(\mathrm{cm}^{1/2}\,\mathrm{s})\,(300\,\mathrm{V/cm})$; $e_0 = 4.8\times10^{-10}\,(\mathrm{g}^{1/2}\,\mathrm{cm}^{3/2})/\mathrm{s}$ $(1.6\times10^{-19}\,\mathrm{C})$; $z_{\mathrm{i}} = +1$; $\mu = 10^{-2} - 10\,\mathrm{g/(cm\,s)}$ (1–1000 cP) and $r = 10^{-8}cm$ (typical for small ions such as Cl^-), $|\boldsymbol{v}_{\mathrm{d}}|$ is of the order of 1 cm/s to 10^{-3} cm/s. The value of $|\boldsymbol{v}_{\mathrm{d}}|$ has been estimated from (3.241) with $|\boldsymbol{F}_{\mathrm{net}}| = e_0|\boldsymbol{E}|$. For small ions r is the ionic radius, correct to the order of magnitude [3.236]. The solvation radii [3.246] are one to two orders larger. With the above values and $\rho \sim 1\,\mathrm{g/cm}^3$, one can easily see that $\mathrm{Re} \ll 1$.

From (3.220, 222) and (3.241) we have

$$M_{\mathrm{abs}} = \frac{1}{6\pi r\mu} , \tag{3.242}$$

$$M_{\mathrm{e}} = \frac{z_{\mathrm{i}}e_0}{6\pi r\mu} . \tag{3.243}$$

The mobility given by (3.243) is also called the Stokes mobility.

The Einstein relation between the ion diffusion coefficient D and the absolute mobility M_{abs} is one of the most important relations relevant for the diffusion of ions [3.236]

$$D = M_{\mathrm{abs}}k_{\mathrm{B}}T = \frac{M_{\mathrm{e}}k_{\mathrm{B}}T}{z_{\mathrm{i}}e_0} , \tag{3.244}$$

where k_{B} is the Boltzmann constant and T the temperature.

With the help of (3.242), (3.244) yields

$$D = \frac{k_{\mathrm{B}}T}{6\pi r\mu} , \tag{3.245}$$

Equation (3.245) is the Einstein–Stokes relation and it links the processes of diffusion and viscous flow.

The real question centers on the applicability of Stokes' law to microscopic ions moving in a structured medium in which the surrounding particles are roughly of the same size as the ions.

Mobility Measurements. The *natural* conductivity of dielectric liquids (leaky dielectrics) is generally very small. Therefore, in order to make the measurement of charge mobility easier, it is necessary to enhance the normal charge density in a controlled manner, usually by some form of transient external excitation. The mobility of charge carriers is defined as its drift velocity per unit of electric stress (3.226). An estimate of mobility is achieved by a time-of-flight method, which requires a measure of the time necessary for the charge to travel a known distance in the liquid under the influence of a uniform electric field. A detailed description of various experimental techniques of measurement can be found in [3.248]. A general arrangement for mobility measurements is illustrated in Fig. 3.57 [3.249]. Excess charge is created at the emitter electrode E. By applying the appropriate polarity of voltage V, ions of one sign are swept to the collector electrode C. The emitter electrode is maintained at a high potential relative to earth. The grid pair AB and DF act as electrical shutters, or gates, to allow the passage of carriers across the drift space BD. The gates are arranged to open or close with the frequency of an alternating current (AC) voltage applied to them.

Table 3.33 Experimental values of the limiting equivalent ionic conductivity λ^0, the relative ion mobility M_{rel}, the absolute ion mobility M_{abs} and the electrical ion mobility M_e for a number of different ions in water at 298.15 K. Most of the values were taken from [3.253] and [3.254]. See also [3.246]

Ion	Valence	λ^0 $[(\text{cm}\,\Omega\,\text{equiv.})^{-1}]$	M_{rel}	M_{abs} $(\text{mol}\,\text{s}\,\text{g}^{-1}\times10^9)$	M_e $(\text{cm}^{3/2}\text{g}^{-1/2}\times10^3)$
Acetate	−1	40.866	0.556	4.3907	0.4236
Br	−1	78.1	1.0626	8.3912	0.8095
Cl	−1	76.35	1.0388	8.2032	0.7914
ClO_4	−1	67.326	0.916	7.2336	0.6979
F	−1	55.4	0.7537	5.9523	0.5742
HCO_3	−1	44.4675	0.605	4.7777	0.4609
I	−1	76.8	1.0449	8.2515	0.7961
NO_3	−1	71.46	0.9722	7.6778	0.7407
OH	−1	198.3	2.698	21.3057	2.0555
Ag	1	61.9	0.8422	6.6506	0.6416
Cs	1	77.2	1.0503	8.2945	0.8002
H	1	350.0805	4.763	37.6133	3.6287
K	1	73.5	1.0	7.8970	0.7619
Li	1	38.6	0.5252	4.1473	0.4001
Na	1	50.1	0.6816	5.3828	0.5193
NH_4	1	73.5	1.0	7.8970	0.7619
Rb	1	77.8365	1.059	8.3629	0.8068
SO_4	−2	80.0	0.5442	4.2977	0.8292
Ba	2	63.798	0.434	3.4273	0.6613
Ca	2	59.5	0.4048	3.1964	0.6167
Cd	2	54.39	0.37	2.9219	0.5638
Co	2	54.39	0.37	2.9219	0.5638
Cu	2	53.655	0.365	2.8824	0.5562
Fe	2	54.39	0.37	2.9219	0.5638
Hg	2	63.651	0.433	3.4194	0.6598
Mg	2	53.0	0.3605	2.8472	0.5494
Mn	2	53.508	0.364	2.8745	0.5546
Ni	2	49.539	0.337	2.6613	0.5135
Pb	2	70.56	0.48	3.7905	0.7314
Sr	2	59.388	0.404	3.1904	0.6156
Zn	2	52.773	0.359	2.8350	0.5470
Fe	3	67.914	0.308	2.4323	0.7040
Gd	3	67.2525	0.305	2.4086	0.6971
La	3	69.678	0.316	2.4954	0.7222

If this frequency is changed continuously, the number of ions reaching C is a maximum when their transit time between the gates is equal to, or an integral multiple of, the period of the pulses. The variation in the collector current is shown in Fig. 3.57b, where the transit time is given by the reciprocal of the difference in frequencies corresponding to adjacent current maxima. The amplitude of the oscillations tends to fall as the frequency of the gate voltage is raised with the result that the sensitivity of the method is decreased as the drift distance is increased and the transit time shortened. *Meyer* and *Reif* [3.250] used this method for fields up to 25 kV/m in liquid helium. *Schynders* et al. [3.251, 252] used this method to determine the electron mobilities in liquid ar-

Table 3.34 Experimental values of the limiting equivalent conductivity λ^0 of ions in water at various temperatures. The units are $(\text{cm}\Omega\text{equiv.})^{-1}$. For a more complete set of data [3.246]

Ion	Valence	Temperature (K)			
		273.15	288.15	298.15	308.15
Br^-	−1	42.6	63.1	78.1	94
Cl^-	−1	41	61.4	76.35	92.2
I^-	−1	41.4	62.1	76.8	92.3
Cs^+	1	44	63.1	77.2	92.1
K^+	1	40.7	59.6	73.5	88.2
Li^+	1	19.4	30.2	38.6	48
Na^+	1	26.5	39.7	50.1	61.5
Ca^{++}	2	31.2	46.9	59.5	73.2

Table 3.35 Limiting ionic conductivities λ^0 $(\text{cm}\Omega\text{equiv.})^{-1}$ in protic solvents at 298.15 K [3.255]. MeOH – Methanol, EtOH – Ethanol, PrOH – Propane alcohol, BuOH – Butane alcohol, HCOOH – Formic acid

Ion	Valence	MeOH	EtOH	PrOH	BuOH	HCOOH
Ag	+1	50.07				
Br	−1	56.43	23.88	12.22	8.23	28.3
Cl	−1	52.09	21.87	10.45	7.76	26.52
Cs	+1	61.33	26.46			
I	−1	62.62	27.0	13.81	9.52	–
K	+1	47.78	22.2	6.88		23.99
Li	+1	39.08	17.07		8.1	19.36
Na	+1	45.08	20.37	8.35		20.97
NH_4	+1				6.68	27.01
NO_3	−1	61.13	–	–	–	–

gon. Additional information on mobility measurements can be found in Chap. 21 of the Handbook.

3.7.4 Broadband Measurement of the Conductivity and Dielectric Constant

In order to measure the conductivity σ and dielectric constant ε_r of a fluid, the apparatus shown in Fig. 3.58 can be used. It consists of a glass syringe with two brass pistons as the electrodes. Electrode 1 is connected to a linear translation stage that enables accurate setting of the distance L between the electrodes. Electrode 2 is fixed close to a small hole in the glass syringe through which the test fluid can escape when the distance between the electrodes is changed.

The real $\text{Re}(Z)$ and imaginary $\text{Im}(Z)$ components of the complex impedance (Z) of the volume between the

Table 3.36 Limiting ionic conductivities λ^0 $(\text{cm}\Omega\text{equiv.})^{-1}$ in some aprotic solvents at 298.15 K [3.255]. DMF – dimethylformamide, DMSO – dimethylsulfoxide, NMT – monomethyltryptamine, NMA – monomethylacetamide, ACN – acetonitrile

Ion	Valence	DMF	DMSO	NMT	NMA	ACN
Ag	+1	35.2				86.0
Br	−1	53.6	24.1	62.9	11.72	100.7
Cl	−1	55.1	24.4	62.7	10.6	
Cs	+1		16.1			87.3
I	−1	52.3	23.8		13.42	102.1
K	+1	30.8	14.7		7.28	83.6
Li	+1	25.0	11.4		5.65	
Na	+1	29.9	14.54		7.19	76.9
NH_4	+1	38.7				
NO_3	−1	57.3				106.4

electrodes are measured at different frequencies (f) and different distances (L) with the aid of a spectrum analyzer [3.256]. The results of the typical used to find σ and ε_r are shown in Fig. 3.59 for an aqueous solution of polyethylene oxide. In order to determine the values of σ and ε_r, a model, consisting of resistors and capacitors that simulates the impedance of the test fluid is constructed. For the above solution the model shown in Fig. 3.60 is appropriate. The impedance of the circuit shown in Fig. 3.60 is given by

$$Z = \frac{R}{1 + i\omega RC}\,, \tag{3.246}$$

where R is resistance, C capacitance and ω the angular frequency. The real and imaginary parts of (3.246), given in (3.247), should correspond to the measured values of

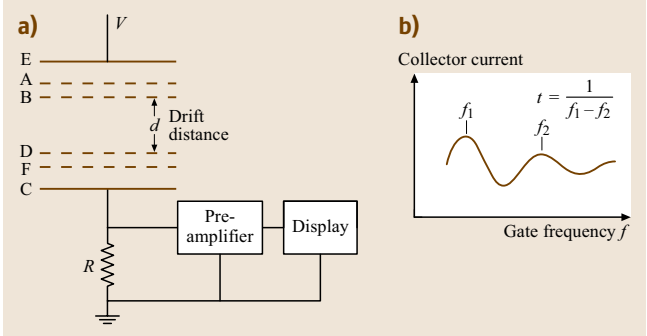

Fig. 3.57 **(a)** Diagram of double gate arrangement for mobility measurement, and **(b)** collector current as a function of the frequency of the voltage on the gates (after [3.249])

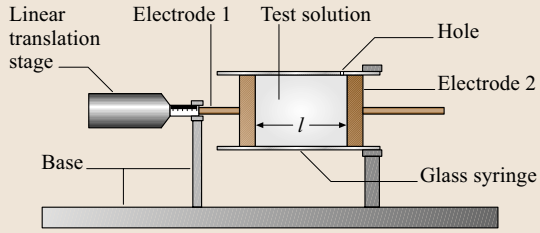

Fig. 3.58 An apparatus for measuring the electric conductivity and dielectric constant of a fluid

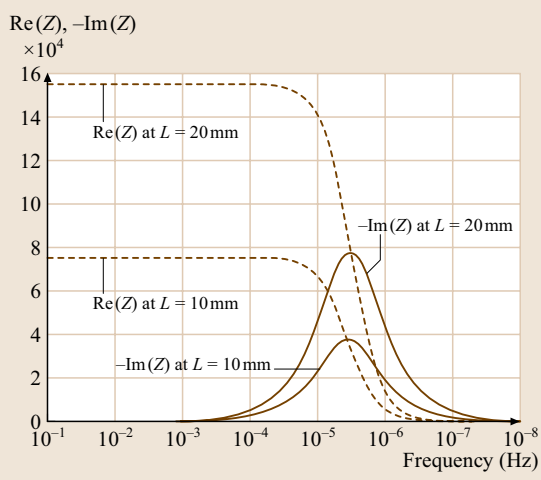

Fig. 3.59 A plot of the real Re(Z) and imaginary Im(Z) parts of the complex impedance of the fluid between the electrodes of the apparatus in Fig. 3.58. The fluid between the electrodes was an aqueous solution of polyethylene oxide: PEO (molecular weight = 4×10^6) at 1% weight concentration in ethanol/water (40/60)

Re(Z) and Im(Z):

$$\mathrm{Re}(Z) = \frac{R}{1+\omega^2R^2C^2}\,, \tag{3.247a}$$

$$\mathrm{Im}(Z) = \frac{-\omega R^2 C}{1+\omega^2R^2C^2}\,, \tag{3.247b}$$

The equations for Re(Z) and Im(Z) as a function of ω are fitted to the experimental data shown in Fig. 3.59 in order to find the values of R and C. With the values of R and C known, σ and ε_r can be calculated from

$$\sigma = \frac{L}{RS}\,, \tag{3.248a}$$

$$\varepsilon_r = \frac{CL}{\varepsilon_0 S}\,, \tag{3.248b}$$

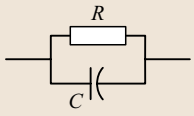

Fig. 3.60 A model that simulates the impedance of the test fluid in Fig. 3.59

where S is the surface area of the electrodes and L is the length of the sample fluid. Table 3.37 shows the values of σ and ε_r for a number of polymer solutions and pure solvents (leaky dielectrics) obtained by this method. The following notation is used: PAA for polyacrylic acid, PVA for polyvinyl alcohol, PU for polyurethane, PCL for polycaprolactone, MC for methylene chloride, DMF for dimethylformamide, and THF for tetrahydrofuran.

The electrical conductivity is a function of the electron and ion motion. In the solutions and solvents tested ion diffusion mainly determines the conductivity of the solution and the electron conductivity is much smaller. When measuring the parameters of an electrically con-

Table 3.37 Representative values of ε_r and σ obtained with the method described in this section

Polymer	ε_r	σ (mS/m)
2% PEO $M_w = 6\times10^5$ in ethanol/water (40/60)	67.09	0.85
2% PEO $M_w = 10^6$ in ethanol/water (40/60)	66.71	0.81
1% PEO $M_w = 4\times10^6$ in ethanol/water (40/60)	66.12	1.102
2% PEO $M_w = 10^6$ in water	81.96	9.43
6% PAA $M_w = 2.5\times10^5$ in ethanol/water (40/60)	79.5	24.47
6% PVA $M_w = 10^4$ in ethanol/water (50/50)	65.99	3.73
6% PU tecoflex in THF/ethanol (50/50)	16.75	0.093
8% PCL $M_w = 8\times10^4$ in acetone	25.2	0.142
10% PCL $M_w = 8\times10^4$ in MC/DMF (75/25)	18.55	0.191
Distilled water	88.75	0.447
Ethanol (95%)	24.55	0.0624
Acetone	20.7	0.0202
Ethanol/water (40/60)	69.47	0.150
MC/DMF (40/60)	29.82	0.505
MC/DMF (75/25)	21.3	0.273
THF/ethanol (50/50)	15.79	0.037

ducting medium (a leaky dielectric), the migration of ions in the high-frequency field causes energy to be drawn from the circuit, damping the oscillation response. In circuit terms, the electrodes and the volume between them are analogous to a capacitor with a resistor in parallel. When the resistance across the electrodes is large, the capacitance derived from the frequency response is close to the true capacitance of the medium between the electrodes. As the resistance across the electrodes is reduced, due to increased ionic conductivity, the oscillator is damped and the oscillation frequency falls. The apparent capacitance thus appears greater than the true capacitance. The effect of ionic conductivity on the permittivity measurement can be neglected below $\sigma = 0.8\,\mathrm{S/m}$ [3.257]. Some other methods of measurement of the dielectric constant and electric conductivity are described in [3.258–262] and in Chap. 21 of the Handbook.

References

3.1 C. Yokohama, S. Takahashi: Saturated liquid densities of 2,2-dichloro-1,1,1-trifluoroethane (HCFC-123), 1,2-dichloro-1,2,2-trifluoroethane (HCFC-123a), 1,1,1,2-tetrafluoroethane (HFC-134a) and 1,1,1-trifluoroethane (HFC-143a), Fluid Phase Equilibr. **67**, 227–240 (1991)

3.2 W.R. Lau, C.-A. Hwang, H.B. Brugge, G.A. Iglesias-Silva, H.A. Duarte-Garza, W.J. Rogers, K.R. Hall, J.C. Holste, B.E. Gammon, K.N. Marsh: A continuously weighed pycnometer for measuring fluid properties, J. Chem. Eng. Data **42**, 738–744 (1997)

3.3 J.R.S. Machado, W.B. Street: Equation of state and thermodynamic properties of liquid methanol from 298 to 489 K and pressures to 1040 bars, J. Chem. Eng. Data **28**, 218–223 (1983)

3.4 H. Kubota, Y. Tanaka, T. Makita, H. Kashiwagi, M. Noguchi: Thermodynamic properties of 1-chloro-1,2,2,2-tetrafluoroethane (R124), Int. J. Thermophys. **9**, 85–101 (1988)

3.5 Y. Sato, T. Nishizuka, K. Hara, T. Yamamura, Y. Waseda: Density measurement of molten silicon by a pycnometric method, Int. J. Thermophys. **21**, 1463–1471 (2000)

3.6 A.R.H. Goodwin, C.H. Braddsell, L.S. Toczylkin: (P, ρ, T) of liquid *n*-octane obtained with a spherical pycnometer at temperatures of 298.03 K and 313.15 K and pressures in the range 0.7 MPa to 32 MPa, J. Chem. Thermodyn. **28**, 637–646 (1996)

3.7 V.N. Belonenko, V.M. Troitsky, Y.E. Belyaev, J.H. Dymond, N.F. Glen: Application of micro (*P*, *V*, *T*) apparatus for measurement of liquid densities at pressures up to 500 MPa, J. Chem. Thermodyn. **32**, 1203–1219 (2000)

3.8 C.M.M. Duarte, H.J.R. Guedes, M. da Nunes Ponte: (*P*, $V - m$, *T*) measurements on liquid and gaseous mixtures near the critical point – I. (xenon + ethane), J. Chem. Thermodyn. **32**, 877–889 (2000)

3.9 E.S. Burnett: Compressibility determinations without volume measurements, J. Appl. Mech. A **3**, 136–140 (1936)

3.10 C.E. Stouffer: *Densities of mixtures of carbon dioxide and hydrogen sulfide from 200 to 450 K to 23 MPa by the Burnett-isochoric method. Ph.D. Thesis* (Texas A&M University, College Station, Texas, USA 1992)

3.11 J.D. Isdale, J.H. Dymond, T.A. Brawn: Viscosity and density of *n*-hexane-cyclohexane mixtures between 25 and 100 °C up to 500 MPa, High Temp.-High Press. **11**, 571–580 (1979)

3.12 J.H. Dymond, J.D. Isdale, N.F. Glen: Density measurement at high pressure, Fluid Phase Equilibr. **20**, 305–314 (1985)

3.13 A. Iso, M. Uematsu: Thermodynamic properties of 1,1-difluoroethane in the super-critical and high-density regions, Physica A **156**, 454–466 (1989)

3.14 J.G. Webster: *Mechanical Variables Measurement: Solid, Fluid and Thermal* (CRC, London 2000)

3.15 V. Hynek, M. Obsil, V. Majer, J. Quint, J.-P.E. Grolier: A vibrating-tube flow densitometer for measurements with corrosive solutions at temperatures up to 723 K and pressures up to 40 MPa, Int. J. Thermophys. **18**, 719–732 (1997)

3.16 A.A.H. Padua, J.M.N.A. Fareleira, J.C.G. Calado, W.A. Wakeham: A vibrating-wire densimeter for liquids at high pressures: The density of 2,2,4-trimethylpentane from 298.15 to 348.15 K and up to 100 MPa, Int. J. Thermophys. **15**, 229–243 (1994)

3.17 J.G. Blencoe, S.E. Drummond, J.C. Seitz, B.E. Nesbitt: A vibrating-tube densimeter for fluids at high pressures and temperatures, Int. J. Thermophys. **17**, 179–190 (1996)

3.18 D.R. Defibaugh, G. Morrison: Compressed liquid densities and saturation densities of chlorodifluoromethane (R22), J. Chem. Eng. Data **37**, 107–110 (1992)

3.19 A.T. Sousa, C.A. Nieto de Castro, R. Tufeu, B. Le Neindre: Density of 1-chloro-1, 1-difluoroethane (R142b), High Temp.-High Press. **24**, 185–194 (1992)

3.20 J. Klimeck, R. Kleinrahn, W. Wagner: An accurate single-sinker densimeter and measurements of the (P, ρ, T) relation of argon and nitrogen in the temperature range from (235 to 520) K at pressures up to 30 MPa, J. Chem. Thermodyn. **30**, 1571–1588 (1998)

3.21 T. Retsina, S.M. Richardson, W.A. Wakeham: The theory of a vibrating-rod densimeter, Appl. Sci. Res. **43**, 127–143 (1986)

3.22 A.R.H. Goodwin, K.N. Marsh, W.A. Wakeham (Eds.): *IUPAC Experimental Thermodynamics Vol. VI. Measurement of the Thermodynamic Properties of Single Phases* (Elsevier, Amsterdam 2003)

3.23 M. Dix, J.M.N.A. Fareleira, Y. Takaishi, W.A. Wakeham: A vibrating wire densimeter for measurements in fluids at high pressures, Int. J. Thermophys. **12**, 357–370 (1991)

3.24 A.A.H. Padua, J.M.N.A. Fareleira, J.C.G. Calado, W.A. Wakeham: Electromechanical model for vibrating-wire instruments, Rev. Sci. Instrum. **69**, 2392–2399 (1998)

3.25 F. Audonnet, A.A.H. Padua: Simultaneous measurements of density and viscosity of *n*-pentane fom 298 K to 383 K and up to 100 MPa pressure using a vibrating-wire instrument, Fluid Phase Equilibr. **181**, 147–161 (2001)

3.26 R. Kleinrahm, W. Wagner: Measurement and correlation of the equilibrium liquid and vapor densities and the vapor pressure along the coexistance curve of methane, J. Chem. Thermodyn. **18**, 739–760 (1986)

3.27 C. Evers, H.W. Losch, W. Wagner: An absolute viscometer-densimeter and measurements of the viscosity of nitrogen, methane, helium, neon, argon, and krypton over a wide range of density and temperature, Int. J. Thermophys. **23**, 1411–1439 (2002)

3.28 R. Masui: Development of a magnetic suspension densimeter and measurement of the density of toluene, Int. J. Thermophys. **23**, 921–935 (2002)

3.29 S. Toscani, P. Figuiere, H. Szwarc: A magnetic suspension apparatus to measure densities of liquids as a function of temperature at pressures up to 100 MPa. Application to *n*-heptane, J. Chem. Thermodyn. **21**, 1263–1277 (1989)

3.30 M. Okada, N. Uemastsu, K. Watanabe: Orthobaric liquid densities of trichloro-fluoromethane, dichlorodifluoromethane, chlorodifluoromethane, 1,1,2-trichloro-trifluoroethane, 1,2-dichlorotetrafluoroethane, and of the azeotropic mixture of (chlorodifluoromethane + chloropentafluoroethane) between 203 and 463 K, J. Chem. Thermodyn. **18**, 527–543 (1986)

3.31 W. Wagner, A. Pruß: The IAPWS formulation 1995 for the thermodynamic properties of ordinary water substance for general and scientific use, J. Phys. Chem. Ref. Data **31**, 387–535 (2002)

3.32 http://www.iapws.org/

3.33 M.J. Assael, J.H. Dymond, D. Exadaktilou: An improved representation of the density of *n*-alkane liquid densities, Int.J. Thermophys. **15**, 155–164 (1994)

3.34 M.J. Assael, J.H. Dymond, P.M. Patterson: Correlation and prediction of dense fluid transport coefficients – V. Aromatic Hydrocarbons, Int. J. Thermophys. **13**, 895–905 (1992)

3.35 M.J. Assael, J.H. Dymond, S.K. Polimatidou: Correlation and prediction of dense fluid transport coefficients – VI. *n*-Alcohols, Int. J. Thermophys. **15**, 189–201 (1994)

3.36 M.J. Assael, J.H. Dymond, S.K. Polimatidou: Correlation and prediction of dense fluid transport coefficients – VII. Refrigerants, Int. J. Thermophys. **16**, 761–772 (1995)

3.37 Supertrapp Ver. 2.0, Computer Software Package for the calculation of the transport properties of nonpolar fluids and their mixtures (N.I.S.T., Gaithersburg 1998)

3.38 K.A. Connors, J.L. Wright: Dependence of surface tension on composition of binary aqueous-organic solutions, Anal. Chem. **61**, 194–198 (1989)

3.39 L.A. Girifalco, R.J. Good: A theory for the estimation of surface and interfacial energies – I. Derivation and application to interfacial tension, J. Phys. Chem. **61**, 904–909 (1957)

3.40 F.M. Fowkes: Dispersion force contributions to surface and interfacial tensions, contact angles, and heats of immersion. In: *Contact Angle, Wettability, and Adhesion*, Adv. Chem. Ser., Vol. 43, ed. by R.F. Gould (ACS, Washington 1964) pp. 99–111

3.41 D.K. Owens, R.C. Wendt: Estimation of the surface free energy of polymers, J. Appl. Polym. Sci. **13**, 1741–1747 (1969)

3.42 J.J. Jasper: The surface tension of pure liquid compounds, J. Phys. Chem. Ref. Data **1**, 841–1009 (1972)

3.43 N.B. Vargaftik, Y.K. Vinogradov, V.S. Yargin: *Handbook of Physical Properties of Liquids and Gases: Pure Substances and Mixtures* (Begell House, New York 1996)

3.44 A. Marmur: Wetting on hydrophobic rough surfaces: to be heterogeneous or not to be?, Langmuir **19**, 8343–8348 (2003)

3.45 E.L. Decker, S. Garoff: Using vibrational noise to probe energy barriers producing contact angle hysteresis, Langmuir **12**, 2100–2110 (1996)

3.46 C. Andrieu, C. Sykes, F. Brochard: Average spreading parameter on heterogeneous surfaces, Langmuir **10**, 2077–2080 (1994)

3.47 H. Kamusewitz, W. Possart, D. Paul: The relation between Young's equilibrium contact angle and the hysteresis on rough paraffin wax surfaces, Colloid. Surf. A Physiochem. Eng. Aspects **156**, 271–279 (1999)

3.48 T.D. Blake, A. Clarke, K.J. Ruschak: Hydrodynamic assist of dynamic wetting, AIChE J. **40**, 229–242 (1994)

3.49 T.D. Blake, M. Bracke, Y.D. Shikhmurzaev: Experimental evidence of non-local hydrodynamic influence on the dynamic contact angle, Phys. Fluids **11**, 1995–2007 (1999)

3.50 T.D. Blake: Dynamic contact angles and wetting kinetics. In: *Wettability*, ed. by J.C. Berg (Marcel Dekker, New York 1993) pp. 251–309

3.51 M.J. de Ruijter, J. De Coninck, T.D. Blake, A. Clarke, A. Rankin: Contact angle relaxation during the spreading of partially wetting drops, Langmuir **13**, 7293–7298 (1997)

3.52 O.V. Voinov: Hydrodynamics of wetting, Fluid Dyn. **11**, 714–721 (1976)
3.53 E.B.V. Dussan: The moving contact line: the slip boundary condition, J. Fluid Mech. **77**, 665–684 (1976)
3.54 L.H. Tanner: The spreading of silicone oil drops on horizontal surfaces, J. Phys. D **12**, 1473–1484 (1979)
3.55 R.G. Cox: The dynamics of the spreading of liquids on a solid surface, J. Fluid Mech. **168**, 169–194 (1986)
3.56 P.G. de Gennes: Wetting statics and dynamics, Rev. Modern Physics **57**, 827–863 (1985)
3.57 S.F. Kistler: Hydrodynamics of wetting. In: *Wettability*, ed. by J.C. Berg (Marcel Dekker, New York 1993) pp. 311–429
3.58 B.W. Cherry, C.M. Holmes: Kinetics of the wetting of surfaces by polymers, J. Colloid Interface Sci. **29**, 174–176 (1969)
3.59 T.D. Blake, J.M. Haynes: Kinetics of liquid/liquid displacement, J. Colloid Interface Sci. **30**, 421–423 (1969)
3.60 M.J. de Ruijter, T.D. Blake, J. De Coninck: Dynamic wetting studied by molecular modeling simulations of droplet spreading, Langmuir **15**, 7836–7847 (1999)
3.61 P.G. Petrov, P.G. Petrov: A combined molecular-hydrodynamic approach to wetting kinetics, Langmuir **8**, 1762 (1992)
3.62 F. Brochard-Wyart, P.G. de Gennes: Dynamics of partial wetting, Adv. Colloid Interface Sci. **39**, 1–11 (1992)
3.63 M. de Ruijter, G. Oshanin, J. De Coninck: Droplet spreading: partial wetting regime revisited, Langmuir **15**, 2209–2216 (1999)
3.64 M. de Ruijter, M. Charlot, M. Voué, J. De Coninck: Experimental evidence of several time scales in drop spreading, Langmuir **16**, 2363–2368 (2000)
3.65 Y.D. Shikhmurzaev: Moving contact lines in liquid/liquid/solid systems, J. Fluid Mech. **334**, 211–249 (1997)
3.66 T.D. Blake, Y.D. Shikhmurzaev: Dynamic wetting by liquids of different viscosity, J. Colloid Interface Sci. **253**, 196–202 (2002)
3.67 M. de Ruijter: *A microscopic approach to partial wetting: statics and dynamics. Ph.D. Thesis* (University of Mons-Hainaut, Mons-Hainaut 1996)
3.68 R.L. Hoffman: A study of the advancing interface – 1. Interface shape in liquid-gas systems, J. Colloid Interface Sci. **50**, 228–241 (1975)
3.69 E.B.V. Dussan: On the spreading of liquids on solid surfaces: static and dynamic contact lines, Annu. Rev. Fluid Mech. **11**, 371–400 (1979)
3.70 T.D. Blake, K.J. Ruschak: Wetting: static and dynamic contact lines. In: *Liquid Film Coating*, ed. by S.F. Kistler, P.M. Schweizer (Chapman Hall, London 1997) pp. 63–97
3.71 A. Clarke, T.D. Blake, K. Carruthers, A. Woodward: Spreading and imbibition of liquid droplets on porous surfaces, Langmuir **18**, 2980–2984 (2002)
3.72 E. Ramé, S. Garoff: Microscopic and macroscopic dynamic interface shapes and interpretation of dynamic contact angles, J. Colloid Interface Sci. **177**, 234–244 (1996)
3.73 R. Burley, B.S. Kennedy: An experimental study of air entrainment at a solid/liquid/gas interface, Chem. Eng. Sci. **31**, 901–911 (1976)
3.74 A. Clarke: The application of particle tracking velocimetry and flow visualisation to curtain coating, Chem. Eng. Sci. **50**, 2397–2407 (1995)
3.75 T.D. Blake, A. Clarke, E.H. Stattersfield: An investigation of electrostatic assist in dynamic wetting, Langmuir **16**, 2928–2935 (2000)
3.76 NIH Image: http://rsb.info.nih.gov/nih-image/ or for further possibilities see http://www.efg2.com/Lab/Library/ImageProcessing/
3.77 W.H. Press, S.A. Teukolsky, W.T. Vetterling, B.P. Flannery: *Numerical Recipes in Fortran*, 2nd edn. (Cambridge Univ. Press, Cambridge 1992)
3.78 R.A. Hayes, J. Ralston: Forced liquid movement on low energy surfaces, J. Colloid Interface Sci. **159**, 429–438 (1993)
3.79 E.V. Gribanova, L.I. Molchanova: Dependence of wetting angle on rate of meniscus movement, Kolloidn. Zh. **40**, 217–223 (1978)
3.80 J.W. Berube, C.B. Schriver, D.H. Chittenden: Photomicrography of a rapidly moving meniscus, Ind. Eng. Chem. Fundam. **12**, 236–239 (1973)
3.81 M. Fermegier, P. Jenffer: An experimental investigation of the dynamic contact angle in liquid-liquid systems, J. Colloid Interface Sci. **146**, 226–241 (1991)
3.82 G. Martic, F. Gentner, D. Sevano, D. Coulon, J. De Coninck, T.D. Blake: A molecular dynamics simulation of capillary imbibition, Langmuir **18**, 7971–7976 (2002)
3.83 W.A. Wakeham, A. Nagashima, J.V. Sengers (Eds.): *Experimental Thermodynamics, Measurement of the Transport Properties of Fluids*, Vol. III (Blackwell, Oxford 1991)
3.84 G.F. Newell: Theory of oscillating type viscometer – V. Disk oscillating between fixed plates, Z. Angew. Math. Phys. **10**, 160–175 (1959)
3.85 J. Kestin, W. Leidenfrost: *Thermodynamic and Transport Properties of Gases, Liquids and Solids*, ed. by Y.S. Touloukian (ASME McGraw-Hill, New York 1959)
3.86 E. Vogel: Konstruction eines Quarzglas-Schwingscheibenviskosimeters und Messungen an Stickstoff und Argon, Wiss. Z. Univ. Rostock **21**, 169–179 (1972), in German
3.87 J. Kestin, S.T. Ro, W.A. Wakeham: Viscosity of isotopes of hydrogen and their intermolecular potential, J. Chem. Soc. Faraday Trans. I **68**, 2316–2323 (1972)
3.88 J. Kestin, O. Korfali, J.V. Sengers: Density expansion of the viscosity of carbon dioxide near the critical temperature, Physica **100A**, 335–348 (1980), 335–348

3.89 R. Di Pippo, J. Kestin, J.W. Whitelaw: A high temperature oscillating-disk viscometer, Physica **32**, 2064–2078 (1966)

3.90 J. Kestin, H.E. Khalifa, W.A. Wakeham: Viscosity of 5 gaseous hydrocarbons, J. Chem. Phys. **66**, 1132–1134 (1977)

3.91 G. Oltermann: *Messung der Viskosität von Wasserdampf in der Nähe des kritischen Zustandes. Ph.D. Thesis* (University of Hannover, Hannover 1977), in German

3.92 J. Kestin, R. Paul, I.R. Shankland, H.E. Khalifa: A high-temperature, high-pressure oscillating-disk viscometer for concentrated ionic solutions, Ber. Bunsenges. Phys. Chem. **84**, 1255–1265 (1980)

3.93 K. Torklep, H.A. Oye: An absolute oscillating-cylinder (or cup) viscometer for high pressures, J. Phys. E **12**, 875–885 (1979)

3.94 D.A. Beckwith, G.F. Newell: Theory of oscillating-type viscometers – II. Oscillating-cup, J. Ang. Math. Phys. **8**, 450–465 (1957)

3.95 J.M. Grouvel, J. Kestin, H.E. Khalifa, E.U. Franck, F. Hensel: Viscosity of liquid mercury from 20 °C to 260 °C along the saturation line, Ber. Bunsenges. Phys. Chem. **81**, 338–344 (1977)

3.96 H.V. Tippelskirch, E.U. Franck, F. Hensel, J. Kestin: Viscosity of fluid mercury to 1529 K and 100 bar, Ber. Bunsenges. Phys. Chem. **79**, 889–897 (1975)

3.97 Y. Abe, O. Kosugiyama, A. Nagashima: Viscosity measurements of NaCl in the temperature range 1083 to 1473 K, Ber. Bunsenges. Phys. Chem. **84**, 1178–1184 (1980)

3.98 B. Knapstad, P.A. Skjolsvik, H.A. Oye: Viscosity of pure hydrocarbons, J. Chem. Eng. Data **34**, 37–43 (1989)

3.99 D. Dumas, K. Grjotheim, B. Hogdahl, H.A. Oye: Theory of oscillating bodies and its utilization for determination of high-temperature viscosities, Acta Chem. Scand. **24**, 510–530 (1970)

3.100 W. Brockner, K. Grjotheim, K. Ohta, H.A. Oye: High temperature viscometer for liquids – 2 Viscosity of alkali chlorides, Ber. Bunsenges. Phys. Chem. **79**, 344–347 (1975)

3.101 J.T. Tough, W.D. McCormick, J.G. Dash: Viscosity of liquid He II, Phys. Rev. **132**, 2373–2378 (1963)

3.102 T. Retsina, S.M. Richardson, W.A. Wakeham: The theory of a vibrating-rod viscometer, Appl. Sci. Res. **43**, 325–346 (1987)

3.103 S.S. Chen, M.W. Wambsganaa, J.A. Jendrzejczyk: Added mass and damping of a vibrating rod in confined viscous fluids, Trans. ASME, J. Appl. Mech. **43**, 315–332 (1976)

3.104 M.J. Assael, M. Papadaki, M. Dix, S.M. Richardson, W.A. Wakeham: An absolute vibrating-wire viscometer for liquids at high pressures, Int. J. Thermophys. **12**, 231–244 (1991)

3.105 C.M.B.P. Oliveira: *Viscosity of liquid hydrocarbons at high pressure. Ph.D. Thesis* (London University, London 1991)

3.106 J. Wilhelm, E. Vogel: Viscosity measurements on gaseous propane, J. Chem. Eng. Data **46**, 1467–1471 (2001)

3.107 J.L.G.C. da Mata, J.M.N.A. Fareleira, C.M.B.P. Oliveira, F.J.P. Caetano, W.A. Wakeham: A new instrument to perform simultaneous measurements of density and viscosity of fluids by a dual vibrating-wire technique, High Temp.-High Press. **33**, 669–676 (2001)

3.108 P.S. van der Gulik, R. Mostert, H.R. van den Berg: The viscosity of methane at 25 °C up to 10 kBar, Physica **151A**, 153–165 (1988)

3.109 W.P. Mason: Measurement of the viscosity and shear elasticity of liquids by means of a torsionally vibrating crystal, Trans. ASME **69**, 359–370 (1947)

3.110 B. Welber: Damping of a torsional oscillating cylinder in liquid helium at various temperatures and densities, Phys. Rev. **119**, 1816–1822 (1960)

3.111 W.M. Haynes: Viscosity of gaseous and liquid argon, Physica **67**, 440–470 (1973)

3.112 D.E. Diller, N.V. Frederick: Torsional piezoelectric crystal viscometer for compressed gases and liquids, Int. J. Thermophys. **10**, 145–157 (1989)

3.113 B. Bode: *Entwicklung eines Quarzviskosimeters für Messungen bei hohen Drucken. Ph.D. Thesis* (Technical University Clausthal, Clausthal 1984)

3.114 F.J.V. dos Santos, C.A. Nieto de Castro: Viscosity of toluene and benzene under high presure, Int. J. Thermophys. **18**, 367–382 (1997)

3.115 G. Barr: *A Monograph of Viscometry* (Oxford Univ. Press, Oxford 1931)

3.116 J. Kestin, M. Sokolov, W.A. Wakeham: Theory of capillary viscometers, Appl. Sci. Res. **27**, 241–264 (1973)

3.117 J.F. Swindells, J.R. Coe Jr., T.B. Godfrey: Absolute viscosity of water at 20 °C, J. Res. Nat. Bur. Standards **48**, 1–31 (1952)

3.118 M. Kawata, K. Kurase, K. Yoshida: *Realization of a viscosity standard*, Proceedings of 5-th International Congress on Rheology, Vol. 1 (University of Tokyo Press, Tokyo 1969)

3.119 N.J. Trappeniers, A. Botzen, H.R. van den Berg, J. van Oesten: The viscosity of neon between 25 °C and 75 °C at pressures up to 1800 atm, Corresponding states for the viscosity of the noble gases up to high densities, Physica **30**, 985–996 (1964)

3.120 A. Nagashima, I. Tanishita: Viscosity measurement of water and steam at high temperature and high pressures, Bull. JSME **12**, 1467–1478 (1969)

3.121 S.L. Rivkin, A.Y. Levin, L.B. Izrailevskii, K.G. Kharistonov: Experimental investigation of the viscosity of heavy water at temperatures of 200–375 °C and pressures up to 500 Bar, Thermal Eng. **19**, 130–134 (1972), English translation of Teploenergetika

3.122 F.A. Guevara, B.B. McInteer, W.E. Wageman: High temperature viscosity ratios for hydrogen, helium, argon and nitrogen, Phys. Fluids **12**, 2493–2505 (1969)

3.123 T. Ejima, K. Shimakage, Y. Sato, H. Okuda, N. Kumada, A. Ishigaki: Viscosity measurements of

alkali chlorides with capillary viscometers, Nihon-Kagaku-Kaishi **6**, 961–968 (1982)
3.124 J.D. Isdale: *Viscosity of simple liquids including measurement and prediction at elevated pressure. Ph.D. Thesis* (University of Strathclyde, Strathclyde 1976)
3.125 J.B. Irving: *Viscosity measurements at pressures up to 14000 bar using an automatic falling cylinder viscometer. Ph.D. Thesis* (University of Glasgow, Glasgow 1980)
3.126 H. Faxen: Die Bewegung einer starren Kugel längs der Achse eines mit zäher Flüssigkeit gefüllten Rohres, Arkiv. Matematik. Astron. Fys. **17**, 1–28 (1923), in German
3.127 M.J.C. Flude, J.E. Daborn: Viscosity measurements by means of falling spheres compared with capillary viscometers, J. Phys. E **15**, 1312–1321 (1982)
3.128 N.F. Glen: *Viscosity coefficient measurement at elevated pressure. Ph.D. Thesis* (University of Glasgow, Glasgow 1983)
3.129 J. Kestin, M. Sokolov, W.A. Wakeham: Viscosity of liquid water in range 8 to 150 °C, J. Phys. Chem. Ref. Data **7**, 941–948 (1978)
3.130 M.J. Assael, J.H. Dymond, M. Papadaki, P.M. Patterson: Correlation and prediction of dense fluid transport coefficients – I. *n*-Alkanes, Int. J. Thermophys. **13**, 269–281 (1992)
3.131 M.J. Assael, J.H. Dymond, P.M. Patterson: Correlation and prediction of dense fluid transport coefficients – V. Aromatic hydrocarbons, Int. J. Thermophys. **13**, 895–905 (1992)
3.132 M.J. Assael, J.H. Dymond, S.K. Polimatidou: Correlation and prediction of dense fluid transport coefficients – VI. *n*-Alcohols, Int. J. Thermophys. **15**, 189–201 (1994)
3.133 M.J. Assael, J.H. Dymond, S.K. Polimatidou: Correlation and prediction of dense fluid transport coefficients – VII. Refrigerants, Int. J. Thermophys. **16**, 761–772 (1995)
3.134 R.B. Bird, W.E. Stewart, E.N. Lightfoot: *Transport Phenomena* (Wiley, New York 1960)
3.135 G.C. Maitland, M. Rigby, E.B. Smith, W.A. Wakeham: *Intermolecular Forces: Their Origin and Determination* (Clarendon, Oxford 1981)
3.136 J.J. Healy, J.J. de Groot, J. Kestin: The theory of the transient hot-wire method for measuring the thermal conductivity, Physica **82C**, 392–408 (1976)
3.137 M.J. Assael, L. Karagiannidis, N. Malamataris, W.A. Wakeham: The transient hot-wire technique: A numerical approach, Int. J. Thermophys. **19**, 379–389 (1998)
3.138 B. Stalhane, S. Pyk: New method of measuring thermal conductivity coefficients, Technisk Tidskrift **61**, 389–397 (1931)
3.139 M.J. Assael, L. Karagiannidis, W.A. Wakeham: Measurements of the thermal conductivity of R11 and R12 in the temperature range 250–340 K at pressures up to 30 MPa, Int. J. Thermophys. **13**, 735–751 (1992)
3.140 M.J. Assael, K. Gialou: A transient hot-wire instrument for the measurement of the thermal conductivity of solids up to 590 K, Int. J. Thermophys. **24**, 667–675 (2003)
3.141 A.M.F. Palavra, W.A. Wakeham, M. Zalaf: Thermal conductivity of *n*-pentane in the temperature range 306–360 K and at pressures up to 0.50 GPa, Int. J. Thermophys. **8**, 305–315 (1987)
3.142 U.V. Mardolcar, J.M.N.A. Fareleira, C.A. Nieto de Castro, W.A. Wakeham: Measurements of the thermal conductivity of argon: a test of the accuracy of the transient hot wire instrument, High Temp.-High Press. **17**, 469–488 (1985)
3.143 Y. Nagasaka, A. Nagashima: Absolute measurements of the thermal conductivity of electrically conducting liquids by the transient hot wire method, J. Phys. E **14**, 1435–1440 (1981)
3.144 R.A. Perkins, A. Laesecke, C.A. Nieto de Castro: Polarized transient hot-wire thermal conductivity measurements, Fluid Phase Equilibr. **80**, 275–285 (1992)
3.145 H. Becker, U. Grigull: Interferometry of transparent phase objects, especially with a high interference fringe density, illustrated by an example from heat transfer, Wärme Stoffübertrag. **10**, 233–244 (1977)
3.146 W.A. Wakeham, J.P.M. Trusler, R.J. de Bruijn, R.J.J. van Diest, T.D. Karapantsios, A.C. Michels: Heat transport near the critical region of a pure fluid in microgravity. In: *Proceedings 2-nd European Symposium Fluids in Space, Naples*, ed. by A. Viviant (Giannini & Figli Publisher, Naples 1996) pp. 29–36
3.147 Sh.H. Jawad: *Thermal conductivity of polyatomic gases. Ph.D. Thesis* (London University, London 1998)
3.148 B. Le Neindre: *Contribution a l'etude experimentale de la conductivite thermique de quelques fluides a haute temperature et a haute pression. Ph.D. Thesis* (Paris University, Paris 1969)
3.149 R. Tufeu: *Etude experimentale en fonction de la temperature et de la pression de la conductivite thermique de l' ensemble des gaz rares et des melanges helium-argon. Ph.D. Thesis* (Paris University, Paris 1971)
3.150 B. Le Neindre, Y. Garrabos, R. Tufeu: Thermal conductivity in supercritical fluids, Ber. Bunsenges. Phys. Chem. **88**, 916–920 (1984)
3.151 A. Michels, J.V. Sengers, P.S. van der Gulik: The thermal conductivity of carbon dioxide in the critical region – II. Measurements and conclusions, Physica **28**, 1216–1237 (1962)
3.152 N.B. Vargaftik, Y.V. Smirnova: On the temperature dependancy of water vapour heat conductivity, Zh. Tekh. Fiz. **26**, 1221–1231 (1956), in Russian
3.153 R.G. Vines: Measurement of thermal conduction of gases at high temperature, J. Heat Transfer **82C**, 48–52 (1960)
3.154 H. Ziebland, J.T.A. Burton: The thermal conductivity of nitrogen and argon in the liquid and gaseous states, Brit. J. Appl. Phys. **9**, 52–59 (1958)

3.155 J. Yata, T. Minamiyama, K. Kajimoto: Thermal conductivity of water and steam at high temperatures and pressures. I. Experimental apparatus and results with water up to 200 °C, B. JSME **22**, 1220–1226 (1979)

3.156 B.J. Bailey, K. Kellner: The thermal conductivity of argon near the critical point, Brit. J. Appl. Phys. **18**, 1645–1647 (1967)

3.157 H.M. Roder, D.E. Diller: Thermal conductivity of gaseous and liquid hydrogen, J. Chem. Phys. **52**, 5928–5970 (1970)

3.158 J.B. Ubbink, W.J. de Haas: Thermal conductivity of gaseous He, Physica **10**, 465–470 (1943)

3.159 G. Grenier: Thermal conductivity of liquid helium, Phys. Rev. **83**, 598–603 (1951)

3.160 R.L. Nuttall, D.C. Ginnings: Thermal conductivity of nitrogen from 50 degrees to 500 degrees and 1 to 100 atmospheres, J. Res. Nat. Bur. Standards **58**, 271–2788 (1957), Research Paper No. 2760

3.161 K.I. Amirkhanov, A.P. Adamov: Heat transfer of steam in near critical and subscritical state; experimental data on heat transfer of steam in range of pressures between 200–400 kg/sq cm and at temperatures of 350 – 450 °C obtained by use of method of plane horizontal layer, Teplogenergetika **10**, 69–72 (1963)

3.162 A. Michels, J.V. Sengers, L.J.M. van de Klundert: The thermal conductivity of argon at elevated gas densities, Physica **29**, 149–160 (1963)

3.163 L.L. Fabelinskii: *Molecular Scattering of Light* (Plenum, New York 1968)

3.164 K. Kraft, M. Matos Lopes, A. Leipertz: Thermal diffusivity and thermal conductivity of toluene by photon correlation spectroscopy: A test of the accuracy of the method, Int. J. Thermophys. **16**, 423–432 (1995)

3.165 P.N. Pusey: *Photon Correlation Spectroscopy and Velocimetry* (Plenum, New York 1976)

3.166 B. Saleh: *Photoelectron Statistics with Applications to Spectroscopy and Optical Communication* (Springer, Berlin, Heidelberg 1978)

3.167 W. Wakeham, A. Nagashima, J.V. Sengers (Eds.): *Experimental Thermodynamics, Measurement of the Transport Properties of Fluids*, Vol. III (Blackwell, Oxford 1991)

3.168 H.J. Eichler, G. Salje, H. Stahl: Thermal diffusion measurements using spatially periodic temperature distributions induced by laser light, J. Appl. Phys. **44**, 5383–5388 (1973)

3.169 D.W. Pohl, S.E. Schwartz, V. Irniger: Forced Rayleigh scattering, Phys. Rev. Lett. **31**, 32–35 (1973)

3.170 T. Hatakeyama, Y. Nagasaka, A. Nagashima: *Measurement of the thermal diffusivity of liquids by the forced Rayleigh scattering method*, Proc. ASME-JSME Thermal Engineering Joint Conference, Honolulu, Vol. 1 (USA 1987) pp. 311–318

3.171 Y. Nagasaka, A. Nagashima: Measurement of the thermal diffusivity of molten KCl up to 1000 °C by the forced Rayleigh scattering method, Int. J. Thermophys. **9**, 923–932 (1988)

3.172 Y. Nagasaka, T. Hatakeyama, M. Okuda, A. Nagashima: Measurement of the thermal diffusivity of liquids by the forced Rayleigh scattering method. Theory and experiment, Rev. Sci. Instrum. **59**, 1156–1168 (1988)

3.173 Y. Nagasaka, N. Nakazawa, A. Nagashima: Experimental determination of the thermal diffusivity of molten alkali halides by the forced Rayleigh scattering method – I. Molten, LiCl, NaCl, KCl, RbCl, and CsCl, Int. J. Thermophys. **13**, 555–573 (1992)

3.174 C.A. Nieto de Castro, S.F.Y. Li, A. Nagashima, R.D. Trengove, W.A. Wakeham: Standard reference data for the thermal conductivity of liquids, J. Phys. Chem. Ref. Data **15**, 1073–1086 (1986)

3.175 J. Kestin, R. Paul, A.A. Clifford, W.A. Wakeham: Absolute determination of the thermal conductivity of the noble gases at room temperature up to 35 MPa, Physica **100A**, 349–369 (1980)

3.176 M.J. Assael, J.H. Dymond, M. Papadaki, P.M. Patterson: Correlation and prediction of dense fluid transport coefficients – I. *n*-Alkanes, Int. J. Thermophys. **13**, 269–281 (1992)

3.177 M.J. Assael, J.H. Dymond, P.M. Patterson: Correlation and prediction of dense fluid transport coefficients – V. Aromatic hydrocarbons, Int. J. Thermophys. **13**, 895–905 (1992)

3.178 M.J. Assael, J.H. Dymond, S.K. Polimatidou: Correlation and prediction of dense fluid transport coefficients – VI. *n*-Alcohols, Int. J. Thermophys. **15**, 189–201 (1994)

3.179 M.J. Assael, J.H. Dymond, S.K. Polimatidou: Correlation and prediction of dense fluid transport coefficients – VII. Refrigerants, Int. J. Thermophys. **16**, 761–772 (1995)

3.180 R.H. Stokes: An improved diaphragm-cell for diffusion studies, and some tests of the method, J. Am. Chem. Soc. **72**, 763–767 (1950)

3.181 J. Kestin, W.A. Wakeham: *CINDAS Data Series on Material Properties. Transport Properties of Fluids, Thermal Conductivity, Viscosity and Diffusion Coefficient*, Vol. I (Hemisphere, New York 1988)

3.182 R. Mills, L.A. Woolf: *The Diaphragm Cell* (Australian National Univ., Canberra 1968)

3.183 L.A. Woolf, J.F. Tilley: Revised values of integral diffusion coefficients of potassium chloride solutions for the calibration of diaphragm cells, J. Phys. Chem. **71**, 1962–1963 (1961)

3.184 G.I. Taylor: Dispersion of soluble matter in solvent flowing slowly through a tube, Proc. R. Soc. London Ser. A **219**, 186–203 (1953)

3.185 G.I. Taylor: Diffusion and mass transport in tubes, Proc. R. Soc. London Ser. B **67**, 857–869 (1954)

3.186 R. Aris: On the dispersion of a solute in a fluid flowing through a tube, Proc. R. Soc. London Ser. A **235**, 67–77 (1956)

3.187 A. Alizadeh, C.A. Nieto de Castro, W.A. Wakeham: The theory of the Taylor dispersion technique for liquid diffusivity measurements, Int. J. Thermophys. **1**, 243–284 (1980)

3.188 W.A. Wakeham: Diffusion coefficient measurements by the chromatographic method, Discuss. Faraday Soc. **15**, 141–150 (1980)

3.189 J.C. Giddings, S.L. Seager: Rapid determination of gaseous diffusion coefficients by means of gas chromatography apparatus, J. Chem. Phys. **33**, 1579–1582 (1960)

3.190 A.C. Ouano: Difusion in liquid systems – I. Simple and fast method of measuring diffusion constant, Ind. Eng. Chem. Fundam. **11**, 268–277 (1972)

3.191 K.C. Pratt, D.H. Slater, W.A. Wakeham: Rapid method for determination of diffusion coefficients of gases in liquids, Chem. Eng. Sci. **28**, 1901–1903 (1973)

3.192 K.C. Pratt, W.A. Wakeham: Mutual diffusion coefficient of ethanol–water mixtures. Determination by a rapid new method, Proc. R. Soc. London Ser. A **336**, 393–406 (1974)

3.193 H.S. Carslaw, J.C. Jaeger: *Conduction of Heat in Solids* (Oxford Univ. Press, New York 1947)

3.194 H.J.V. Tyrrell, K.R. Harris: *Diffusion in Liquids* (Butterworths, London 1984)

3.195 L.O. Sundelöf: Determination of distributions of molecular size parameters by a convolution procedure. A computational and experimental study with special reference to diffusion at low concentrations, Arkiv Kemi **25**, 1–65 (1966)

3.196 L.G. Longsworth: Diffusion measurements at 1° of aqueous solutions of amino acids peptides and sugars, J. Am. Chem. Soc. **74**, 4155–4159 (1952)

3.197 H. Svensson: On the use of Rayleigh–Phulpot–Cook interference fringes for the measurement of diffusion coefficients, Acta Chem. Scand. **5**, 72–84 (1951)

3.198 S. Claesson, H. Matsuda, L.O. Sundelöf: New boundary formation technique for free-diffusion in liquids, Chem. Scripta **6**, 94–96 (1974)

3.199 F.R. McLarnon, R.H. Muller, C.W. Tobias: Reflection effects in interferometry, Appl. Opt. **14**, 2468–2472 (1975)

3.200 G. Gouy: Sur de nouvelles franges d'interfirence, Comptes Rend. **90**, 307–309 (1880)

3.201 G. Kegeles, L.J. Gosting: The theory of an interference method for the study of diffusion, J. Am. Chem. Soc. **69**, 2516–2523 (1947)

3.202 C.A. Coulson, J.T. Cox, A.G. Ogston, J.S.L. Philpot: A rapid method for determing diffusion constants in solutions, Proc. R. Soc. London Ser. A **192**, 382–402 (1948)

3.203 L.J. Gosting, L. Onsager: A general theory for the Gouy diffusion method, J. Am. Chem. Soc. **74**, 6066–6074 (1952)

3.204 I.R. Shankland, P.J. Dunlop: Pressure dependence of the mutual diffusion coefficients of the binary systems N_2+Ar, N_2+O_2, O_2+Ar, and Ar+Kr at 300 and 323 K, Physica **100A**, 64–84 (1980), in German

3.205 T. Graham: On the molecular mobility of gases, Phil. Trans. R. Soc. **153**, 385–405 (1863)

3.206 T.R. Marrero, E.A. Mason: Gaseous diffusion coefficients, J. Phys. Chem. Ref. Data **1**, 3–110 (1972)

3.207 P.J. Dunlop, K.R. Harris, D.J. Young: Experimental methods for studying diffusion in gases, liquids, and solids. In: *Physical Methods of Chemistry*, Vol. VI, ed. by B.W. Rossiter, R.C. Baetzold (Wiley–Interscience, New York 1992)

3.208 J. Loschmidt: Experimental-Untersuchungen über die Diffusion von Gasen ohne poröse Scheidewunde, Sitzber. Mathem.-Natur. Clas. Kaiserl. Akad. Wiss. Wien **62**, 468–478 (1870)

3.209 J. Crank: *The Mathematics of Diffusion* (Clarendon, Oxford 1956)

3.210 W. Wakeham, A. Nagashima, J.V. Sengers (Eds.): *Experimental Thermodynamics, Measurement of the Transport Properties of Fluids*, Vol. III (Blackwell, Oxford 1991)

3.211 M.A. Yabsley, P.J. Dunlop: Study of 2-bulb method for measuring diffusion coefficients of binary gas mixtures, Physica **85A**, 160–164 (1976)

3.212 R.J.J. van Heijningen, A. Feberwee, A. van Costen, J.J.M. Beenakker: Determination of the diffusion coefficient of the system N_2–H_2 as a function of temperature and concentration, Physica **32**, 1649–1662 (1966)

3.213 W.L. Taylor, D. Cain: Temperature dependence of the mutual diffusion coefficients of He–Ar, Ne–Ar and Xe–Ar from 350 to 1300 K, J. Chem. Phys. **78**, 6220–6227 (1983)

3.214 W.A. Wakeham, D.H. Slater: Binary diffusion coefficients of homologous species in argon, J. Phys. B **7**, 297–306 (1974)

3.215 G.M. Schneider: Phase equilibria in fluid systems, Ber. Bunsenges. Phys. Chem. **88**, 841–848 (1984)

3.216 A. Wilsch, R. Feist, G.M. Schneider: Capacity ratios and diffusion coefficients of low-volatility organic compounds in supercritical carbon dioxide from supercritical chromatography, Fluid Phase Equilibr. **10**, 299–306 (1983)

3.217 G.C. Maitland, E.B. Smith: Critical reassessment of viscosity of eleven common gases, J. Chem. Eng. Data **17**, 150–167 (1972)

3.218 P.S. Arora, I.R. Shankland, T.N. Bell, M.A. Yabsley, P.J. Dunlop: Use of precise binary diffusion coefficients to calibrate 2-bulb cell instead of using standard end-correction for connecting tube, Rev. Sci. Instrum. **48**, 673–674 (1977)

3.219 J. Kestin, K. Knierim, E.A. Mason, B. Najafi, S.T. Ro, W.A. Wakeham: Equilibrium and transport properties of the noble gases and their mixtures at low density, J. Phys. Chem. Ref. Data **13**, 229–303 (1984)

3.220 S. Umezawa, A. Nagashima: Measurement of the diffusion coefficients of acetone, benzene and alkane in supercritical CO_2 by the Taylor dispersion method, J. Supercrit. Fluids **5**, 242–250 (1992)

3.221 M.A. Awan, J.H. Dymond: Transport properties of nonelectrolyte liquid mixtures – X. Limiting mutual diffusion coefficients of fluorinated benzenes in *n*-hexane, Int. J. Thermophys. **17**, 759–769 (1996)

3.222 P. Frick, S. Khripchenko, S. Denisov, D. Sokoloff, J.F. Pinto: Effective magnetic permeability of a turbulent fluid with macroferroparticles, Eur. Phys. J. B **25**, 299–402 (2002)

3.223 J. de Vicente, G. Bossis, S. Lacis, M. Guyot: Permeability measurements in cobalt ferrite and carbon iron powders and suspensions, J. Magn. Magn. Mater. **251**, 100–108 (2002)

3.224 I. Hrianca, I. Malaescu: The rf magnetic permeability of statically magnetized ferrofluids, J. Magn. Magn. Mater. **150**, 131–136 (1995)

3.225 J.S. Brooks, G.O. Zimmerman, R. Meservey: Apparatus for the measurement of the magnetic susceptibility of liquids in high magnetic fields, Rev. Sci. Instrum. **54**(9), 1234–1237 (1983)

3.226 M.B. Stout: *Basic Electrical Measurements*, 2nd edn. (Prentice-Hall, Englewood Cliffs 1960)

3.227 D.R. Lide (Ed.): Diamagnetic susceptibility of selected organic compounds, Handbook of Chemistry and Physics. In: *Handbook of Chemistry and Physics*, 84th edn. (CRC, Boca Raton 2004)

3.228 University of Surrey, Department of Electronics and Physical Sciences (2002) http://www.ee.surrey.ac.uk/workshop/advice/coils/mu/#mur

3.229 M. Matsuura, S. Takeuchi: Thermoelectric power and magnetic susceptibility of liquid silver alloys, Trans. TIM **17**, 707–716 (1976)

3.230 S. Takeda, S. Tamaki: Magnetic susceptibilities of liquid Cd-Na and In-Na alloys, J. Phys. Soc. Jpn. **58**(4), 1484–1485 (1989)

3.231 D.R. Lide (Ed.): Magnetic susceptibility of elements and inorganic compounds. In: *Handbook of Chemistry and Physics*, 84th edn. (CRC, Boca Raton 2004)

3.232 P. Terzieff, X. Tsuchiya: Magnetic susceptibility of liquid Ag-Ge, Ag-Sn and Ag-Pb, J. Phys. **13**, 3573–3582 (2001)

3.233 D.P. Fernandez, Y. Mulev, A.R.H. Goodwin, J.M.H.L. Sengers: A database for the static dielectric constant of water and steam, J. Phys. Chem. Ref. Data **24**, 33–69 (1995)

3.234 U. Kaatze: Complex permittivity of water as a function of frequency and temperature, J. Chem. Eng. Data **34**, 371–374 (1989)

3.235 P. Turq, J. Barthel, M. Chemla: *Transport, Relaxation and Kinetic Processes in Electrolyte Solutions* (Springer, Berlin, Heidelberg 1992)

3.236 J.O'M. Bockris, A.K.N. Reddy: *Modern Electrochemistry*, Vol. 1 (Plenum, New York 1970)

3.237 C. Wohlfahrt: *Static dielectric constants of pure liquids and binary liquid mixtures*, Landolt-Börnstein New Ser., Vol. IV/6 (Springer, Berlin, Heidelberg 1991)

3.238 K.N. Marsh (Ed.): *Recommended Reference Materials for the Realization of Physicochemical Properties* (Blackwell, Oxford 1987)

3.239 C. Wohlfart: Permittivity (dielectric constant) of liquids. In: *Handbook of Chemistry and Physics*, 84th edn., ed. by D.R. Lide (CRC, Boca Raton 2004)

3.240 D.A. Saville: Electrohydrodynamics, The Taylor Melcher leaky dielectric model, Annu. Rev. Fluid Mech. **29**, 27–64 (1997)

3.241 R.P. Feynman, R.B. Leighton, M. Sands: *The Feynman Lectures on Physics*, Vol. 2 (Addison Wesley, Palo Alto 1964)

3.242 D. Braun, A.J. Heeger: Visible light emission from semiconducting polymer diodes, Appl. Phys. Lett. **52**(18), 1982–1984 (1991)

3.243 G. Gustafsson, Y. Cao, G.M. Treacy, F. Klavetter, N. Colaneri, A.J. Heeger: Flexible light-emitting-diodes made from soluble conducting polymers, Nature **357**, 477–479 (1992)

3.244 M.N. Simon, B.Y. Lin, H.S. Lee, T.A. Skotheim, J.S. Wall: *Conducting polymer films as EM substrates*, Proc. XIIth Int. Congress for Electron Microscopy, Vol. 1 (San Francisco Press, San Francisco 1990) pp. 290–291

3.245 A.C. MacDiarmid, W.E. Jones, I.D. Norris, J. Gao, A.T. Johnson, N.J. Pinto, J. Hone, B. Han, F.K. Ko, H. Okuzaki, M. Llaguno: Electrostatically-generated nanofibers of electronic polymers, Synth. Met. **119**, 27–30 (2001)

3.246 R.A. Robinson, R.H. Stokes: *Electrolyte Solutions*, 2nd edn. (Butterworths, London 1959)

3.247 A. Newman: Ion transport in roots: measurement of fluxes using ion-selective microelectrodes to characterize transporter function, Plant Cell Environment **24**, 1–14 (2001)

3.248 I. Adamczewski: *Ionization, Conductivity and Breakdown in Dielectric Liquids* (Taylor Francis, London 1969)

3.249 T.J. Gallagher: *Simple Dielectric Liquids, Mobility, Conduction, and Breakdown* (Clarendon, Oxford 1975)

3.250 L. Meyer, F. Reif: Mobility of He ions in liquid helium, Phys. Rev. **110**, 279–280 (1958)

3.251 H. Schynders, L. Meyer, S.A. Rice: Electron mobilities in liquid argon, Phys. Rev. Lett. **15**, 187–180 (1965)

3.252 H. Schynders, L. Meyer, S.A. Rice: Electron drift velocities in liquefied argon and krypton at low electric field strengths, Phys. Rev. **150**, 127–145 (1966)

3.253 J.A. Dean: *Lange's Handbook of Chemistry*, 15th edn. (McGraw-Hill, New York 1999)

3.254 P. Vanysek: Ionic conductivity and diffusion at infinite dilution. In: *Handbook of Chemistry and Physics*, 83rd edn., ed. by D.R. Lide (CRC, Boca Raton 2002)

3.255 R.A. Horne: *Water and Aqueous Solutions, Structure, Thermodynamics and Transport Processes* (Wiley-Interscience, New York 1972)

3.256 R. Heinrich, S. Bonisch, D. Pommerenke, R. Jobava, W. Kalkner: Broadband measurement of the conductivity and the permittivity of semiconducting

materials in high voltage XLPE cables, 8. Int. Conference on Dielectric Materials, Measurements and Applications, Edinburgh, IEE Conf. Publ. **473**, 212–217 (2000)

3.257 D.A. Robinson, C.M.K. Gardner, J. Evans, J.D. Cooper, M.G. Hodnett, J.P. Bell: The dielectric calibration of capacitance probes for soil hydrology using an oscillation frequency response model, Hydrol. Earth Syst. Sci. **2**(1), 111–120 (1998)

3.258 J.B. Hasted: *Aqueous Dielectrics* (Chapman Hall, London 1973)

3.259 R.H. Cole, P. Winsor IV: Fourier transform dielectric spectroscopy. In: *Fourier, Hadamard and Hilbert Transforms in Chemistry*, ed. by A.G. Marshall (Plenum, New York 1982) pp. 183–206

3.260 J.B. Hasted, D.M. Ritson, C.H. Collie: Dielectric properties of aqueous ionic solutions. Part I and II, J. Chem. Phys. **16**(1), 1–11 (1948)

3.261 R.J. Hodgkinson, N.J. Eastman, J. Favaron, H. Owen: Contact and contactless electrical conductivity measurements on the liquid semiconductor systems In-Te and Sb-Tc, J. Phys. C **15**, 4147–4153 (1982)

3.262 P.C. Fannin, S.W. Charles, D. Vincent, A.T. Giannitsis: Measurement of the high-frequency complex permittivity and conductivity of magnetic fluids, J. Magn. Magn. Mater. **252**, 80–82 (2002)